Mitigation of RF Sheaths Through Design and Implementation of Magnetic Field-Aligned ICRF Antenna

by

Michael Lane Garrett

Submitted to the Department of Nuclear Science and Engineering
in partial fulfillment of the requirements for the degree of
Master of Science in Nuclear Science and Engineering
at the
MASSACHUSETTS INSTITUTE OF TECHNOLOGY
June 2012

Author .....
Department of Nuclear Science and Engineering
May 11, 2012

Certified by .....
Stephen J. Wukitch
Research Scientist
Thesis Supervisor

Certified by .....
Dennis G. Whyte
Professor
Thesis Reader

Certified by .....
Ronald R. Parker
Professor
Thesis Reader

Accepted by .....
Mujid S. Kazimi
TEPCO Professor of Nuclear Engineering
Chair, Department Committee on Graduate Students

Mitigation of RF Sheaths Through Design and Implementation of Magnetic Field-Aligned ICRF Antenna

by

Michael Lane Garrett

Submitted to the Department of Nuclear Science and Engineering
on May 11, 2012, in partial fulfillment of the
requirements for the degree of
Master of Science in Nuclear Science and Engineering

Abstract

In ITER and in eventual reactors, enhanced impurity confinement due to internal transport barriers (ITBs) and H-mode operation establishes a very low tolerance for high-Z impurities [1]. Experiments have shown that impurity accumulation increases as power in the ion cyclotron range of frequencies (ICRF) is increased [2]. As a result, one of the primary challenges of ICRF heating is the reduction or elimination of impurities introduced into the plasma during ICRF operation, particularly for tokamaks with high-Z plasma facing components (PFCs). Plasma impurities associated with ICRF auxiliary heating are universally observed [3, 4, 5, 6]. However, the underlying physics of ICRF-specific impurity generation is not well understood, and observations of impurity characteristics differ among various tokamak experiments. Several methods have been proposed to reduce ICRF-specific impurity characteristics: low-Z PFC coatings such as boronization [7]; toroidal phasing of antenna straps [3]; and alignment of antenna Faraday screen elements with the total magnetic field [8]. On Alcator C-Mod we have designed a new magnetic field-aligned ICRF antenna to minimize ICRF-specific impurity characteristics. The field-aligned antenna is rotated 10° from horizontal, such that the antenna straps are perpendicular to the total magnetic field at the edge for a typical plasma discharge ($B_{\mathrm{T}} \sim 5.4$ T, $I_{\mathrm{p}} \sim 1$ MA). ICRF-induced E-parallel is a likely candidate for producing enhanced sheath voltages that lead to greatly increased sputtering of material surfaces and enhanced impurity edge transport. Initial simulations performed using both slab and cylindrical geometry suggested nearly complete cancellation of E-parallel in front of the antenna structure for certain toroidal phasings. Using toroidal models, the cancellation of E-parallel is more modest, suggesting 3-D geometrical effects are important. Multiple antenna phases were analyzed for the field-aligned antenna using finite element method with a 3-D toroidal cold plasma model. In each case, the field-aligned antenna had reduced integrated E-parallel relative to the existing non-aligned antenna geometry, with the greatest reduction for monopole [0, 0, 0, 0] phasing. Initial results suggest that the field-aligned antenna operation results in fewer impurities in the plasma than conventional antennas.

Thesis Supervisor: Stephen J. Wukitch
Title: Research Scientist

Thesis Reader: Dennis G. Whyte
Title: Professor

Thesis Reader: Ronald R. Parker
Title: Professor

Acknowledgments

Many people have contributed both directly and indirectly to this body of work. First, I would like to thank Steve Wukitch whose guidance, instruction, and insight has enabled me to complete the work presented in this thesis. Steve has helped me to grow as a scientist and engineer, and allowed me to develop the analytical, numerical and experimental skills necessary to excel in my work. I would like to thank Dennis Whyte for many things, including his extraordinary teaching ability, his vision, and his endless support throughout this process. Jeff Freidberg, for believing in me, for assigning the hardest problem sets and exams I've ever seen, and for inviting me to TA for his fusion energy class. Ron Parker, for his encouragement and for sharing his vast knowledge of fusion systems and RF heating and current drive mechanisms. Anne White, for both her support and advice. Miklos Porkolab, for teaching me plasma wave physics. I also would like to thank Earl Marmar for his leadership and support, without which I certainly would not be able to write this thesis.

I would like to thank Pete Koert, for countless insightful conversations. Pete has forgotten more about RF than I am likely to ever know. Yijun Lin, for his ICRF physics knowledge and help. Paul Bonoli, for his help with numerical techniques, his wave physics expertise, and his encouragement. Orso Meneghini and Syunichi Shiraiwa, for introducing me to FEM and for countless conversations about plasma numerical work. Jim Terry, for insightful discussions of plasma edge turbulence. Alan Binus and Rick Murray, for their help, knowledge, support and patience. Andy Pfeiffer, for his help with anything and everything, and his innovative problem solving ability. Rui Vieira, whose insight, engineering acumen and positive attitude is nothing short of amazing. Bill Beck, for his engineering expertise and general support. I would also like to thank the entire C-Mod team and PSFC staff, including Ed Fitzgerald, Bill Forbes, Mark Iverson, Jack Nickerson, Sue Agabian and Tom Tolan, who were always ready and willing to help regardless of the task at hand.

I would like to thank my officemates: Geoff Olynyk, Bob Mumgaard, and Dan Brunner. I certainly could not have made it through my first years at MIT without

their patience, help and friendship. Zach Hartwig, for his support, friendship and occasional cyclocross or Wompatuck ride invitation. Jessica Coco, for the countless hours spent keeping the C-Mod ship afloat. I would like to thank Liz Parmelee, Clare Egan and Heather Barry for all of their help and support and for conveying just how much they truly care about students.

I would like to thank Tim Graves, my friend and colleague, who first suggested I consider research on Alcator C-Mod at MIT. I would like to thank Ed Beiting for being an excellent mentor, for introducing me to plasma physics and propulsion systems, and for his generous support and guidance.

I would like to thank my family: My dad, Bill and my Mom, Pam who always believed in me, taught me that anything was possible, and let me find my own way. My sister Meg, whose creativity, humor, encouragement, and friendship has helped me for each of the all-but-three years of my life that I've known her.

Finally, I would like to thank my wonderful partner, Natalie Canfield, whose love, friendship, understanding, patience, humor and charisma has been invaluable during my often difficult tenure in graduate school.

Contents

List of Figures

List of Tables

Chapter 1

Introduction

1.1 Energy

Energy is literally all around us, contained in each photon reaching the earth from the sun, every air molecule moving at some individual and bulk velocity, and in the mass of every particle of matter anywhere. The greatest problem the current generation of humans must overcome is not how to find energy, nor is it to make energy, because we cannot.

> There is a fact, or if you wish, a *law*, governing all natural phenomena that are known to date. There is no known exception to this law—it is exact so far as we know. The law is called the *conservation of energy*. It states that there is a certain quantity, which we call energy, that does not change in the manifold changes which nature undergoes. That is a most abstract idea, because it is a mathematical principle; it says that there is a numerical quantity which does not change when something happens. It is not a description of a mechanism, or anything concrete; it is just a strange fact that we can calculate some number and when we finish watching nature go through her tricks and calculate the number again, it is the same. —Richard Feynman

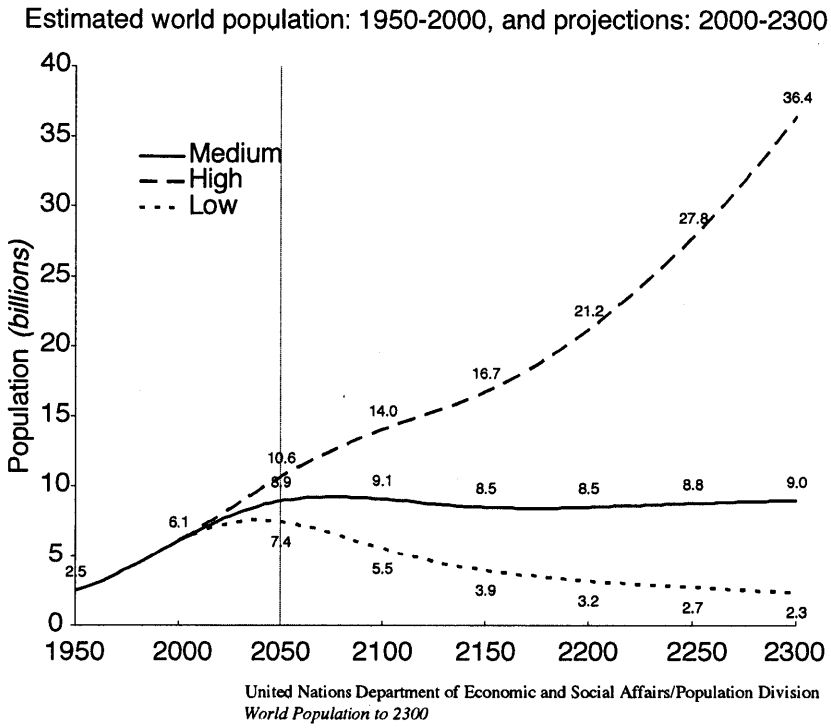

Figure 1-1: Projections of world population through 2300 by United Nations. Source: United Nations, Department of Economic and Social Affairs Population Division, *World Population to 2300*, 2004.

The greatest problem facing the present population of the earth is how best to translate energy from the sources all around us to facilitate a higher standard of living for all. The United Nations predicts a peak population of 9.2 billion in 2060 [11], as seen in Fig. 1-1. As the earth's population continues to grow, global energy demands will increase. At the present rate of population, industrial and economic growth, major energy shortages, as well as irreparable changes to the environment, will occur within the next several decades.

Today, many different energy sources are converted into a usable form. However, all of them have limitations in terms of fuel availability, energy density and environmental side-effects. Generally, energy sources can be placed into three primary categories: fossil fuels, consisting of oil, coal and natural gas; renewables such as solar, wind and hydroelectric; and nuclear, such as currently used fission reactors and

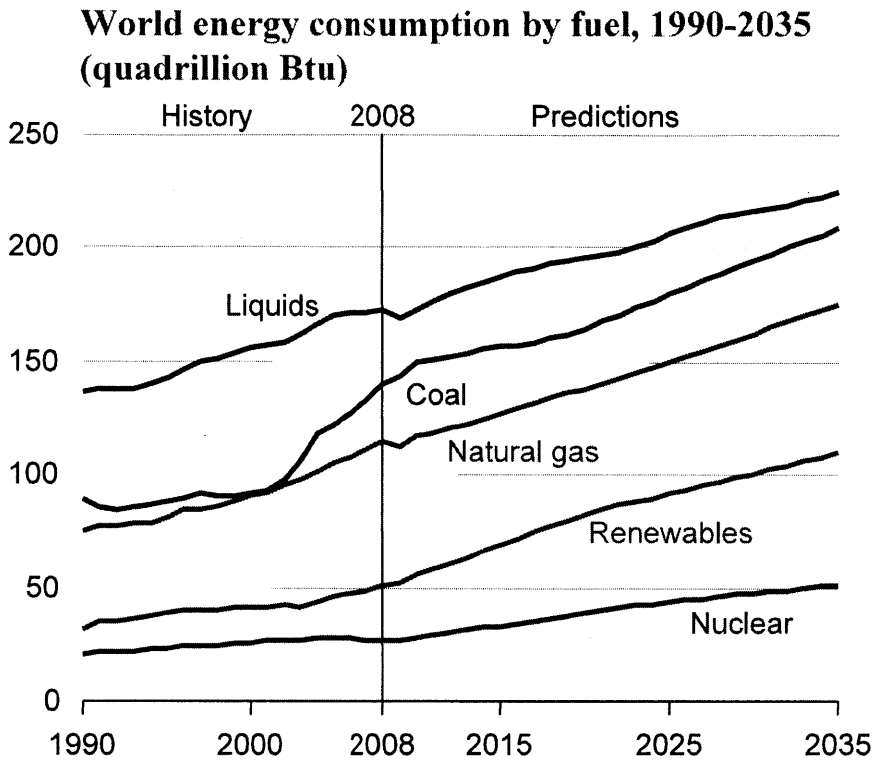

Figure 1-2: World energy consumption by fuel, 1990-2035. Source: U.S. Energy Information Administration, *International Energy Outlook*, 2011

future fusion reactors.

Fossil fuels have high energy density, cost relatively little, and can provide *base load* electricity. However, they must be chemically burned, producing carbon dioxide (CO_2) and other greenhouse gases. Oil is used primarily for transportation due to its high energy density and portability. Oil can also be used for heating but is not as efficient as natural gas for this purpose. Natural gas is primarily composed of methane (CH_4), and can be efficiently burned with fewer emissions than coal. However, the burning of natural gas does produce significant CO_2 emissions. Coal provides over half the electricity in the US and there are substantial reserves of coal all over the world. Unfortunately, the burning of coal also produces significant amounts of CO_2, contributing to greenhouse gases. It also produces toxic emissions of calcium carbonate, nitrous oxide and sulfur dioxide as well as traces of radioactive material. Many

people are surprised to learn that a typical coal power plant releases more radiation than a typical nuclear fission power plant [12].

Renewable energy sources have the advantage of producing zero emissions and, of course, being renewable. However, renewables are typically very low energy density sources. Hydroelectric generators located inside dams are an exception, and have high energy density; similar to the energy density of coal power plants. These power plants produce zero emissions and are also capable of supplying base load power. Unfortunately, most of the potential hydroelectric dam sites are already used. In addition, for any major future hydroelectric power plant sites, the environmental impact on the area that must be flooded upriver from the dam will be significant. Solar energy also generates zero emissions, and is, neglecting capital costs, an essentially free energy source. However, solar cannot provide base load power. Nor can it provide much power at all per unit area covered with solar transducers. This is because the photon sets the energy density scale for solar power. Each incident photon has an energy of order 1 electon-volt (eV) which is 1.6×10^{-19} joules. Wind energy shares the advantages of solar: it has zero emissions, and neglecting capital costs, is free. However, wind energy also suffers from low energy density and the inability to provide base load power.

Nuclear energy has several important advantages relative to both fossil fuels and renewables. Nuclear energy produces no greenhouse gases or other emissions. Nuclear reactors are also well suited to provide base load power. The energy density of a nuclear reaction is six orders of magnitude larger than that of the chemical reactions which burn fossil fuel. Compared with an incident photon in a solar array, the fission of a uranium nucleus (U^{235}) produces approximately 200 million electron volts (MeV) and the fusion of a deuteron (D) and a Triton (T) releases 17.6 MeV.

The safety of fission reactors is a constant source of public scrutiny and concern. However, even taking into account the disaster at Chernobyl (1986), and more recently, Fukushima (2011), public sentiment regarding nuclear energy risk far exceeds the actual danger. In fact, nuclear energy in use today produces far less damage to both human health and the environment per watt of power produced than coal.

Uranium, the fuel used in fission reactors is relatively abundant with hundreds to thousands of years of reserves. However, scientists still have not found a way to close the nuclear fuel cycle. As a result, many of the fission products will remain highly radioactive for hundreds of thousands of years. This timeline can be drastically reduced, by recycling spent radioactive fuel in so called *breeder reactors.* However, nuclear weapon proliferation remains an indirect consequence of fission reactors.

Similar to fission, fusion energy has the potential to provide high energy density, zero emissions, and base load power. However, fusion has many potential benefits that make it a much more attractive energy source than fission, coal, gas or any of the renewables. The fuel of fusion reactors comes from isotopes of hydrogen: deuterium and tritium. Deuterium is universally abundant in the form of seawater. Tritium can be bred inside a fusion reactor from abundant reserves of lithium. Fusion reactors are also not easily weaponizable; they do not produce products that could be made into a bomb or other weapon. In fact, the only product from the fusion reaction is helium, which is one of the most inert elements. Finally, fusion reactors are inherently safe. The fusion reaction is so difficult to maintain, that if anything were to happen to the structure itself—if a critical element were to overheat, or if a catastrophic leak were to develop in the reaction chamber, the fusion reaction would simply cool off and stop. Damage could occur to the reactor itself, but there is no chance of a *meltdown* or similar energy runaway event associated with fission reactors. Although in many ways a utopian energy source, the one major drawback to fusion energy is that we have yet to construct a fusion reactor with a net energy gain.

Fusion energy continues to be a significant technological challenge to the engineers and scientists throughout the world working on it. However, constant incremental progress has been made since fusion research was declassified by the U.S. Government in 1958. Around the world, tokamak fusion reactors like MIT's Alcator C-Mod are discovering new physics and solving important engineering problems to try to make fusion energy a reality. Today, a seven-member international collaboration is building the world's first burning fusion reactor, ITER, which should provide a path from current reactors to a demonstration fusion power plant. Fusion is not merely an

attractive solution to the the world's energy problems, it is likely the only long-term solution capable of meeting world energy consumption while ensuring protection of the planet's environment.

1.2 Fusion research

1.2.1 Plasma

As the temperature of matter increases it transitions though states of solid, liquid and gas. If it becomes even hotter, the atoms of the material ionize, thereby dissociating the negatively charged electrons from the positively charged nucleus. When this happens to a sufficient number of atoms in a given population, the resulting *ions* begin to exhibit collective behavior as a result of the Lorentz forces they create as they move. This *ionized* collection of particles is a plasma. Because most of the particles in a plasma have a net electric charge, fusion scientists can exploit an attribute of their motion given by the Lorentz force: $\mathbf{F} = q(\mathbf{E} + \mathbf{v} \times \mathbf{B})$. The $\mathbf{v} \times \mathbf{B}$ component of this force causes charged particles to orbit magnetic field lines as they travel along them. This gyroscopic motion causes charged particles to trace helical trajectories along magnetic field lines. If these field lines can be made to *close* on themselves, then the particles can be confined in a general area defined by this magnetic field.

1.2.2 Fusion energy

Nuclear fusion reactions occur when light nuclides fuse to form heavier nuclides. As a direct result of the strong nuclear force, nuclides lighter than iron (see Fig. 1-3), have masses larger than their fusion product. This mass deficit Δm, is the source of fusion energy. Relativity theory describes the amount of energy released from each fusion reaction as Δmc^2, where c is the speed of light. More specifically, this *binding energy* is given by:

$$E_B = \left(N m_{\mathrm{n}} + Z m_{\mathrm{p}} - m_{\mathrm{A}}\right) c^2 \tag{1.1}$$

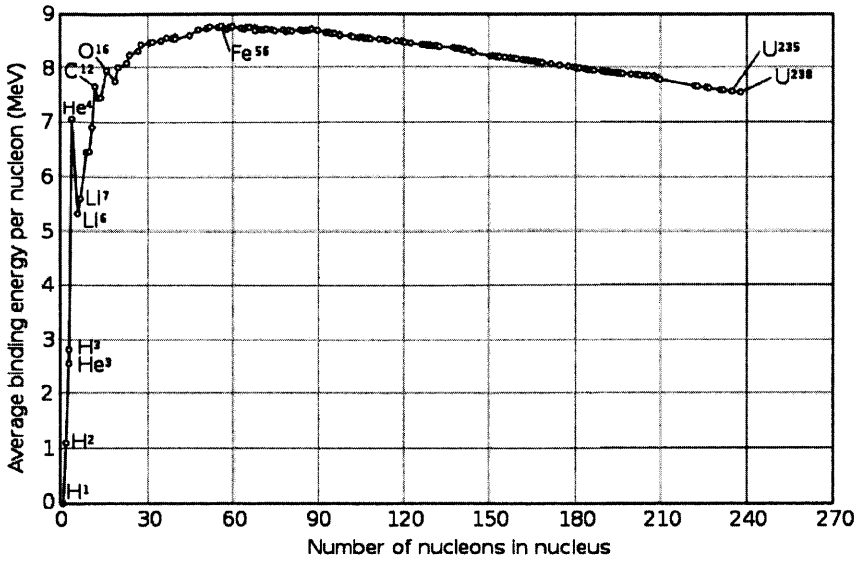

Figure 1-3: Nuclear binding energy.

where Nm_{n} is the total mass of the neutrons, Zm_{p} is the total mass of the protons, and m_{A} is the mass of the resulting nuclear product.

The six nuclear reactions of primary interest for fusion reactors are:

- $D + D \rightarrow T(1.01MeV) + p(3.03MeV)$
- $D + D \rightarrow He^3(0.82MeV) + n(2.45MeV)$
- $D + T \rightarrow He^4(3.52MeV) + n(14.06MeV)$
- $D + He^3 \rightarrow He^4(3.67MeV) + p(14.67MeV)$
- $Li^6 + n \rightarrow T + He^4 + (4.8MeV)$
- $Li^7 + n \rightarrow T + He^4 + n - (2.5MeV)$

where D is deuterium, T is tritium, He^3 is helium, and Li is lithium. Most experiments today, including Alcator C-Mod, use deuterium plasmas. Deuterium-deuterium reactions produce two branches of products of as seen above; either a triton and a proton are produced, or a helium-3 nucleus and a neutron. Note that both of these reactions release a moderate amount of energy ($\sim 4MeV$) compared with the D-T or D-He^3 reactions ($\sim 18MeV$). For the D-T reaction, 17.6 MeV are transferred into the kinetic

energy of the reaction products from the nuclear strong force. As can be seen from Fig. 1-4, the reaction rate $\langle \sigma v \rangle$ for D-T is almost two orders of magnitude larger than both D-D and D-He^3, below 30 keV. As a result, for a given nuclear reaction rate, D-T reactions occur at a lower temperature than do D-D or D-He^3 reactions. This is an important consideration because the required temperatures for thermonuclear fusion are very high $\sim$ 10 keV, or about 120 million degrees Celcius. This is due to an electrostatic barrier, called the Coulomb potential barrier, surrounding each nucleus which arises from the electrostatic charge of the protons contained therein. This mutual electrostatic repulsion of similarly charged nuclei must be overcome in order to bring the two nuclei close enough for the fusion reaction to occur. This can be achieved by heating a plasma of deuterium and tritium to the requisite temperatures, thus using the thermal velocity of the particles to overcome the Coulomb barrier and initiate the fusion reaction. The volumetric reaction rate for these fusion events is given by:

$$R_{ij} = n_i n_j \langle \sigma v \rangle, \tag{1.2}$$

where the velocity averaged cross section $\langle \sigma v \rangle$ is shown in Fig. 1-4, and n_i and n_j represent the particle number densities of two ion species.

Two distinct confinement methods are being studied for fusion reactions: inertial and magnetic. In inertial confinement fusion, high energy (MJ), short pulse (ps) lasers are used to implode a cryogenic capsule containing a mixture of D-T. This laser pulse initiates a burn wave which rapidly ablates the surface of the D-T fuel and, via Newton's 3rd law, provides a reaction force which rapidly compresses the target capsule to pressures and temperatures required for fusion. The details of inertial confinement fusion are beyond the scope of this thesis. As its name suggests, magnetic confinement utilizes magnetic fields to confine the plasma and keep it away from the walls of the device, which are much colder than the plasma itself. This confinement allows the plasma to be heated sufficiently to achieve the temperatures and pressures required for fusion.

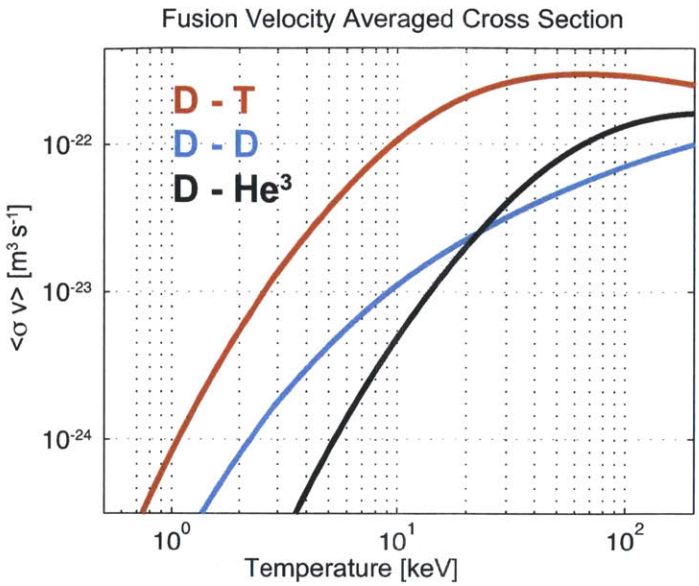

Figure 1-4: Velocity averaged cross section $\langle \sigma v \rangle$ for D-T, D-D, and D-He^3 reactions as a function of temperature.

1.2.3 Tokamaks and stellarators

The choice of magnetic topology used to confine a plasma is not an obvious one. As mentioned in Sec. 1.2.2, charged particles are forced to move along magnetic field lines. Initial fusion experiments utilized cylindrical plasmas with axial magnetic fields. To prevent the particles from streaming out the ends of the device, separate magnets were used to create magnetic mirror fields at the ends. However, significant particle and energy losses can still occur along the field lines in the magnetic mirror geometry. As a result, mirror devices have typically had poor performance. The end losses, combined with poor plasma stability, limit the achievable plasma temperature and confinement time.

In the 1950s a group of Russian scientists invented a new type of magnetic confinement device called a tokamak. The work tokamak comes from the Russian acronym, TOKAMAK (**TO**роидалыная **КА**мера с **МА**гнитными **К**атушками), which means toroidal chamber with magnetic coils. Here, the Russians discovered a magnetic topology which can have a set of surfaces where there exists a non-vanishing

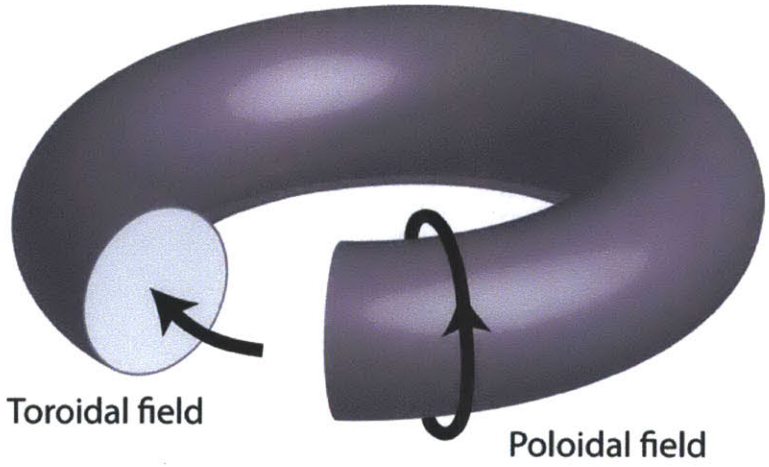

Figure 1-5: Toroidal and poloidal magnetic fields required to realize rotational transform in a tokamak.

continuous tangent vector field. In other words, the magnetic field lines on the surface of a torus can be made to wrap around continuously. In 1968, at the Kurchatov Institute in Moscow, Russian scientists achieved a record plasma temperature of $\sim$ 1 keV, an order of magnitude higher than any of the western devices had reached at the time [13]. Today, all magnetic fusion devices are structured around a general toroidal geometry to prevent end-losses.

The torus is the desired topology; however, if a cylinder with an axial magnetic field, called a θ-pinch, is simply bent into a torus, it turns out to be unstable. As a result, a poloidal magnetic field must be combined with the toroidal field from the θ-pinch, as shown in Fig. 1-5, to form a helical magnetic field configuration known as a screw-pinch (see Fig. 1-6).

The toroidal magnetic field has a 1/R dependence and decreases from the center of the tokamak to the outside. The toroidal field also has a curvature associated with it, because its in the shape of a torus. When a gradient exists within the magnetic field in a plasma, a so-called grad-B (∇B) drift of the electrons and ions occurs:

$$v_{\nabla B} = -\frac{m v_{\perp}^2}{2e} \frac{\nabla B \times \mathbf{B}}{B^3}, \tag{1.3}$$

which causes the ions and electrons to drift in opposite directions resulting in charge

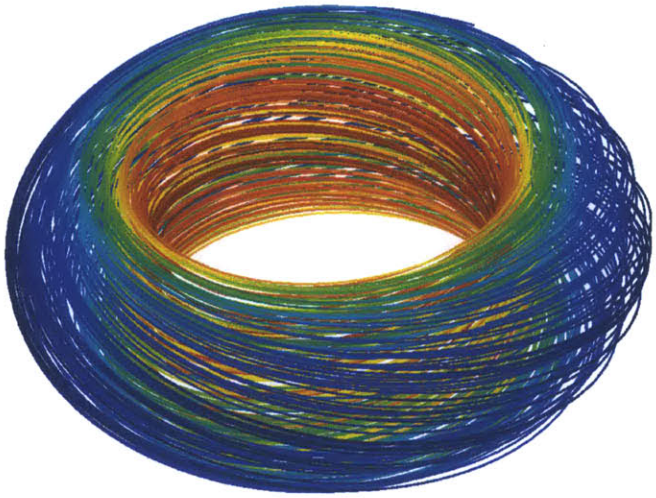

Figure 1-6: Reconstruction of the total magnetic field in Alcator C-Mod for shot 1050426022, t = .64 s. Color indicates field magnitude: Max (red) 7.8 T, Min (blue) 3.2 T.

separation. When a magnetic field is present in the plasma with some finite curvature, another drift, the curvature drift occurs:

$$v_K = \frac{m v_\parallel^2}{e R_c} \frac{\mathbf{R}_c \times \mathbf{B}}{B^2}, \tag{1.4}$$

which also results in charge separation. These two properties, the magnetic field gradient and the magnetic field curvature, cause particles in a tokamak to drift vertically in opposite directions for different charge polarity. If the field is purely toroidal, this charge separation produces a vertical electric field, resulting in an additional drift ($\mathbf{E} \times \mathbf{B}$) of the plasma radially towards the low-field side.:

$$v_{\mathbf{E}\times\mathbf{B}} = \frac{\mathbf{E} \times \mathbf{B}}{B^2}. \tag{1.5}$$

To ameliorate this effect, a poloidal magnetic field is required.

The velocity distribution of a particle in a non-uniform magnetic field changes changes as it moves. As the particle moves toward a higher field, its parallel velocity decreases, while its perpendicular velocity increases. In a tokamak, this *mirror* effect

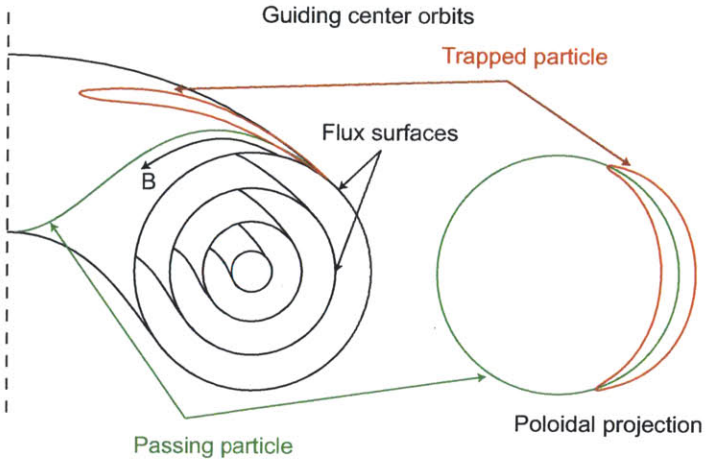

Figure 1-7: Circular cross-section tokamak flux surfaces. Passing particles transit from low-field side to high-field side, circulating around the torus. The trapped particles, lacking sufficient initial $v_{\parallel}$, are reflected and trace out banana-shaped orbits.

causes particles with low initial parallel velocities to reflect and become trapped in low-field orbits which are shaped like bananas. If a particle has a sufficiently large parallel velocity, it avoids becoming trapped in a so-called *banana orbit* and passes through the high-field side of the tokamak, orbiting around the entire torus. These orbits are shown in Fig. 1-7.

All axisymmetric toroidal fusion devices have both poloidal and toroidal magnetic fields. On a tokamak, large toroidal field coils, which wrap around the torus in the poloidal direction, provide the toroidal magnetic field. The poloidal field must be generated by current running through the plasma itself. The Spitzer plasma resistivity for a deuterium plasma is given by:

$$\eta \approx 5.2 \times 10^{-5} \frac{Z_{\text{eff}} \ln \Lambda}{T_e^{3/2}} \quad [\Omega\text{m}], \tag{1.6}$$

where T_e is the electron temperature in eV, Z_{eff} is the effective atomic number, and Λ is given by:

$$\Lambda = \frac{4}{3}\pi \left(\frac{\varepsilon_0 T_e}{e^2 n_0} \right)^{3/2} n_0. \tag{1.7}$$

Thus, the resistivity of the plasma is extremely small at fusion temperatures $\eta \sim$

$1 \times 10^{-9}\Omega$m. As a result, this current can be driven inductively by a large solenoid positioned in the center of the torus. Here, the plasma functions as the secondary winding of a transformer; the central solenoid functions as the primary winding. However, the central solenoid current ramp is limited to a finite amount of time. Therefore, a fusion power plant, which must operate in steady-state, needs to drive current in the plasma through some non-inductive method. Several non-inductive current drive methods have produced promising experimental results. For a reactor, the most efficient method is likely to be coupling an asymmetric toroidal spectrum of radio frequency (RF) waves to the plasma. On Alcator C-Mod, this is accomplished using lower hybrid (LH) waves which lose their energy to high energy electrons in the plasma, thorough a process called Landau damping. However, many physics and engineering challenges must be solved for lower hybrid current drive (LHCD) before it can be successfully implemented on a reactor.

As mentioned above, a poloidal magnetic field is critical to confining a plasma in a toroidal fusion device. However, there is an alternative to driving a current in the plasma itself to accomplish rotational transform of the field lines. Instead, the toroidal magnetic field coils can be deformed to provide both a toroidal and poloidal magnetic field. This alternative approach is used in a class of fusion devices called stellarators. In stellarators, the current drive problem is solved. However, the resulting plasma and magnetic configuration is no longer truly axisymmetric and is extraordinarily complex.

In both the tokamak and the stellarator, plasma equilibrium and stability require complicated coil configurations and real-time control of plasma shaping. Magnetohydrodynamics (MHD), a single fluid model combining electromagnetism and fluid dynamics, is used to characterize the fundamental plasma equilibrium and stability. Magnetohydrodynamics theory has been instrumental in quantifying operational regimes useful for a fusion reactor.

The tokamak, in particular, has produced promising results in machines all over the world. Today, a next-step fusion reactor is being constructed in Cadarache, France. The International Thermonuclear Experimental Reactor (ITER) is scheduled

to have first plasma in 2020. ITER is designed to achieve a net energy gain with a physics gain factor $Q = 10$. The physics gain factor is given by:

$$Q = \frac{\frac{1}{4} n_e^2 \langle \sigma v \rangle E_\mathrm{f} \cdot V_\mathrm{p}}{P_\mathrm{h}}, \tag{1.8}$$

where the rate coefficient $\langle \sigma v \rangle$ is shown in Fig. 1-4, E_f is the fusion energy per reaction, V_p is the plasma volume, and P_h is the external heating power. Here, $Q = 1$ is the break-even operation point, $Q > 5$ is defined as a burning plasma, and $Q = \infty$ is ignition. From this definition, ITER is expected to produce a burning plasma, in which heating from the α-particles inside the plasma is double the external heating power applied to the reactor. ITER should extend our understanding of fusion plasmas into the burning plasma regime and contribute to the next large step toward actualizing commercially available fusion power, a demonstration fusion power plant (DEMO).

To review, tokamak fusion reactors (including current machines and future devices like ITER) utilize a large toroidal magnetic field, a smaller poloidal magnetic field produced by the toroidal current in the plasma. In addition, vertical field coils are used to control the radial position of the plasma, and various error field coils and shaping coils are necessary to optimize the plasma shape inside the vacuum vessel. A central solenoid is used to generate and control the plasma current. This describes a simple methodology for confining the plasma in a particular region. However, in order for the individual particles to overcome the Coulomb barrier described in Sec. 1.2.2, the plasma must be heated to extreme temperatures.

1.3 Heating

1.3.1 Ohmic heating

The volumetric fusion reaction rate is a function of temperature, as seen in Fig. 1-4. As a result, all magnetic fusion experiments require external heating to bring the plasma to a burning plasma scenario, when α-heating takes over. In order to

increase the temperature of the plasma close to ignition, where zero external heating is supplied, auxiliary heat must be initially provided. In reality, a reactor will always operate sub-ignition because a small amount of auxiliary power is required for plasma control.

In a tokamak, the central solenoid can fulfill another role, related to that described above. Fusion plasmas are good conductors with some finite resistivity given by Eq. 1.6. As the central solenoid current is changed, a current is induced in the plasma. This current effectively heats the plasma through ohmic heating due to the resistivity of the plasma. However, as the plasma heats up its resistivity decreases as electron-ion collisions become less frequent. The electron-ion collision frequency is given by:

$$\nu_{\mathrm{ei}} = \left(\frac{e^4 n_{\mathrm{i}} \ln \Lambda}{4\pi\epsilon_0^2 m_{\mathrm{e}} m_{\mathrm{i}}}\right) \frac{1}{v_{\mathrm{e}}^3 + 1.3 v_{\mathrm{iTh}}^3} \tag{1.9}$$

Here, we see that the electron-ion collision frequency scales as v^{-3}, or $T^{-3/2}$. Therefore, although ohmic heating can be effective at low temperatures, its effectiveness rapidly decreases with increasing temperature. To quantify this effect for a simple case, we can calculate the maximum temperature that could be achieved through ohmic heating alone. If we assume a flat current profile and a circular cross section toroidal plasma, the ohmic heating power is:

$$P_{\mathrm{OH}} = 2\eta I^2 \frac{R}{a^2} \tag{1.10}$$

where η is given in Eq. 1.6, R is the torus major radius, a is the torus minor radius, I is the total current, and T_e the electron temperature in keV. Using ITER as an example with a plasma current, $I_p = 15$ MA, at a temperature of 1 keV: $P_{OH} \approx 100$ MW, at 5 keV: $P_{OH} \approx 10$ MW, and at 10 keV: $P_{OH} \approx 3$ MW. To estimate the the maximum temperature which can be achieved, we can set the ohmic power dissipation equal to the loss power. The energy confinement time scaling can be used to estimate the loss power:

$$P_{\mathrm{L}} = \frac{3nTV}{\tau_{\mathrm{E}}}. \tag{1.11}$$

Using ITER plasma parameters, setting Eq. 1.10 equal to Eq. 1.11 and solving for temperature, we find that the maximum temperature that could be reached in ITER for an ohmically heated plasma is $\sim$ 2.5 keV. Although this is a very simple calculation, it illustrates the significance of the $T^{-3/2}$ resistivity scaling. A fusion reactor simply cannot rely on ohmic heating methods alone. In order to reach a burning plasma condition, or ignition, some form of auxiliary heating is necessary. The primary methods of auxiliary heating involve either neutral particle beams, or radio frequency waves. Neutral particle beams can be used to heat the plasma by injecting energetic ions into the plasma which then transfer energy to the bulk plasma as they slow down via collisions. Radio frequency waves can heat the plasma through resonances associated with either electron or ion species in the plasma. Electron cyclotron heating (ECH) uses high frequency, short wavelength waves to interact with electrons near the electron cyclotron frequency:

$$\Omega_{\mathrm{e}} = \frac{eB}{m_{\mathrm{e}}}, \tag{1.12}$$

which, for ITER at a magnetic field of 5.4 T, is approximately 150 GHz. These waves have short wavelengths, $\lambda \sim 2$ mm, and propagate as they would in a vacuum, allowing excellent spatial resolution and hence, the ability to deposit the ECH power where it is needed. One drawback of ECH is the limited availability of high power, steady-state microwave sources. In contrast, ion cyclotron heating (ICH) has widely available high power, steady-state, relatively inexpensive radio frequency sources. ICH uses longer wavelength waves than ECH in the ion cyclotron range of frequencies (ICRF) to interact with ions near the ion cyclotron frequency:

$$\Omega_{\mathrm{i}} = \frac{ZeB}{m_{\mathrm{i}}}. \tag{1.13}$$

For ITER at a magnetic field of 5.4 T, this frequency is approximately 40 MHz for deuterium, with a wavelength, $\lambda \sim 7$ m. ICRF heating is one of the most efficient of the auxiliary heating methods. ICRF provides the majority of the auxiliary heating power on Alcator C-Mod, and it will also provide a significant fraction of auxiliary

heating on ITER.

1.3.2 ICRF heating

Heating in the ion cyclotron range of frequencies is accomplished by damping of energy from launched electromagnetic waves onto particles in the plasma. One advantage of ICRF heating is that the ions are heated directly when the wave frequency is near the ion cyclotron frequency, or one of its harmonics. Details of ICRF heating physics will be presented in Ch. 2. Here, a cursory overview of ICRF is given to describe the motivation for this thesis.

ICRF heating is accomplished by launching the fast magnetosonic wave, or fast wave (FW), typically from the low field side of the tokamak. The antennas designed for this purpose are typically poloidal inductive current loops which couple an RF magnetic flux to the DC magnetic flux inside the plasma. The work presented in this thesis arises from a specific problem within ICRF heating operation: RF sheath formation and its relationship to ICRF-specific impurity characteristics. Impurities associated with ICRF auxiliary heating are universally observed [3, 4, 5, 6]. However, the underlying physics of ICRF-specific impurity generation is not well understood. Full wave simulation codes are used to predict wave absorption in the plasma core. For certain phenomena, there is reasonable agreement between simulation and experimental results. However, there are many aspects of ICRF-plasma interaction that require more accurate simulation tools and methods. A particular area of importance is that the ICRF antenna structure must reside near the boundary region of the plasma in order to assure that the waves can propagate into the plasma for heating. Wave physics in the edge, including scrape off layer (SOL) physics, ICRF induced $\mathbf{E} \times \mathbf{B}$ convection, turbulence and RF sheath physics require a more robust agreement between theory and experiment.

This thesis is narrow in focus, as it must be. However, my hope is that by quantifying a specific part of ICRF-plasma interactions, it will contribute to shortening the timeline to a fusion energy power plant. In this thesis, previous and existing Alcator C-Mod antennas are studied in slab, cylindrical, and toroidal geometry. In addition,

a new magnetic field-aligned antenna is optimized for magnetic flux coupling, and mitigation of integrated $E_{\|}$. Both isotropic dielectric and cold plasma models are used to load each antenna. The parallel electric field is quantified for different antennas, toroidal phasing of current loops, magnetic field pitch angle and antenna box topology.

The method, simulation, results and conclusions of this thesis are discussed in the following chapters. Ion cyclotron range of frequency (ICRF) physics is discussed in Ch. 2. Chapter 3 pertains to ICRF-relevant impurity characteristics. Finite element method simulations coupling RF with cold plasma are discussed in Ch. 4. Simulation results and antenna development are given in Ch. 5. Chapter 6 illustrates the manufacturing and installation of the field-aligned antenna. Experimental results are presented in Ch. 7. Finally, conclusions and future simulation and experimental work are discussed in Ch. 8.

Chapter 2

ICRF Physics

2.1 Radio frequency heating physics

Radio frequency heating of tokamak plasmas is accomplished by electromagnetic (EM) waves launched into the plasma. These EM waves propagate inward into the plasma and deposit energy through resonant collisionless processes. The accessibility of the waves to the plasma core is of fundamental importance. In a tokamak, there are several resonances and cut-offs for multi-species plasmas which depend on the magnetic field, and the mass and charge of each species j as seen in the cyclotron frequency definition:

$$\Omega_j = \frac{q_j B}{m_j}. \tag{2.1}$$

Each resonance is associated with both absorption and reflection. Resonances are defined as surfaces in the plasma where the perpendicular index of refraction:

$$n_\perp = \frac{ck_\perp}{\omega}, \tag{2.2}$$

where c is the speed of light, $k_\perp$ is the wavenumber perpendicular to the magnetic field and ω is the wave frequency, goes to infinity: $n_\perp^2 \to \infty$. Conversely, cut-offs are defined as surfaces in the plasma where the perpendicular index of refraction goes to zero: $n_\perp^2 \to 0$. The actual physics in the vicinity of a resonance or cut-off is quite

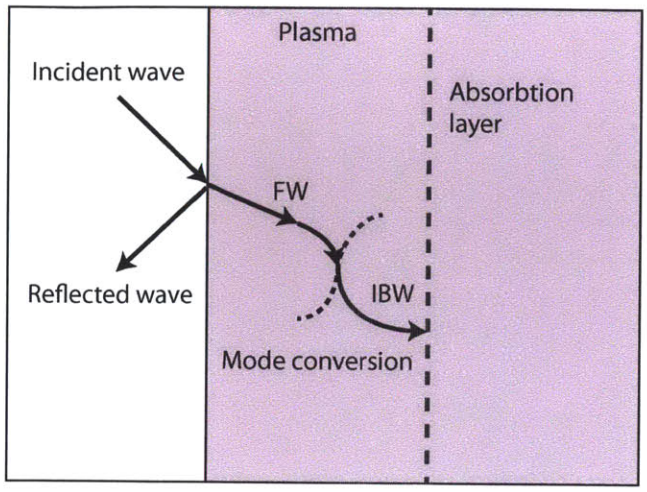

Figure 2-1: Schematic of simple mode conversion model.

complicated. Generally, at a cut-off surface the incident wave produces not only a reflected wave, but also a transmitted wave, as some of the energy tunnels through the evanescent region near the cut-off to an area where propagation can occur. A simple description of this process is given by the Budden model [14]:

$$\frac{\mathrm{d}^2\phi}{\mathrm{d}\xi^2} + \frac{k_0^2\left(\xi - \xi_c\right)}{\xi}\phi = 0, \tag{2.3}$$

where k_0 is the wave number, ξ is the spatial coordinate, ξ_c is the location of cut-off, and ϕ is the wave amplitude. Here, a simple estimate of the fraction of transmitted power is given by [14]:

$$T = exp\left(-\pi k_0 \xi_c\right). \tag{2.4}$$

The actual transmission is significantly more complicated and requires a kinetic treatment of the waves to allow for secondary degenerate modes. These degenerate modes allow a process called mode conversion to occur, whereby the incident wave couples some of its energy to a second type of wave (see Fig. 2-1). The mode conversion process will be described in more detail later, but for ICRF it allows the launched fast magnetosonic wave to couple energy into a category of electrostatic waves, called ion Bernstein waves (IBW). The physics of hot plasma wave dispersion is extremely

complicated. However, simplified models can provide significant insight about wave propagation and absorption in tokamak plasmas. The cold plasma model is used extensively to characterize simplified wave-plasma interaction in tokamaks. In this model, the magnetic field and plasma density are assumed to be static and first-order quantities can be Fourier analyzed in time and space as:

$$Q = \widetilde{Q} \exp(\mathrm{i}\mathbf{k} \cdot \mathbf{r} - \mathrm{i}\omega t). \tag{2.5}$$

Maxwell's equations provide a starting point to obtain the cold plasma model:

$$\nabla \cdot \mathbf{E} = \frac{\rho}{\varepsilon_0}, \tag{2.6}$$

$$\nabla \cdot \mathbf{B} = 0, \tag{2.7}$$

$$\nabla \times \mathbf{E} = -\frac{\partial \mathbf{B}}{\partial t}, \tag{2.8}$$

$$\nabla \times \mathbf{B} = \mu_0 \mathbf{J} + \mu_0 \varepsilon_0 \frac{\partial \mathbf{E}}{\partial t}. \tag{2.9}$$

Ampere's law (Eq. 2.9) and Faraday's law (Eq. 2.8) can be Fourier analyzed per Eq. 2.5, linearized such that $\nabla \rightarrow \mathrm{i}\mathbf{k}$, and $\partial/\partial t \rightarrow -\mathrm{i}\omega$, and combined to obtain the wave equation:

$$\mathbf{k} \times (\mathbf{k} \times \mathbf{E}) = -\mathrm{i}\omega\mu_0 \mathbf{J} - \frac{\omega^2}{c^2}\mathbf{E}, \tag{2.10}$$

where $\mathbf{k} = \omega/c\ \mathbf{n}$, and $c^2 = (\mu_0 \varepsilon_0)^{-1}$. A conductivity tensor can be introduced to define the relationship between current density and the electric field: $\mathbf{J} = \overleftrightarrow{\boldsymbol{\sigma}} \cdot \mathbf{E}$. Inserting $\overleftrightarrow{\boldsymbol{\sigma}}$ into Eq. 2.10 and rearranging, we obtain:

$$\mathbf{n} \times (\mathbf{n} \times \mathbf{E}) + \left[\overleftrightarrow{\boldsymbol{I}} + \frac{\mathrm{i}}{\varepsilon_0 \omega} \overleftrightarrow{\boldsymbol{\sigma}}\right] \mathbf{E}. \tag{2.11}$$

Here, the quantity in brackets is the permittivity tensor:

$$\overleftrightarrow{\boldsymbol{\epsilon}} = \left[\overleftrightarrow{\boldsymbol{I}} + \overleftrightarrow{\boldsymbol{X}}\right] = \left[\overleftrightarrow{\boldsymbol{I}} + \frac{\mathrm{i}}{\varepsilon_0 \omega} \overleftrightarrow{\boldsymbol{\sigma}}\right]. \tag{2.12}$$

To evaluate this expression for the plasma permittivity, we must obtain $\overleftrightarrow{\boldsymbol{\sigma}}$. This can

be accomplished using Ohm's law and the equations of motion. This results in two bounding equations for the current density:

$$\mathbf{J} = \overleftrightarrow{\boldsymbol{\sigma}} \cdot \mathbf{E} = nq\mathbf{v}, \tag{2.13}$$

which, written in component form becomes:

$$\mathbf{J} = \begin{bmatrix} \sigma_{xx} & \sigma_{xy} & \sigma_{xz} \\ \sigma_{yx} & \sigma_{yy} & \sigma_{yz} \\ \sigma_{zx} & \sigma_{zy} & \sigma_{zz} \end{bmatrix} \begin{bmatrix} E_x \\ E_y \\ E_z \end{bmatrix} = nq \begin{bmatrix} v_x \\ v_y \\ v_z \end{bmatrix}. \tag{2.14}$$

Calculation of the perturbed velocity components begins with the two-fluid momentum equations for ions and electrons, where we define $\hat{z} \parallel \hat{B}_0$ [12]:

$$m_j \left(\frac{\partial \mathbf{v}_j}{\partial t} + \mathbf{v}_j \cdot \nabla \mathbf{v}_j \right) = \pm q \left(\mathbf{E} + \mathbf{v}_j \times \mathbf{B} \right). \tag{2.15}$$

This equation can be linearized and solved in component form for the three perturbed velocity components as a function of the electric field. After some algebra we find:

$$v_{xj} = \frac{\mathrm{i} q_j \omega E_x}{m_j \left(\omega^2 - \Omega_j^2 \right)} - \frac{q_j \Omega_j E_y}{m \left(\omega^2 - \Omega_j^2 \right)}, \tag{2.16}$$

$$v_{yj} = \frac{q_j \Omega_j E_x}{m_j \left(\omega^2 + \Omega_j^2 \right)} - \frac{\mathrm{i} q_j \omega E_y}{m_j \left(\omega^2 - \Omega_j^2 \right)}, \tag{2.17}$$

$$v_{zj} = \frac{\mathrm{i} q_j E_z}{\omega m_j}. \tag{2.18}$$

Now we are able to calculate the components of $\overleftrightarrow{\boldsymbol{\sigma}}$ from Eq. 2.14. We find:

$$\sigma_{xx} = \sigma_{yy} = \sum_j \frac{q_j^2 n}{m_j} \frac{\omega}{\left(\omega^2 + \Omega_j^2 \right)}, \tag{2.19}$$

$$\sigma_{xy} = -\sigma_{yx} = i\sum_j \frac{q_j^2 n}{m_j} \frac{\Omega_j}{\left(\omega^2 + \Omega_j^2\right)}, \tag{2.20}$$

$$\sigma_{zz} = \sum_j \frac{q_j^2 n}{m_j \omega}, \tag{2.21}$$

$$\sigma_{zx} = \sigma_{xz} = \sigma_{zy} = \sigma_{yz} = 0. \tag{2.22}$$

Inserting the components of the conductivity tensor into Eq. 2.12, we calculate the susceptibility $\overleftrightarrow{X}$, which, when added with the unit tensor $\overleftrightarrow{I}$ yields the plasma dielectric tensor [15]:

$$\overleftrightarrow{\epsilon} = \begin{bmatrix} S & -iD & 0 \\ iD & S & 0 \\ 0 & 0 & P \end{bmatrix}, \tag{2.23}$$

with the sum (S), difference(D), and plasma(P) components, given by:

$$S = 1 - \sum_j \frac{\omega_{pj}^2}{\omega^2 - \Omega_j^2}, \tag{2.24}$$

$$D = \sum_j \frac{\Omega_j}{\omega} \frac{\omega_{pj}^2}{\omega^2 - \Omega_j^2}, \tag{2.25}$$

$$P = 1 - \sum_j \frac{\omega_{pj}^2}{\omega^2}, \tag{2.26}$$

where we have introduced the plasma frequency for each species:

$$\omega_{pj} = \left(\frac{n_j e^2}{m_j \epsilon_0}\right)^{\frac{1}{2}}. \tag{2.27}$$

Now that we have the dielectric tensor, we can find the dispersion relationship for wave propagation in the plasma. We can rearrange the components of Eq. 2.11 to obtain a single tensor multiplying **E**. First, we rewrite the double cross product in Eq. 2.11 as:

$$\mathbf{n}\times(\mathbf{n}\times\mathbf{E})=\mathbf{n}(\mathbf{n}\cdot\mathbf{E})-\mathbf{E}(\mathbf{n}\cdot\mathbf{n})=\left[\mathbf{n}\cdot\mathbf{n}-\overleftrightarrow{\mathbf{I}}n^2\right]\mathbf{E}, \tag{2.28}$$

which, in component form is:

$$\begin{bmatrix} n_\perp^2 & 0 & n_\perp n_\parallel \\ 0 & 0 & 0 \\ n_\perp n_\parallel & 0 & n_\parallel^2 \end{bmatrix} - \begin{bmatrix} n^2 & 0 & 0 \\ 0 & n^2 & 0 \\ 0 & 0 & n^2 \end{bmatrix} = \begin{bmatrix} -n_\parallel^2 & 0 & n_\perp n_\parallel \\ 0 & -n_\perp^2 - n_\parallel^2 & 0 \\ n_\perp n_\parallel & 0 & -n_\perp^2 \end{bmatrix}. \tag{2.29}$$

Combining with the dielectric tensor, we find:

$$\begin{bmatrix} S-n_\parallel^2 & -\mathrm{i}D & n_\perp n_\parallel \\ \mathrm{i}D & S-n_\perp^2-n_\parallel^2 & 0 \\ n_\perp n_\parallel & 0 & P-n_\perp^2 \end{bmatrix} \begin{bmatrix} E_\mathrm{x} \\ E_\mathrm{y} \\ E_\mathrm{z} \end{bmatrix} = 0. \tag{2.30}$$

In order to obtain a non-trivial solution to Eq. 2.30 the determinant must equal zero. This allows the description of the natural modes of oscillation within the system by the root(s) of a dispersion relation, $\omega = \omega(\mathbf{k})$. Here, the cold plasma dispersion relation is obtained by setting the determinant equal to zero:

$$n_\perp^4 S + n_\perp^2(D^2 - (S-n_\parallel^2)(S+P)) + P((S-n_\parallel^2)^2 - D^2) = 0. \tag{2.31}$$

For a wave propagating at an angle θ to $\mathbf{B}$ [15], we can rewrite this dispersion equation as:

$$An^4 - Bn^2 + C = 0 \tag{2.32}$$

$$A = S\sin^2\theta + P\cos^2\theta \tag{2.33}$$

$$B = RL\sin^2\theta + PS\left(1+\cos^2\theta\right) \tag{2.34}$$

$$C = PRL, \tag{2.35}$$

where $R = S + D$, and $L = S - D$. Solving this quadratic in n^2 we find:

$$n^2 = 1 - \frac{RL\sin\theta^2 + PS\left(1 + cos\theta^2\right) \pm \left[\left(RL - PS\right)^2 \sin\theta^4 + 4P^2D^2\cos\theta^2\right]^{1/2}}{2\left(S\sin\theta^2 + P\sin\theta^2\right)} \tag{2.36}$$

Equation 2.36 can be rearranged to quickly reveal four modes of wave propagation; two modes are parallel to the magnetic field, and two are perpendicular to the magnetic field:

$$\tan\theta^2 = -\frac{P\left(n^2 - R\right)\left(n^2 - L\right)}{\left(Sn^2 - RL\right)\left(n^2 - P\right)}. \tag{2.37}$$

For the trivial solution, $B_0 = 0$ we find the dispersion for a simple EM wave:

$$n^2 = 1 - \sum_j \frac{\omega_{pj}^2}{\omega^2}. \tag{2.38}$$

Four additional dispersion relations can immediately be seen for $\theta = 0$ and $\theta = \pi/2$. For $\mathbf{k} \parallel \mathbf{B}$, by making the bracketed terms in the numerator of Eq. 2.37 go to zero, two waves exist. The R-mode is a right-hand circularly polarized (RHCP) wave given by:

$$n^2 = R, \tag{2.39}$$

and the L-mode is a left-hand circularly polarized (LHCP) wave given by:

$$n^2 = L. \tag{2.40}$$

For $\mathbf{k} \perp \mathbf{B}$, by making the bracketed terms in the denominator of Eq. 2.37 go to zero, there are also two waves of interest. The O-mode has $\mathbf{E} \parallel \mathbf{B}$ and is given by:

$$n^2 = P \tag{2.41}$$

The X-mode has $\mathbf{E} \perp \mathbf{B}$ and is given by:

$$n^2 = \frac{RL}{S} \tag{2.42}$$

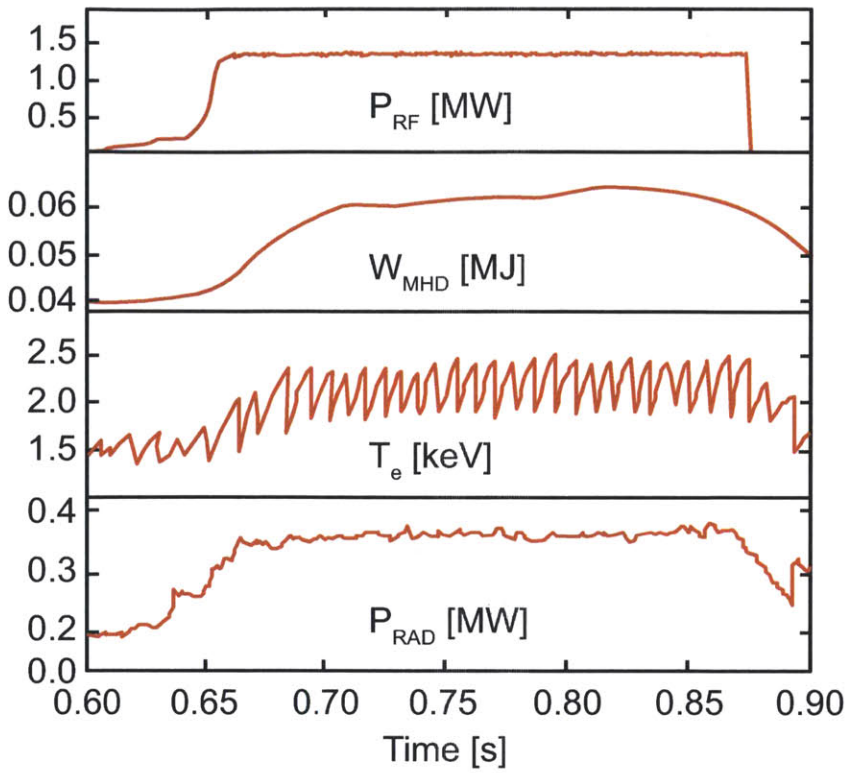

Figure 2-2: Effect of ICRF heating on plasma parameters for a typical low confinement mode discharge on Alcator C-Mod.

Now we will focus on a specific group of plasma waves within the X-mode category above. These are waves associated with the ion cyclotron range of frequencies (ICRF).

2.2 Ion cyclotron heating

Ion cyclotron range of frequencies (ICRF) heating is very effective at transferring energy into the plasma through wave particle resonances. Fig. 2-2 shows the effect of ICRF on several plasma parameters during a typical discharge on Alcator C-Mod. When ICRF is turned on, the plasma stored energy W_{MHD}, central electron temperature T_{e0}, and radiated power P_{RAD}, increase significantly. In a tokamak, the large toroidal magnetic field described in Ch. 1, depends inversely on the major radius. For a circular cross-section device, neglecting poloidal current, this magnetic field can

be written as:

$$B_\phi = \frac{B_0 R_0}{R}, \tag{2.43}$$

where B_0 is the magnetic field strength on axis, and R_0 is the major radius of the torus. For a magnetic field of 5.4 T, the resonant frequencies of a proton and a deuteron are approximately 80 MHz and 40 MHz, respectively. As long as the solutions to the dispersion relation given by Eq. 2.31 are well separated, using reasonable approximations, we can find two solutions relevant for ICRF physics:

$$n_\perp^2 = \frac{\left(n_\parallel^2 - R\right)\left(n_\parallel^2 - L\right)}{\left(S - n_\parallel^2\right)} \qquad \text{Fast wave (FW)} \tag{2.44}$$

$$n_\perp^2 = \frac{P}{S}(S - n_\parallel^2) \qquad \text{Slow wave (SW)} \tag{2.45}$$

The fast magnetosonic wave, or fast wave (FW) is the desired wave for ICRF heating. The slow wave is cut-off at all but very low densities in the tokamak. As a result, the SW propagation can only occur near the edge of the plasma. However, as will be discussed in Ch. 3, the fast wave can parasitically couple to the slow wave and produce undesired plasma interactions near the plasma edge. The slow wave has a large electric field component parallel to the magnetic field ($E_\parallel$). In the edge region of the plasma, the density is low and the plasma is not as effective at shielding the RF electric field. As a result $E_\parallel$ present at the edge can drive radio frequency sheaths (RF sheaths), which produce deleterious plasma material interactions (PMI).

The fast wave is used in radio frequency heating on tokamaks for several reasons. The FW polarization ensures that the electric field component of the wave parallel to the magnetic field is negligible. The large $E_\perp$ component of fast wave allows it to be launched effectively by inductive loops which couple large amounts of RF magnetic flux to the plasma. The damping mechanisms for the fast wave and waves to which the FW converts are quite efficient. The damping effectiveness for these waves is correlated to the amount of reflection the waves encounter as they transit

the plasma. The desired wave propagation involves a *single pass* through the plasma, where the wave deposits all of its energy before reflecting off the plasma edge, or a cut-off surface within the plasma. This effect is called *single pass absorption.*

2.2.1 Ion absorption

The ion cyclotron resonance allows absorption of launched wave energy for certain plasma parameters. Equations 2.1 and 2.43 define resonant surfaces, where the cyclotron frequency or one of its harmonics is equal to the frequency of the launched wave. The absorption of launched waves can be spatially localized to a region near this resonant surface. The specific region of absorption can be controlled by adjusting B, ω, m_j, or q_j. One obstacle to absorption is the polarization of the launched wave, which must have a finite LHCP component to effectively couple to the ions in the plasma. The fraction of power absorbed at the resonance depends on the ratio of the LHCP component of **E** to the RHCP component of **E**:

$$\frac{E^+}{E^-} = \frac{D+S}{D-S} = \frac{\omega - \Omega_i}{\omega + \Omega_i} \tag{2.46}$$

In Eq. 2.46 we see that no absorption occurs at the fundamental resonance surface ($\omega + \Omega_i$). This is because the launched fast wave is purely right-hand circularly polarized at the cyclotron resonance, which is opposite to the left-handed ion gyration. If waves are launched at the second harmonic of the cyclotron frequency, a portion of the wave has the correct polarization to damp its energy. However, this damping is quite sensitive to both density and temperature [12].

Another method, called minority heating, is used to create strong wave-particle resonance and heating in a multi-species plasma. In the minority heating regime, a small population of *minority* particles added to the bulk *majority* plasma. The frequency of the launched wave is chosen to correspond to the fundamental resonance of the minority species. In this case the polarization of the wave maintains sufficient left-handedness to allow effective plasma-wave coupling to occur. Minority concentrations are generally a few percent, as absorption peaks at a small critical minority ion

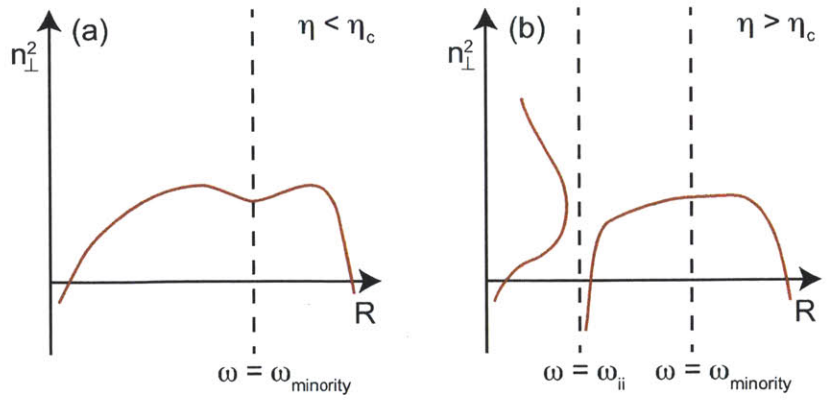

Figure 2-3: Schematic fast wave perpendicular refractive index vs. R. In (a) the minority concentration is below the critical fraction $\eta < \eta_c$; in (b) the minority concentration is above the critical fraction $\eta > \eta_c$ and mode conversion can occur.

fraction η_c. For minority fractions above the critical value a different heating regime appears, as seen in Fig. 2-3. In this regime, the fast wave transfers some of its energy into different propagation modes which can heat the electrons in the plasma directly.

2.2.2 Electron absorption

In a multi-species plasma, the fast wave can be mode converted to the ion cyclotron wave (ICW) and the ion Bernstein wave (IBW) if the minority fraction is above a critical value [16]. Both the IBW and the ICW encounter significant electron landau damping (ELD) inside the plasma. As a result, the power contained in these mode converted waves is transferred directly to the electrons in the plasma. The mechanisms listed above allow effective transfer of energy from the wave to the plasma species across a range of different plasma conditions.

One difficulty of ICRF heating is that the antenna structure must be positioned very close to the plasma. This is because the fast wave is evanescent at low densities near the plasma edge. This proximity to the plasma edge introduces a host of challenges related to plasma-antenna interaction. These plasma-antenna interactions will be discussed in detail in Ch. 3. First, we will outline the Alcator C-Mod ICRF system.

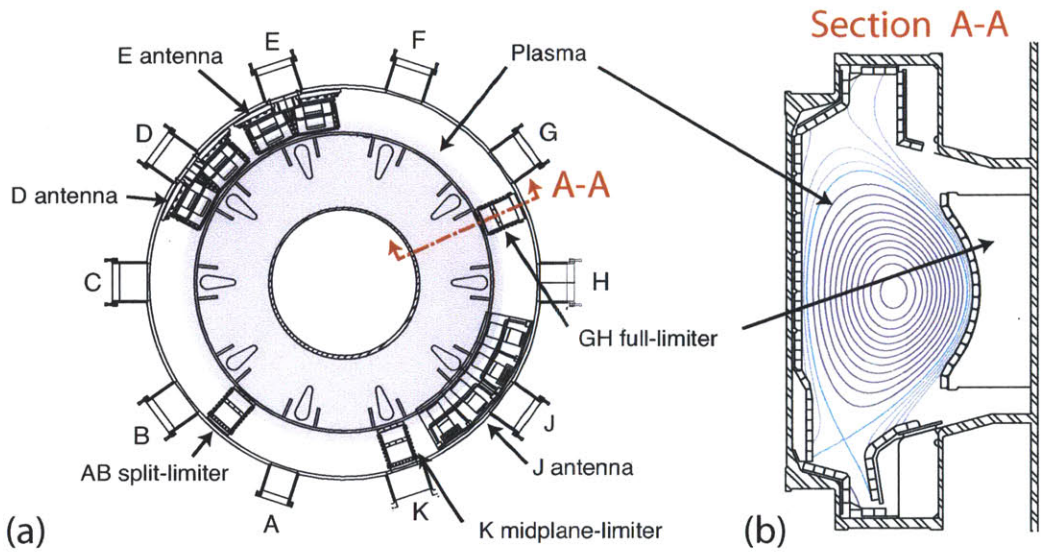

Figure 2-4: Alcator C-Mod shown in top view (a), and poloidal cross section (b).

2.3 ICRF heating on Alcator C-Mod

2.3.1 *ALto CAmpo TORus*

Alcator C-Mod is one of three National Tokamak Facilities in the United States. The characteristics of Alcator C-Mod are described in detail elsewhere [17]. Although it is a relatively small machine, (major radius, $R_0 = 0.67$ m, minor radius, $a = 0.22$ m) Alcator C-Mod is uniquely equipped to study ITER and reactor-relevant ICRF physics. It operates at high densities (up to $10^{21}\mathrm{m}^{-3}$) and has the highest toroidal magnetic field (up to 8 T) of any divertor tokamak. The C-Mod ICRF antennas operate at power densities of up to 10 $\mathrm{MW/m^2}$, ~ 50 % higher than expected ITER ICRF power densities [18]. ITER is also expected to have similar single-pass ICRF wave absorption to that of Alcator C-Mod. In addition, both experiments utilize high-Z plasma facing components (PFC) in the divertor, and contain plasmas where the scrape-off-layer (SOL) is opaque to neutrals [19]. Operational parameters for Alcator C-Mod are listed in table 2.1. A top view and poloidal cross section of the tokamak are shown in Fig. 2-4, and an image of the inside of the machine is shown in Fig. 2-5.

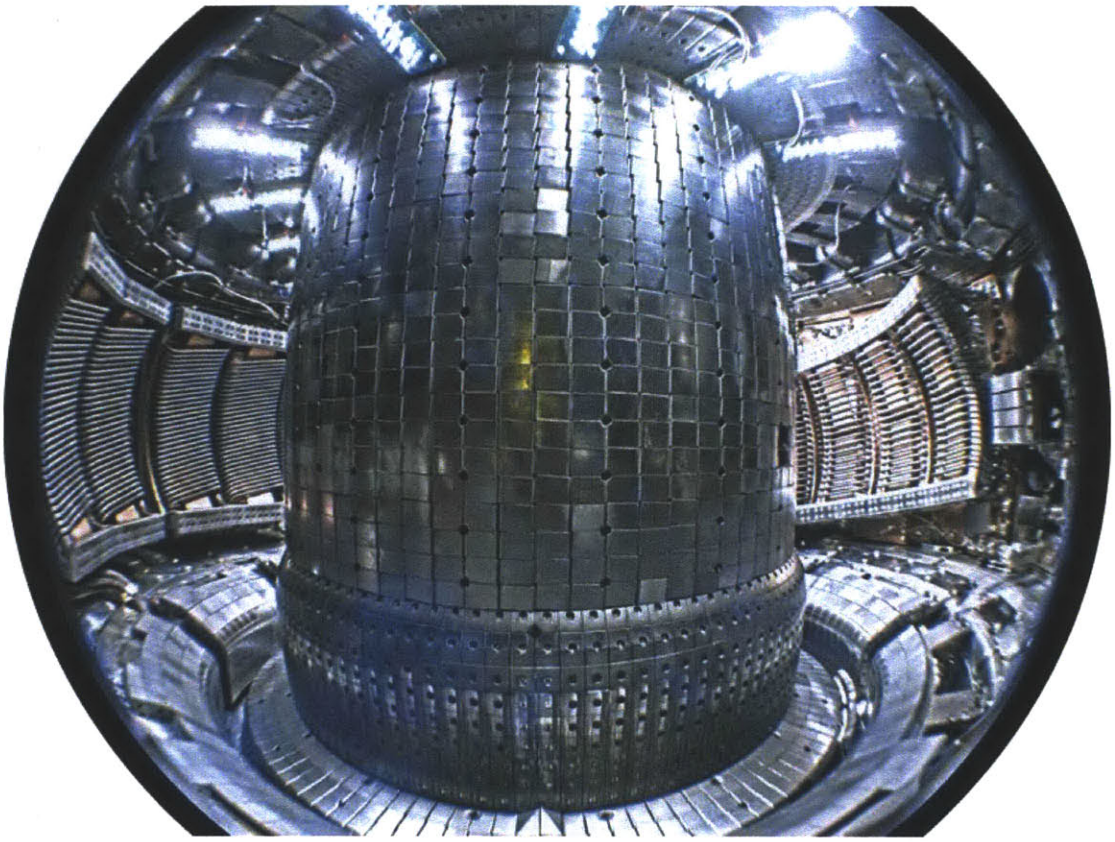

Figure 2-5: High dynamic range composite image of the inside of Alcator C-Mod taken from B-port (see Fig. 2-4). Two conventional ICRF antennas (D-port and E-port) are visible to the left of the central column. The new field-aligned antenna (J-port) is visible to the right of the central column.

Alcator C-Mod is a diverted tokamak, but can be operated with limited discharges using either the inner wall, or poloidal limiters shown in Fig. 2-4. The structure consists of a stainless steel vacuum chamber encased in a cryostat. The inside of the machine is armored with TZM molybdenum refractory tiles, visible in Fig. 2-5. The vacuum vessel is divided into ten sections and has ten horizontal and twenty vertical ports (labeled A-K in Fig. 2-4) to provide access to the plasma for diagnostics and ICRF transmission lines. Several sets of magnetic coils are used to confine and control the plasma. All of the coils are copper conductors cooled to liquid nitrogen temperatures to minimize resistive losses. There are twenty toroidal coils (carrying a total current of 265,000 Amperes during a pulse), which wrap around the central core, producing a peak magnetic field of 22 T at the center of the device. These

Table 2.1: Alcator C-Mod parameters

Major radius	R_0	=	0.67 m
Minor radius	a	=	0.22 m
Toroidal field	B_T	$\leq$	8 T
Plasma current	I_p	$\leq$	2 MA
Elongation	ϵ	$\sim$	1.7
Triangularity	δ	$\sim$	.4
Flat top duration	t	$\sim$	2 s
Inductive volt seconds	Φ	$\sim$	7 Wb
Average density	$\langle n \rangle$	$\leq$	$10^{21}\mathrm{m}^{-3}$
Central electron temperature	T_{e0}	$\leq$	5 keV

magnets produce extremely large self-forces (100 MN). As a result, a series of wedge plates, massive cover plates and superalloy draw bars are used to prevent the device from exploding under the loads produced during a plasma discharge. These loads are so large that the cover plates on the top and bottom of the machine, which are 3 m in diameter, 0.66 m thick, and weigh 31,000 kg each, flex over 3 mm during a pulse. In addition to the toroidal coils there are four sets of poloidal coils and a central solenoid.

A typical discharge lasts 1-2 seconds and uses approximately 500 MJ of energy. This energy is provided by a 10 m long, 200,000 kg alternator that is magnetically braked to translate rotational kinetic energy into electrical energy for the tokamak. At 1800 rpm, the alternator stores approximately 5 billion joules of energy. Approximately 20-30 discharges can be run during a single day, with 20 minutes in between. During this time the magnets have adequate time to cool down and the alternator can spin back up to its pre-discharge speed using power drawn from the Cambridge electrical grid. For each discharge, extensive data are taken for almost every machine parameter and diagnostic system. These data are stored in networked servers to be accessed by graduate students, scientists and engineers.

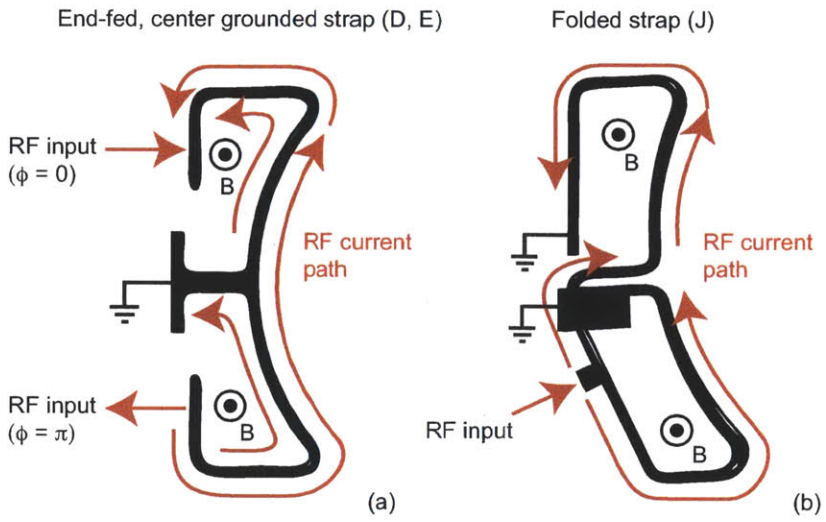

Figure 2-6: Schematic of Alcator C-Mod ICRF antenna strap topology: the end-fed, center-grounded strap used for the D and E-port antennas (a), and the folded strap used for the field-aligned antenna, located at J-port (b).

2.3.2 ICRF

Auxiliary heating on Alcator C-Mod is accomplished almost exclusively with ICRF. Three ICRF antennas are installed on the machine. These antennas are shown at the locations of the D, E and J-ports in Fig. 2-4. The antennas at the D and E-ports each use two end-fed, center-grounded straps with two coaxial inputs per strap and operate with a fixed dipole toroidal phasing [18, 20]. The previous antenna located at J-port used four balanced, folded straps with a single coaxial input per strap [21]. This antenna has been replaced with a new magnetic field-aligned antenna which also uses folded straps with a single coaxial input per strap. The field-aligned antenna is rotated 10° from horizontal, such that the antenna straps are perpendicular to the total magnetic field at the edge for a typical plasma discharge ($B_T \sim 5.4$ T, $I_p \sim 1$ MA). Both strap topologies are illustrated in Fig. 2-6. As indicated in the drawing, each of the antenna straps is composed of two poloidal current loops to couple RF magnetic flux to the plasma. This RF flux coupling is paramount and is shown schematically in Fig. 2-7. Unlike the 2-strap antennas, both of the 4-strap antennas

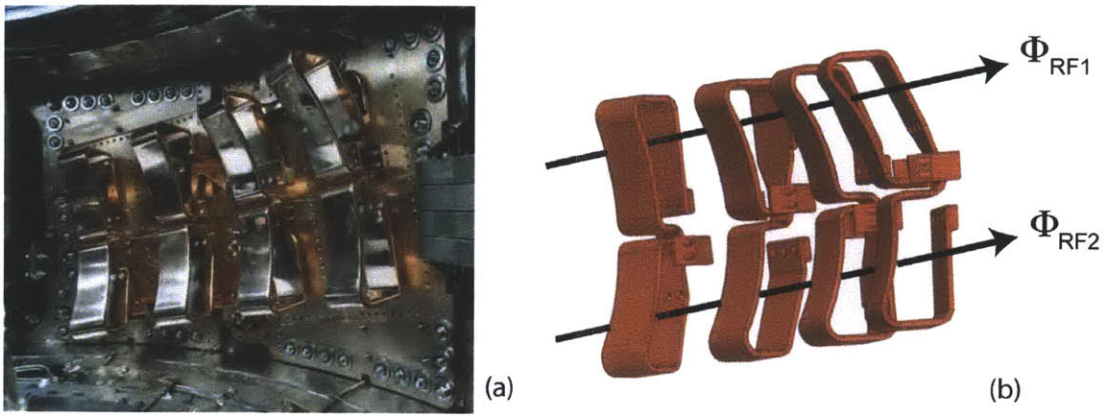

Figure 2-7: The field-aligned antenna straps are shown installed in C-Mod (a), beside a drawing illustrating the RF flux coupling of the loops in each strap (b). The RF magnetic flux through the upper set of loops Φ_{RF1} is designed to equal the flux through the lower loops Φ_{RF2}.

have the capability to vary the toroidal phase between straps. Typically [0, π, 0, π] and [0, π, π, 0] phasing are used for heating and [0, $\pm\pi/2$, $\pm\pi$, $\pm 3\pi/2$] phasing is used for co-current and counter-current drive. Toroidal phasing will be discussed in more detail in the next chapter.

Coaxial transmission line provides a low-loss transmission path from the four (2 MW) transmitters to the ICRF antennas. Most of the transmission line is filled with either air or dry nitrogen. However, in areas where high voltages are anticipated, sulfur hexafluoride (SF_6) gas is injected to increase the voltage standoff limits and prevent breakdown. The ratio of inner to outer conductor is set such that the impedance of the lines is 50 Ω, corresponding to a balance between voltage and power limits. Along the transmission lines, directional couplers are used to measure forward and reflected power. Demodulators in the data acquisition system provide phase information. In addition, voltage and current probes are used near high voltage and/or high current points in the system.

Impedance matching to the plasma is accomplished using a stub tuner and phase shifter which can be adjusted between discharges. In addition, the D and E-port antennas use a fast ferrite tuner (FFT) to adjust to load variations quickly $\sim 10^{-4}$ s during a discharge. The antenna loading changes rapidly as local density profiles

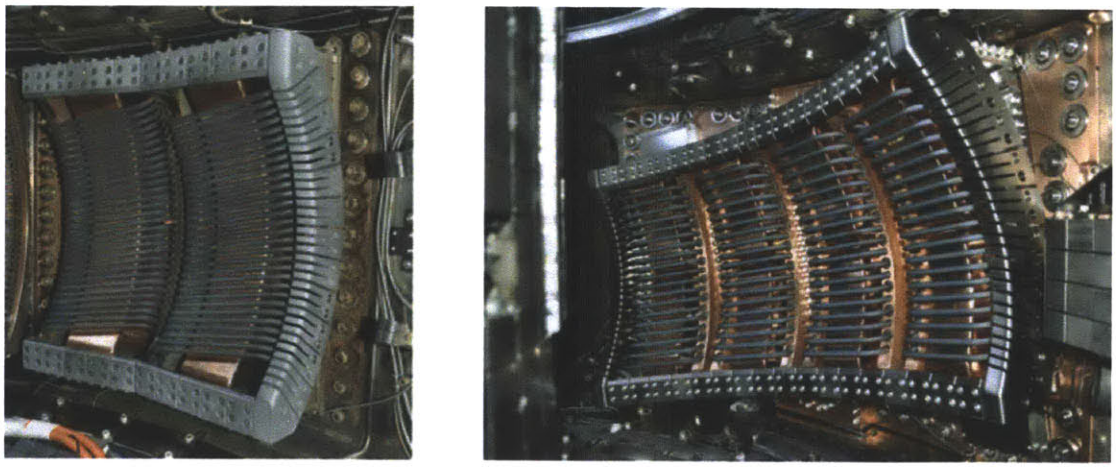

Figure 2-8: Alcator C-Mod E-port antenna (a), and field-aligned antenna, located at J-port (b).

fluctuate, and $\mathbf{E} \times \mathbf{B}$ turbulence forms in front of the antenna[22]. However, the fast wave cut-off layer in Alcator C-Mod is typically within 1-3 cm of the antenna straps, thus the evanescent region is usually very short, and ICRF coupling is generally better than other tokamaks.

One problem that is universally observed on tokamaks [2], including Alcator C-Mod [23], is an increase in impurities during ICRF operation. In ITER and in eventual reactors, enhanced impurity confinement establishes a very low tolerance for high-Z impurities [1]. High-Z impurities can cause significant radiation losses from the plasma, as well as dilution of the fuel. As a result, one of the primary challenges of ICRF heating is the reduction or elimination of impurities introduced into the plasma during ICRF operation, particularly for tokamaks with high-Z PFCs. ICRF-specific impurities, their origin, and mitigation techniques are the subject of the next chapter.

Chapter 3

ICRF Impurity characteristics

As described in the previous chapter, electromagnetic waves in the ion cyclotron range of frequencies (ICRF) are used to provide bulk auxiliary plasma heating in tokamaks like Alcator C-Mod, where high-Z metallic plasma facing components (PFCs) form the first wall. In ITER and in eventual reactors, enhanced impurity confinement due to internal transport barriers (ITBs) and H-mode operation establishes a very low tolerance ($\sim 1 \times 10^{-5}$ to 1×10^{-4}) for high-Z impurities [1]. Experiments have shown that impurity generation increases as ICRF power is increased [2]. As a result, one of the primary challenges of ICRF heating is the reduction/elimination of impurities introduced into the plasma during ICRF operation, particularly for tokamaks with high-Z PFCs.

3.1 Motivation

Impurities associated with ICRF auxiliary heating are universally observed [3, 4, 5, 6]. However, the underlying physics of ICRF-specific impurity generation is not well understood, and observations of impurity characteristics differ among various tokamak experiments. ICRF impurity accumulation is very machine-specific, depending on machine size, the overall geometry, the materials used, the conditioning of the machine, and on the chosen heating scenario [24].

The antenna Faraday shields on the Princeton Large Torus (PLT) were thought

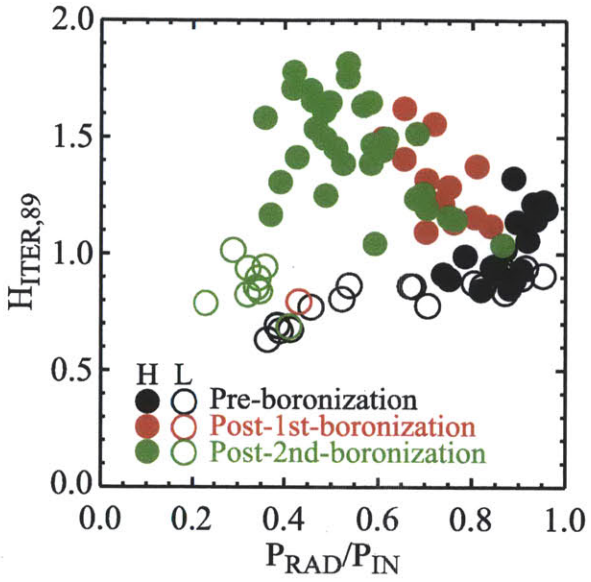

Figure 3-1: Alcator C-Mod plasma performance. Confinement quality ($H_{ITER,\,89}$) vs radiated power fraction (P_{RAD}/P_{IN}) shows decreasing performance in H-mode, with increasing radiated power. Reprinted with permission from [9]. Copyright 2006, American Institute of Physics.

to be the primary source of metallic impurities during ICRF heating[5]. Similarly, on Alcator C, spectroscopic observations revealed significant increases in iron impurity concentrations during ICRF heated discharges compared with ohmic discharges. In addition, a local temperature spike in the limiter shadow region was well correlated with the iron influx rate, suggesting that the Faraday shield was the primary source of metal impurities [6].

The Joint European Torus (JET) observed flattening of the density and temperature profiles in the scrape-off layer (SOL) and enhanced impurity and neutral influx during ICRF operation. Metallic impurity influx originating from the antenna Faraday screens (FS) was also observed along with a radially localized enhanced particle diffusivity across the plasma edge. This is especially true for toroidal antenna phasings with low-$k_{\|}$ [3]. The FS impurity influxes on JET were shown to depend on the antenna voltage, the density at the FS, the magnetic pitch angle, the toroidal antenna phasing, the FS geometry and the FS material. It was also found that replacing the carbon antenna limiters with beryllium limiters reduced impurity influxes by a factor

of two [25]. In addition, experiments on JET using four ICRF antennas with mixed toroidal phasing produced interesting results. During an L-mode discharge, when two antennas were phased in monopole [0, 0, 0, 0], and two were phased in [0, π, 0, π], strong interaction and arcing on one of the monopole antennas was observed. However, this interaction was not observed when all four antennas were phased in monopole, nor was it observed for an H-mode discharge [26]. In 2008, three different antenna phasings were compared: [0, π, 0, π], [0, π, π, 0], [0, 0, π, π]. The third case, referred to as *super dipole*, showed higher antenna-plasma coupling, but lower heating efficiency, higher local antenna temperature rise and much stronger plasma-wall interaction. The central temperature, stored energy, and neutron rate all decreased approximately 30% for the *super dipole* case relative to the others [27].

On the Tokamak EXperiment for Technology Oriented Research (TEXTOR), an ICRF generated direct current (DC) between a Faraday-shielded ICRF antenna and the wall of the tokamak increased almost an order of magnitude relative to the ohmic case. A corresponding density increase in the scrape-off layer (SOL) due to particle transport changes, and the generation of waves at harmonics of the RF generator frequency were attributed to RF sheaths [28]. TEXTOR data also show that DC sheath-rectified currents drawn by the energized ICRF antenna extend toroidally far away from the antenna and return via conducting objects in the machine [29]. In addition, a comparison on TEXTOR of an antenna with a FS and an antenna without a FS revealed no difference between the two antennas [30]

On the Tokamak Fusion Test Reactor (TFTR), titanium impurities from the Faraday screens increased substantially when the toroidal antenna phasing was changed from dipole [$0, \pi$] to monopole [0, 0] [31]. After numerous high-power discharges on TFTR, metal impurities migrated around the machine and were deposited on the limiters. This created a secondary source of titanium in addition to the Faraday screens. The global titanium concentration was found to depend strongly on antenna phasing [32]

Observations made on JT-60U suggest the ratio of radiation loss to ICRF power decreases with increasing ICRF power. In addition, radiated power saturates at less

than 10% at RF power levels of more than 4 MW. Observations suggested that low-Z impurity content correlates with ICRF power. However, high-Z impurities local to the antenna did not appear to be correlated with ICRF operation. [33].

On Tore Supra, antenna side limiters have shown overheating for ICRF power levels greater than 2 MW for dipole phasing or 1 MW for monopole phasing [34]. In addition, a poloidal variance and decrease in density is observed in front of the ICRF antenna on Tore Supra, along with a vertical asymmetry in local heat-flux and antenna erosion. These observations were attributed to $\mathbf{E} \times \mathbf{B}$ convection resulting from RF sheath formation [35]. Similarly, metallic impurity bursts have been associated with arcs and bright spots on the FS, and attributed to RF sheath formation [36]. Tore Supra impurity content was also observed to increase, while stored energy decreased, for monopole phasing relative to dipole phasing. In addition, antenna surface temperatures were shown to increase during monopole phasing [37].

On Alcator C-Mod, the primary impurity source locations were found to be the divertor, the inner wall and the ICRF antenna limiters. Of these sources, the limiter is typically the smallest in terms of absolute influx. However, it has a penetration factor:

$$PF = \frac{N_{\mathrm{Mo}}}{\Gamma_{\mathrm{Mo}}}, \tag{3.1}$$

where N_{Mo} represents the total impurity content and Γ_{Mo} corresponds to the source at the wall, an order of magnitude larger than the inner wall [38]. Presently, the outer divertor shelf appears to be the dominant source [39]. In addition, the plasma potential, measured on field lines connected to the active antenna is very high, often reaching hundreds of volts [38]. For C-Mod L-mode discharges, impurity characteristics were shown to be independent of phase, unlike observations on JET and TFTR [40]. Replacement of C-Mod molybdenum (Mo) antenna limiter tiles with boron nitride (BN) tiles did not decrease RF sheaths, nor did it change observed impurities [19]. To assess the effectiveness of boronization, the molybdenum tiles in C-Mod were cleaned to remove all boron. Then, discharges both before and after boronization were compared. The discharges with boronization had higher density and stored energy,

but lower radiated power than the discharges without boronization.

Operation of the 4-strap antenna on C-Mod without the Faraday screen showed significantly increased copper (Cu) influxes and degraded performance for both L-mode and H-mode plasmas [39]. Radiated power from consecutive H-mode discharges following a light boronization showed an increase in radiated power for discharges heated by same antenna. However, for consecutive discharges using different antennas, the radiated power was more controlled. This suggests that localized erosion is linked to the active ICRF antenna [23].

On ASDEX Upgrade (AUG) $E_{||}$ is found to be largest at the antenna side limiters when dipole toroidal phasing is used. However, $E_{||}$ is found to be largest at the septa when toroidal phasing other than dipole is used [41]. Image currents in the ICRF antenna box were shown to play a dominant role in parallel antenna near-fields in experiments on ASDEX Upgrade [42]. Reductions in high-Z impurity concentrations were achieved by increasing plasma-antenna clearance, using strong gas puffing, and decreasing the intrinsic light impurity content [43]. In addition, both boronization and edge localized mode (ELM) pace-making are effectively used to control tungsten (W) influxes on ASDEX Upgrade [44]. In addition, tungsten sputtering patterns were found to correlate with changes in parallel connection lengths at the antenna limiters [45]. Finally, when the toroidal magnetic was reversed, significantly less high-Z impurity influx was observed relative to operation with the typical field direction.

We see from these results that significant differences occur among observed impurity characteristics on different tokamaks, presumably because of the relative importance of various basic machine and plasma phenomena associated with each device. On Alcator C-Mod, data suggest that some impurities originate locally at the ICRF antenna; however, the primary impurity source is thought to be away from the antennas [40, 38]. ASDEX-Upgrade data indicate that the ICRF antenna limiters are the primary impurity source [44]. Additionally, JET results suggest that the faraday screens are responsible for most of the observed impurities [25]. While these observations are quite scattered, a common feature is an increased rate of impurity production, presumably through sputtering. This implicates RF-enhanced edge

sheath voltages which can lead to greatly increased sputter yield. In some sense this should not be surprising since ICRF heating by it very nature must impose large AC voltages in the boundary plasma in order to provide heating. Clearly this can have many negative consequences for impurity control. In all of these experimental cases it is thought that the underlying mechanisms are related to $E_{\|}$ and RF sheath rectification associated with ICRF operation.

3.2 Impurity production mechanisms

Generally, the observed increase in impurities with the onset of ICRF power is attributed to either a source mechanism, a transport mechanism, or both [46]. In the first hypothesis, impurities are generated by sputtering of PFCs by energetic ions [47]. In the second case, it is thought that spatial variation of potentials in front of the antenna establishes local $\boldsymbol{E} \times \boldsymbol{B}$ drifts that effect edge transport via formation of convective cells [48, 35]. In each case, the mechanism ultimately responsible for the increase in observed impurities is related to RF sheath formation [2].

3.2.1 RF sheaths

The electric potential of a DC plasma sheath is described by Poisson's equation:

$$\frac{\mathrm{d}^2\phi}{\mathrm{d}x^2} = \frac{e}{\varepsilon_0}\left(n_\mathrm{e} - n_\mathrm{i}\right), \tag{3.2}$$

where the electron density is given by a Boltzman distribution:

$$n_\mathrm{e} = n_0 \exp\frac{e\phi}{T_\mathrm{e}}. \tag{3.3}$$

The ion energy can be estimated through conservation of energy:

$$\frac{1}{2}m_\mathrm{i}v_\mathrm{i}^2 = \frac{1}{2}m_\mathrm{i}v_0^2 - e\phi. \tag{3.4}$$

From the assumption that $n_i v_i$ is constant within the sheath, we can calculate the ion density:

$$n_i = n_0 \left(\frac{\frac{1}{2} m_i v_0^2}{\frac{1}{2} m_i v_0^2 - e\phi} \right)^{1/2}, \tag{3.5}$$

where v_0 is the ion velocity as it enters the sheath [14]. Now Eq. 3.2 can be written:

$$\frac{\mathrm{d}^2\phi}{\mathrm{d}x^2} = \frac{n_0 e}{\varepsilon_0} \left[\exp\frac{e\phi}{T_e} - \left(\frac{\frac{1}{2} m_i v_0^2}{\frac{1}{2} m_i v_0^2 - e\phi} \right)^{1/2} \right]. \tag{3.6}$$

Assuming small ϕ, compared to T_e, and introducing the characteristic plasma scale length, the Debye length ($T_e = T_i$):

$$\lambda_D = \left(\frac{\varepsilon_0 T}{n e^2} \right)^{1/2}, \tag{3.7}$$

we can re-write Eq. 3.6 as:

$$\frac{\mathrm{d}^2\phi}{\mathrm{d}x^2} = \left(1 - \frac{T_e}{m_i v_0^2} \right) \frac{\phi}{\lambda_D^2}. \tag{3.8}$$

In order to obtain a spatially monotonic potential profile from the plasma to the sheath, the bracketed term in Eq. 3.8 must be positive. This condition requires a minimum velocity:

$$v_0 \geq \left(\frac{T_e}{m_i} \right)^{1/2}. \tag{3.9}$$

This is known as the Bohm sheath criterion and states that ions *must* enter the sheath at, or above, the sound speed ($v_0 \gtrsim c_s$). This has important implications for plasma material interaction (PMI), including sputtering where atoms are ejected from the surface of a material due to impacts from other atoms or ions. To calculate the potential drop across the sheath and mechanism for the acceleration of these ions, we satisfy the requirement that the electron current and ion current flowing to the material surface must be equal. The ion current is given by:

$$j_{\mathrm{i}} = n_0 e c_{\mathrm{s}}, \tag{3.10}$$

and the electron current is given by [14]:

$$j_{\mathrm{e}} = -\frac{1}{4} n_0 e \left(\frac{8T_{\mathrm{e}}}{\pi m_{\mathrm{e}}} \right)^{1/2} \exp \frac{e\phi_0}{T_{\mathrm{e}}}. \tag{3.11}$$

For ($T_{\mathrm{e}} = T_{\mathrm{i}}$), we can equate these current densities and solve for the sheath potential:

$$-\frac{e\phi_0}{T_{\mathrm{e}}} = \frac{1}{2} \ln \left[\frac{m_{\mathrm{i}}}{4\pi m_{\mathrm{e}}} \right], \tag{3.12}$$

which yields a potential of $\approx 3T_{\mathrm{e}}$ for deuterium.

The physics of DC sheaths translates to RF sheaths, where an oscillating voltage is applied to one or both electrode surfaces. Electrons escape from the plasma to one electrode and then the other at the location of highest applied voltage. This results in a parallel electron current which oscillates from one direction to the other across the electrode gap. The voltage in the gap increases and decreases at twice the RF frequency but is always higher than the voltage at the electrodes. As a result, the time-averaged potential along field lines between electrodes is always positive [49].

RF-rectification-enhanced sheaths form on open field lines, which terminate on PFCs and establish sheath potentials significantly higher than those formed across electrostatic sheaths ($V_{\mathrm{SH}} \gg 3k_{\mathrm{B}}T_{\mathrm{e}}$). RF sheaths arise from the nonlinear current response of the plasma to an applied voltage due to the high electron mobility compared to ions along the total magnetic field. As a result, a DC voltage forms along the magnetic field in response to an applied RF field to maintain ambipolarity. Thus, the primary driving mechanism for these sheaths is thought to be the RF electric field component parallel to the equilibrium magnetic field [47].

A simple picture of RF sheath rectification is illustrated in Fig. 3-2 using a basic current-voltage diode characteristic. When an RF voltage is applied, the electron current into a material surface is much higher than the ion current due to enhanced electron mobility compared with that of the ions. As a result, a DC rectification develops to to retard this "excess" electron current and maintain ambipolarity. Sim-

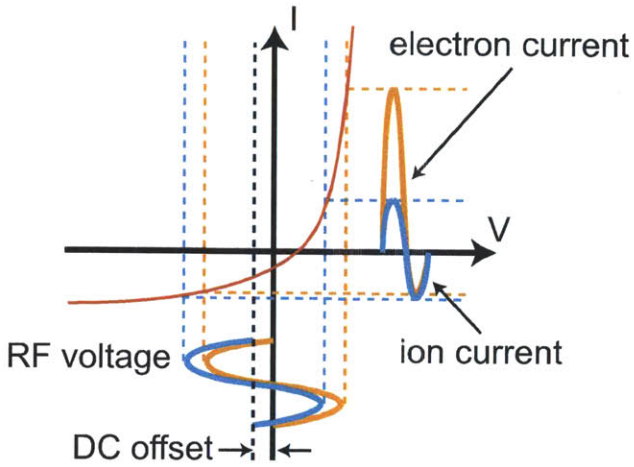

Figure 3-2: A simple picture of RF sheath rectification. When an RF voltage is applied, the electron current into a material surface is much higher than the ion current due to enhanced electron mobility compared with that of the ions. As a result a DC rectification develops to maintain ambipolarity.

ilarly, the schematic in Fig. 3-3 shows a pair of electrodes where an RF voltage is applied to one electrode. As the voltage swings from maximum to minimum, each electrode is alternatively biased negative relative to the other. The time average of this oscillation results in an average *positive* DC potential between the sheaths which form at either electrode. Such a mechanism increases the ion energy impacting the surface after acceleration through the sheath, enhancing the sputtering.

One mechanism that follows directly from rectification-enhanced sheath formation is physical sputtering of material inside the tokamak. When ions are accelerated through a large potential gradient, they can acquire sufficient energy and momentum to remove atoms from material lattice structure. Some intuition for this process can be gained using a simple classical treatment. The energy threshold where sputtering occurs is given by:

$$E_{\mathrm{T}} = \frac{E_{\mathrm{B}}}{\gamma_{\mathrm{sp}}\left(1-\gamma_{\mathrm{sp}}\right)}, \tag{3.13}$$

where E_{B} is the surface binding energy of the solid and the energy fraction transferred is:

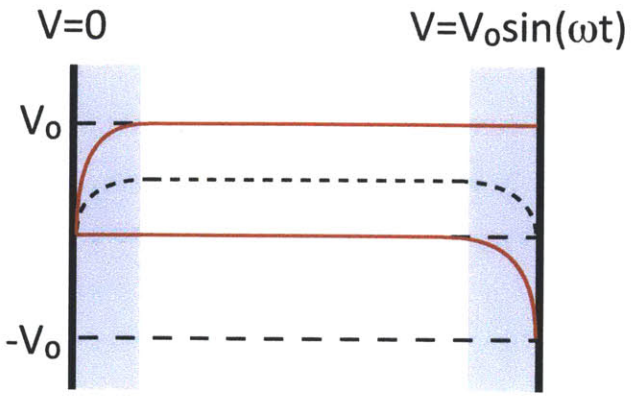

Figure 3-3: A simple schematic of sheath formation and steady state DC potential rectification between two electrodes, where an oscillating voltage is applied to one of the electrodes: The red lines correspond to the maximum and minimum RF voltage, and the dashed line represents the time-averaged potential.

$$\gamma_{\mathrm{sp}} = \frac{4 m_{\mathrm{inc}} m_{\mathrm{tar}}}{(m_{\mathrm{inc}} + m_{\mathrm{tar}})^2}, \tag{3.14}$$

where m_{inc} is the incident particle mass and m_{tar} is the target particle mass. For fixed surface density, mass ratio, collision cross section and mean free path of the incident ion in the target, the ratio of incident particle energy to threshold energy determines the sputtering yield. For a deuteron (2.01 u) incident on a molybdenum (95.94 u) target, a quick calculation using Eqs. 3.13 and 3.14, and surface binding energy of $\sim$ 6 eV, reveals a sputtering energy threshold of $\sim$ 80 eV. The sputtering yield can be combined with the ion flux through the sheath to calculate the total efflux of material sputtered from the target surface.

3.2.2 Fast wave parasitic coupling

Far-field RF sheaths and parasitic coupling of the launched fast wave to the slow wave can occur if the single pass absorption is low. In this case, the FW is not completely absorbed on one pass and therefore can reflect off the walls or limiters or cutoff surfaces within the plasma and couple to the SW [50]. In this model, the parallel component of the SW electric field drives an RF sheath, similar to the description

given in Sec. 3.2.1. This SW generated sheath can increase sputtering of impurities from material surfaces inside the tokamak. Because toroidal phasings with higher launched $k_{||}$ have better core absorption, the increased impurity response observed with monopole phasing is thought to result from this mechanism in areas far from the antenna structure [24].

In tokamak plasmas with high single pass absorption very little energy is coupled to the SW. In this case, antenna near-field effects tend to dominate impurity generation and transport. This model suggests that RF magnetic flux in circuits formed by field lines and Faraday screen components produces an $E_{||}$ that drives local sputtering [47].

3.2.3 $E \times B$ convection

The potentials formed as a result of RF sheath rectification have strong gradients in both the poloidal and radial directions. The poloidal electric fields E_θ and radial electric fields E_r combine with the magnetic field to drive $\mathbf{E} \times \mathbf{B}$ convection. This convection contributes to a flattening of the density profile in front of the antenna observed on several tokamaks [32]. An increase in plasma flux toward the antenna enhances the antenna-plasma interactions. When field lines in front of an active antenna charge up to different potentials, an electric field forms between them. The direction of the toroidal magnetic field determines whether plasma convection is either toward the top or bottom of the antenna [49]. In this way, the launched waves not only alter the edge turbulence and transport mechanisms, but also change the density in front of the antenna which results in changes to the antenna coupling efficiency.

3.2.4 Proposed solutions

Several methods have been proposed to reduce ICRF-specific impurity characteristics. Coatings of low-Z elements such as boron on top of high-Z PFCs can be beneficial by essentially *hiding* the high-Z elements from sputtering. This is effective because low-Z elements are much less damaging to core plasma performance since they become fully stripped of electrons. Boronization [7] is one such coating, which has achieved good

experimental results. Application of a thin coating of boron (Z = 5) over the C-Mod molybdenum (Z = 42) walls, limiters and antennas, resulted in considerably higher plasma stored energy and significantly lower radiated power [23].

Toroidal phasing of straps on ICRF antennas also has a measurable effect on RF sheath potentials and observed impurity production [31, 32, 8]. Typically, ICRF antennas are operated in dipole phasing $[0, \pi, 0, \pi]$ due to the deleterious effects of monopole phasing $[0, 0, 0, 0]$. As described above, these effects include increased plasma impurity content [3, 31], hot-spot formation [37], and arcing [26]. This is likely because the cancellation of $E_{\|}$ along field lines is greater for dipole phasing than for monopole phasing for antenna structures which are not aligned with the equilibrium magnetic field [8, 51]. Simulations of the ITER-like antenna (ILA) on Tore Supra showed the highest DC rectified potentials for [0, 0, π, π] phasing, and the lowest potentials for [0, π, 0, π] phasing, with [0, π, π, 0] in between [52]. Similar results have been observed on JET [3, 25, 27], Tore Supra [34], TFTR [31], and ASDEX Upgrade [41]

Alignment of Faraday screen elements with the total magnetic field has been shown decrease RF sheaths and observed impurities [8]. Numerical work on the ASDEX Upgrade antennas found that $E_{\|}$ could be mitigated several ways: by increasing the toroidal distance between the antenna side limiters, septa and current straps; by increasing the number of straps toroidally; and by better cancellation of image currents in the antenna structure [43]. Another technique for mitigating RF sheaths, which is particularly appealing from a symmetry perspective, is antenna rotation [4], i.e. the face remains parallel to the SOL flux surfaces but the antenna straps have varying orientation to the local B field. On Alcator C-Mod we have designed a new magnetic field-aligned ICRF antenna to minimize ICRF-specific impurity characteristics. Chapter 4 describes the 3-D finite element method (FEM) simulation model developed to quantify the effect of magnetic field-antenna alignment on $E_{\|}$ and RF sheath effects.

Chapter 4

Finite element method simulation

4.1 Initial modeling and design

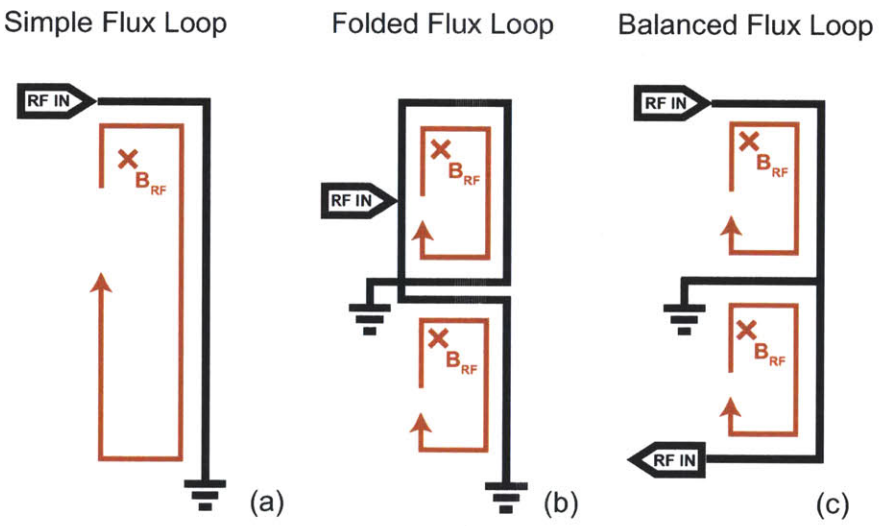

Figure 4-1: Basic design topologies for consideration as inductive flux coupling ICRF structures. A simple loop is shown in (a), a folded loop is shown in (b), and an end-fed center-grounded loop is shown in (c).

Initial design considerations for the rotated antenna included maximizing RF magnetic flux coupled to the plasma, minimizing voltage breakdown across gaps in the antenna and transmission line structures, and minimizing the effects of the RF electric field parallel to the total magnetic field. In 2008, Steve Wukitch and Pete Koert

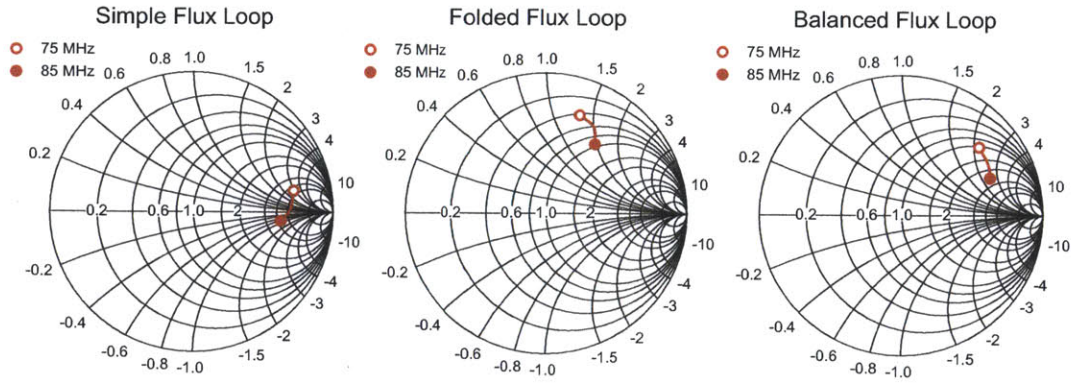

Figure 4-2: Smith chart display of reflected power for the geometries shown schematically in Fig. 4-1. A simple loop is shown in (a), a folded loop is shown in (b), and an end-fed center-grounded loop is shown in (c).

began investigating antenna designs based upon the existing Alcator C-Mod antennas. As mentioned previously, the end-fed center-grounded 2-strap designs installed at D-port and E-port [18, 20] in the machine performed better than the folded 4-strap antenna installed at J-port [21]. However, geometry and power handling requirements limit each horizontal port on C-Mod to four coaxial power feed lines. As a result, the design choices for an inductively coupled ICRF antenna are limited. Either the design is limited to two straps with two inputs per strap, or the antenna can include up to four straps if each one is fed individually. We began investigating the effects of various basic strap topologies to ascertain loading characteristics and general performance.

In Fig. 4-1 (a) the most basic inductive coupling loop is shown. Here, a rectangular current strap is fed via coaxial input at one end while the other end is grounded. While quite simple in design, the effectiveness of this approach is limited because the distribution of RF magnetic flux is not uniform within the loop. This degrades the inductive coupling effectiveness. The loops shown in Fig. 4-1 (b) and (c) improve this design issue by dividing the main flux loop into two separate loops to better control the distribution of RF flux.

In Fig. 4-2 the complex reflection coefficient is plotted for the three cases shown in Fig. 4-1. Although the total coefficient is similar for the three designs at 80 MHz, the folded design yields a slightly lower value. All three loops were numerically

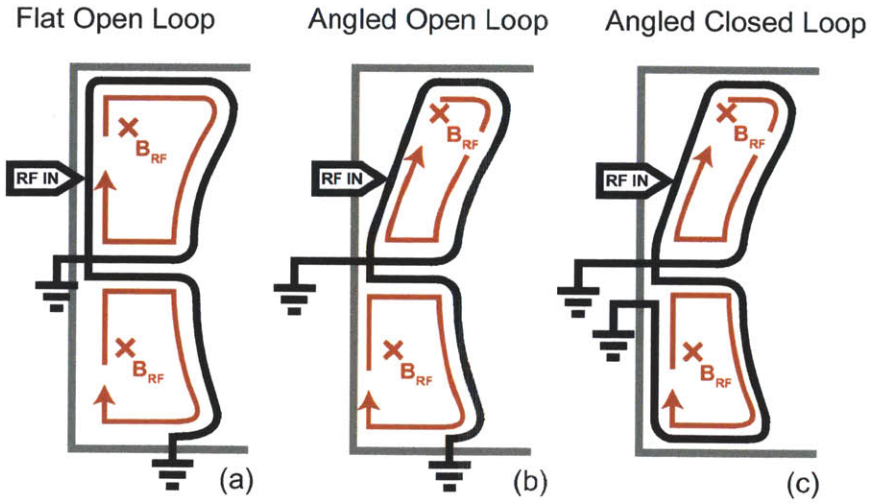

Figure 4-3: Folded strap design topologies. Flat backed open strap is shown in (a), an angled back open strap is shown in (b), and an angled back closed strap is shown in (c).

loaded with a graduated dielectric in slab geometry. The load consisted of an isotropic dielectric ($K_D = 150$), with a series of five 1 mm thick steps ($K_D = 50$) to ($K_D = 150$) at the vacuum dielectric transition. Scattering boundary conditions were implemented to prevent reflected waves at the boundaries.

Open loop designs, shown in Fig. 4-3 (a) and (b), were initially investigated. These designs created larger flux loops by allowing currents to return within the antenna box itself. However, as can be seen from Fig. 4-4, the complex reflection coefficient was found to be higher relative to the closed loop design. In addition, the RF magnetic flux distribution within the open section of the loop was not uniform. By closing the second loop section, the RF current driving the magnetic flux was forced to remain relatively uniform around the perimeter of the loop. Consequently, the magnetic flux in the second loop became more evenly distributed. As a result, an up-down magnetic flux symmetry was restored by creating equal area loops with similar strap current distributions. This is important for launching waves which propagate into the plasma normal to flux surfaces. This design, Fig. 4-3 (c), was eventually chosen for the baseline for the field-aligned antenna. To better understand the effects of antenna

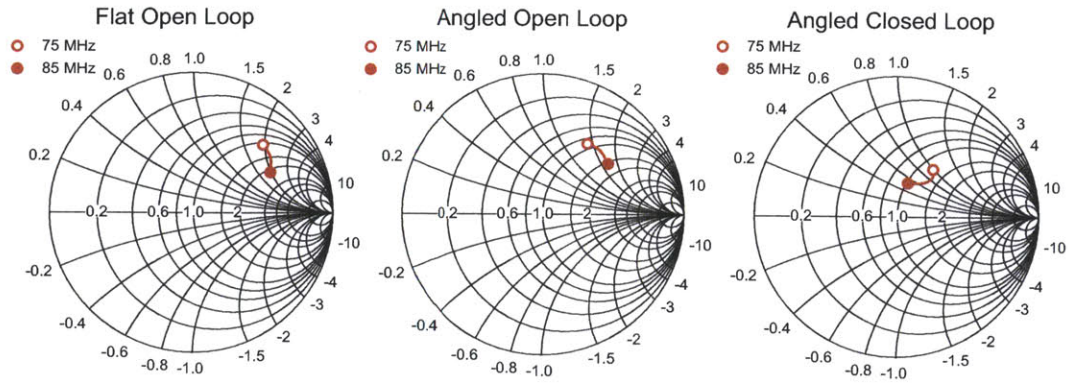

Figure 4-4: Smith chart display of reflected power for the geometries shown schematically in Fig. 4-3. Flat backed open strap is shown in (a), an angled back open strap is shown in (b), and an angled back closed strap is shown in (c).

topology on the parallel RF electric field, RF sheaths, and impurity production and transport, a cold plasma model was developed and implemented in 3D slab, cylindrical and toroidal geometry.

4.2 Cold plasma RF model: slab geometry

Full wave codes, which solve Maxwell's equations directly inside a plasma model, are typically implemented in the spectral domain. Spectral solvers such as TORIC [53] and AORSA [54], and hybrid spatial / spectral solvers such as TOPICA [55] have achieved good results simulating ICRF heating in tokamaks. More recently, finite element method (FEM) full wave codes have been successfully implemented entirely in the spatial domain [56, 57]. Full FEM codes have several advantages over spectral solvers for ICRF simulation, including the capability to include complex three dimensional (3-D) antenna structures and SOL details that play an important role in coupling and $E_{\|}$ generation. In addition, FEM generally produces numerically sparse matrices, an important consideration for the solution of large electromagnetic problems [58].

For this study, we have utilized the FEM model described below to solve Maxwell's

equations for the electric field $\boldsymbol{E}$, in 3-D slab geometry:

$$\nabla \times \nabla \times \boldsymbol{E} = \frac{\omega^2}{c^2} \overleftrightarrow{\epsilon} \cdot \boldsymbol{E} \tag{4.1}$$

where $\overleftrightarrow{\epsilon}$ is the cold plasma dielectric tensor [15]:

$$\overleftrightarrow{\epsilon} = \begin{bmatrix} S & -\mathrm{i}D & 0 \\ \mathrm{i}D & S & 0 \\ 0 & 0 & P \end{bmatrix}, \tag{4.2}$$

with the sum (S), difference(D), and plasma(P) components, given by:

$$S = 1 - \frac{\omega_{\mathrm{pe}}^2}{(\omega^2 - \omega_{\mathrm{ce}}^2)} - \frac{\omega_{\mathrm{pi}}^2}{(\omega^2 - \omega_{\mathrm{ci}^2})}, \tag{4.3}$$

$$D = -\frac{\omega_{\mathrm{ce}}\omega_{\mathrm{pe}}^2}{\omega\,(\omega^2 - \omega_{\mathrm{ce}}^2)} + \frac{\omega_{\mathrm{ci}}\omega_{\mathrm{pi}}^2}{\omega\,(\omega^2 - \omega_{\mathrm{ci}}^2)}, \tag{4.4}$$

$$P = 1 - \frac{\omega_{\mathrm{pe}}^2}{\omega^2} - \frac{\omega_{\mathrm{pi}}^2}{\omega^2}, \tag{4.5}$$

for a single ion species in Cartesian coordinates [15]. Here, $\omega_{\mathrm{p}j}^2$, and $\omega_{\mathrm{c}j}^2$ represent the plasma and cyclotron frequencies, respectively, for the j^{th} particle species. A simple 1/R magnetic field is used with $\mathbf{B} = \mathrm{B}_0\hat{\mathrm{z}}$, given by:

$$\mathbf{B} = \frac{B_0 R_0}{R}\phi \quad \rightarrow \quad \mathbf{B} = \frac{B_0 R_0}{x}\hat{\mathrm{z}}. \tag{4.6}$$

In this Cartesian slab model, Stix coordinates [15] are used such that: $\mathbf{B} \parallel \hat{\mathrm{z}}$, $\nabla\mathbf{B} \parallel \hat{\mathrm{x}}$, and $\mathbf{B}$, $\nabla\mathbf{B} \perp \hat{\mathrm{y}}$. A simple parabolic density profile is used of the form:

$$n(x/a) = n_{\mathrm{edge}} + (n_0 - n_{\mathrm{edge}})\left(1 - (x/a)^2\right), \tag{4.7}$$

where n_0 represents the central density of the plasma, and n_{edge} represents the density at the edge. Ion and electron density are set to be equal ($n_{\mathrm{i}} = n_{\mathrm{e}}$). The central density is $n_0 = 2 \times 10^{20}$ m^{-3}, and the edge density is $n_{\mathrm{edge}} = 5 \times 10^{18}$ m^{-3}. A radiation

boundary condition is used to prevent standing waves within the simulation domain. It should also be noted that a 1 cm vacuum gap is imposed between the plasma and the antenna structure. Following simulations with slab geometry, a 3D cold plasma model was implemented in toroidal geometry.

4.3 Cold plasma RF model: toroidal geometry

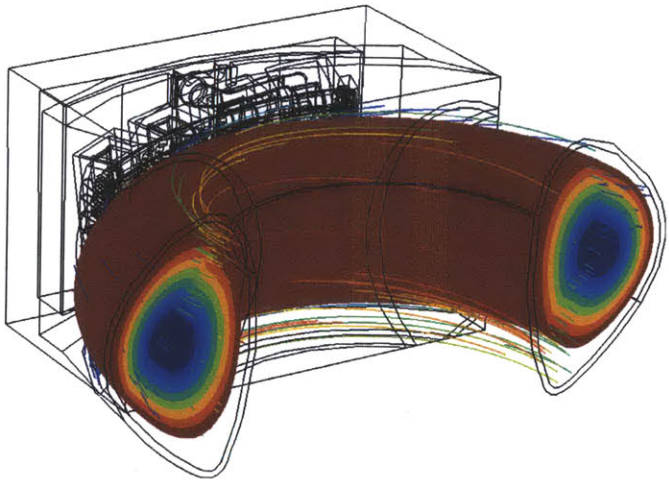

Figure 4-5: Simulation model showing 3-D magnetic flux surfaces reconstructed from EFIT [10].

To quantify the effects of antenna orientation on $E_{\|}$ in actual experiments, a 3-D toroidal plasma model was adopted. For this study, we have utilized the FEM model described below to solve Maxwell's equations for the electric field $\boldsymbol{E}$, in 3-D toroidal geometry:

$$\nabla \times \nabla \times \boldsymbol{E} = \frac{\omega^2}{c^2} \overleftrightarrow{\epsilon} \cdot \boldsymbol{E} \tag{4.8}$$

where $\overleftrightarrow{\epsilon}$ is the cold plasma dielectric tensor [15]:

$$\overleftrightarrow{\epsilon} = \begin{bmatrix} S & -\mathrm{i}D & 0 \\ \mathrm{i}D & S & 0 \\ 0 & 0 & P \end{bmatrix}, \tag{4.9}$$

with the sum (S), difference(D), and plasma(P) components, given by

$$S = 1 - \sum_j \frac{\omega_{pj}^2}{\omega} \frac{\omega + i\nu_j}{(\omega + i\nu_j)^2 - \omega_{cj}^2}, \tag{4.10}$$

$$D = \sum_j \frac{\omega_{pj}^2}{\omega} \frac{\omega_{cj}}{(\omega + i\nu_j)^2 - \omega_{cj}^2}, \tag{4.11}$$

$$P = \sum_j \frac{\omega_{pj}^2}{\omega(\omega + i\nu_j)}. \tag{4.12}$$

Artificial collisional damping is included by introducing the collision frequency ν_j into the cold plasma two-fluid momentum equations, and ω_{pj}^2, and ω_{cj}^2 represent the plasma and cyclotron frequencies, respectively, for the j^{th} particle species. The electron-ion collision frequency is given by [12]:

$$\nu_{ei} \approx \left(\frac{1}{4\pi} \frac{e^4 n_i}{\varepsilon_0^2 m_e m_\mu} \ln\Lambda \right) \frac{1}{v_{Te}^3}, \tag{4.13}$$

where the electron thermal velocity v_{Te} is defined as:

$$v_{Te} = \left(\frac{2T_e}{m_e} \right)^{\frac{1}{2}}, \tag{4.14}$$

the reduced mass, m_μ is given by:

$$m_\mu = \frac{m_e m_i}{m_e + m_i}, \tag{4.15}$$

and the Coulomb logarithm is given by:

$$\Lambda = \frac{12\pi\varepsilon_0^{3/2} T_e^{3/2}}{n_e^{1/2} e^3}. \tag{4.16}$$

The ion-electron collision frequency simply differs from the electron-ion collision frequency by the electron-ion mass ratio:

$$\nu_{ie} = \frac{m_e}{m_i} \nu_{ei}, \tag{4.17}$$

The dielectric tensor shown in Eq. (4.9) is rotated to describe an axisymmetric toroidal plasma. Rotation of the cold plasma permittivity tensor requires rotation through spatial Euler angles θ and α. Here, θ represents the local poloidal coordinate, and α represents the local pitch coordinate within the intermediate reference frame. Rotation is accomplished from the right-handed x-y-z cartesian system to an X-Y-Z system where the relevant rotation matrices are:

$$R_\theta = \begin{bmatrix} \cos\theta & -\sin\theta & 0 \\ \sin\theta & \cos\theta & 0 \\ 0 & 0 & 1 \end{bmatrix}, \tag{4.18}$$

and

$$R_\alpha = \begin{bmatrix} 1 & 0 & 0 \\ 0 & \cos\alpha & -\sin\alpha \\ 0 & \sin\alpha & \cos\alpha \end{bmatrix}. \tag{4.19}$$

Rotation of the cold plasma permittivity tensor takes the form:

$$\epsilon_{\text{rotated}} = R \cdot \epsilon \cdot R^T, \tag{4.20}$$

where R=$R_\theta \cdot R_\alpha$, and is given by

$$R = \begin{bmatrix} \cos\theta & -\sin\theta\cos\alpha & \sin\theta\sin\alpha \\ \sin\theta & \cos\theta\cos\alpha & -\cos\theta\sin\alpha \\ 0 & \sin\alpha & \cos\alpha \end{bmatrix}, \tag{4.21}$$

and the transpose of R, $R^T = (R_\theta \cdot R_\alpha)^T$ is given by:

$$R^T = \begin{bmatrix} \cos\theta & \sin\theta & 0 \\ -\sin\theta\cos\alpha & \cos\theta\cos\alpha & \sin\alpha \\ \sin\theta\sin\alpha & -\cos\theta\sin\alpha & \cos\alpha \end{bmatrix}. \tag{4.22}$$

First, we rotate twice in the original xyz frame:

$$R \cdot \boldsymbol{\epsilon} = \begin{bmatrix} \cos\theta & -\sin\theta\cos\alpha & \sin\theta\sin\alpha \\ \sin\theta & \cos\theta\cos\alpha & -\cos\theta\sin\alpha \\ 0 & \sin\alpha & \cos\alpha \end{bmatrix} \begin{bmatrix} S & -\mathrm{i}D & 0 \\ \mathrm{i}D & S & 0 \\ 0 & 0 & P \end{bmatrix} =$$

$$\begin{bmatrix} S\cos\theta - \mathrm{i}D\sin\theta\cos\alpha & -\mathrm{i}D\cos\theta - S\sin\theta\cos\alpha & P\sin\theta\sin\alpha \\ S\sin\theta + \mathrm{i}D\cos\theta\cos\alpha & -\mathrm{i}D\sin\theta + S\cos\theta\cos\alpha & -P\cos\theta\sin\alpha \\ \mathrm{i}D\sin\alpha & S\sin\alpha & P\cos\alpha \end{bmatrix} \tag{4.23}$$

Then we rotate via R^T to move to final coordinate system XYZ:

$$R \cdot \boldsymbol{\epsilon} \cdot R^T = \begin{bmatrix} S\cos\theta - \mathrm{i}D\sin\theta\cos\alpha & -\mathrm{i}D\cos\theta - S\sin\theta\cos\alpha & P\sin\theta\sin\alpha \\ S\sin\theta + \mathrm{i}D\cos\theta\cos\alpha & -\mathrm{i}D\sin\theta + S\cos\theta\cos\alpha & -P\cos\theta\sin\alpha \\ \mathrm{i}D\sin\alpha & S\sin\alpha & P\cos\alpha \end{bmatrix} \cdot$$

$$\begin{bmatrix} \cos\theta & \sin\theta & 0 \\ -\sin\theta\cos\alpha & \cos\theta\cos\alpha & \sin\alpha \\ \sin\theta\sin\alpha & -\cos\theta\sin\alpha & \cos\alpha \end{bmatrix},$$

yielding components:

$$\epsilon_{xx} = S\cos^2\theta - \cancelto{0}{iD\sin\theta\cos\alpha\cos\theta} + \cancelto{0}{iD\cos\theta\sin\theta\cos\alpha} + S\sin^2\theta\cos^2\alpha + P\sin^2\theta\sin^2\alpha$$

$$\epsilon_{xy} = S\sin\theta\cos\theta + iD\cos^2\theta\cos\alpha + iD\sin^2\theta\cos\alpha - S\cos\theta\sin\theta\cos^2\alpha - P\cos\theta\sin\theta\sin^2\alpha$$

$$\epsilon_{xz} = iD\sin\alpha\cos\theta - S\sin\alpha\sin\theta\cos\alpha + P\cos\alpha\sin\theta\sin\alpha$$

$$\epsilon_{yx} = S\cos\theta\sin\theta - iD\sin^2\theta\cos\alpha - iD\cos^2\theta\cos\alpha - S\sin\theta\cos\theta\cos^2\alpha - P\sin\theta\cos\theta\sin^2\alpha$$

$$\epsilon_{yy} = S\sin^2\theta + \cancelto{0}{iD\cos\theta\sin\theta\cos\alpha} - \cancelto{0}{iD\sin\theta\cos\theta\cos\alpha} + S\cos^2\theta\cos^2\alpha + P\cos^2\theta\sin^2\alpha$$

$$\epsilon_{yz} = iD\sin\alpha\sin\theta + S\sin\alpha\cos\theta\cos\alpha - P\cos\alpha\cos\theta\sin\alpha$$

$$\epsilon_{zx} = -iD\cos\theta\sin\alpha - S\sin\theta\cos\alpha\sin\alpha + P\sin\theta\sin\alpha\cos\alpha$$

$$\epsilon_{zy} = -iD\sin\theta\sin\alpha + S\cos\theta\cos\alpha\sin\alpha - P\cos\theta\sin\alpha\cos\alpha$$

$$\epsilon_{zz} = S\sin^2\alpha + P\cos^2\alpha.$$

These components form the dielectric tensor used in the toroidal model:

$$\overleftrightarrow{\epsilon}_{\text{rotated}} = \begin{bmatrix} \epsilon_{xx} & \epsilon_{xy} & \epsilon_{xz} \\ \epsilon_{yx} & \epsilon_{yy} & \epsilon_{yz} \\ \epsilon_{zx} & \epsilon_{zy} & \epsilon_{zz} \end{bmatrix}. \tag{4.24}$$

This model uses experimental data from Alcator C-Mod. Magnetics data from EFIT [10] are used to reconstruct accurate 3-D magnetic fields in the model. Here, 2-D poloidal magnetic field reconstruction is combined with the toroidal magnetic field to produce a 3-D map of the total magnetic field, shown in Fig. 4-6. The reconstructed 3-D flux surfaces are shown in Fig. 4-5. These flux surfaces extend beyond the solution domain shown in Fig. 4-8 simply for visualization purposes. Three dimensional density and temperature profiles are reconstructed from Alcator C-Mod Thompson scattering data [59]. The 1-D radial profiles used are shown in Fig. 4-7. The locations of the main plasma limiter, ICRF limiter, ICRF antenna strap and vacuum region are shown as a function of major radius. In addition, detailed 3-D

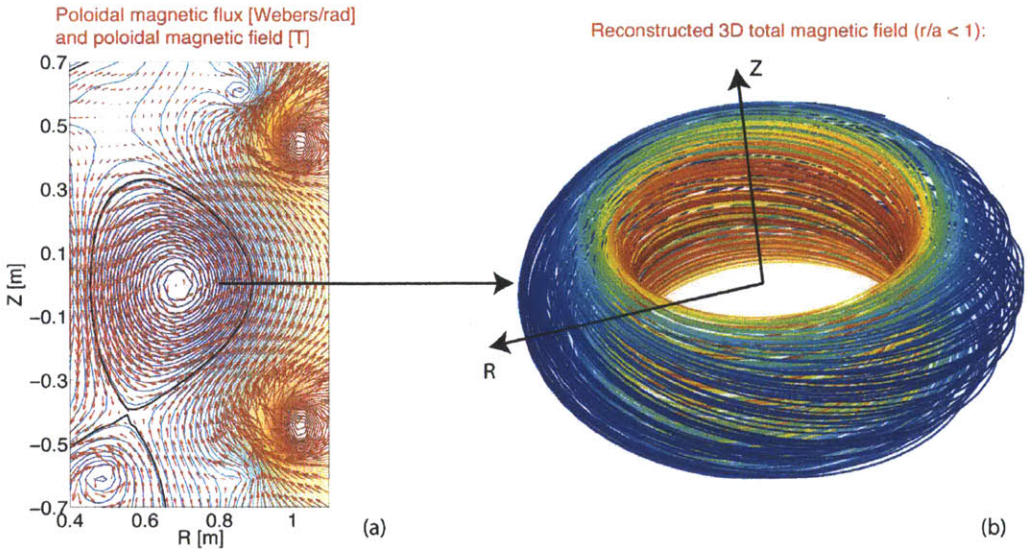

Figure 4-6: Poloidal magnetics data from EFIT (a) are combined with toroidal field data to reconstruct the total magnetic field inside Alcator C-Mod (b).

computer aided design (CAD) assemblies of the ICRF antenna and vacuum vessel are included in the simulation. The new Alcator C-Mod ICRF antenna, rotated 10 degrees to provide symmetry with respect to the total magnetic field is shown in 4-9(a). The FEM model geometry, including the field-aligned antenna and evaluation flux surface is shown in 4-9(b).

Simulations are carried out using this cold plasma model with data from lower single null deuterium discharges with a hydrogen minority D(H) concentration of $n_H/n_D = 0.05$. The plasma parameters used are: elongation $\kappa = 1.7$, upper triangularity $\delta_u = 0.31$, lower triangularity $\delta_l = 0.55$, magnetic field on axis $B_0 = 5.4$ T, density on axis $n_0 = 2.1 \times 10^{20}\mathrm{m}^{-3}$ and at the plasma edge $n_s = 1.0 \times 10^{19}\mathrm{m}^{-3}$, temperature on axis $T_0 = 2$ keV and at temperature at the plasma edge $T_s = 100$ eV. In addition, the cold plasma model was compared with a lossy dielectric model. This dielectric model includes a set of spatial domains separated into discrete steps within the scrape-off-layer (SOL). Each dielectric domain is assigned a relative permittivity and loss tangent to mimic measured density profiles and observed antenna loading. Similar to previous work [60], the choice of dielectric constant approximately equal to the square of the speed of light divided by the Alfven speed $K_D \approx (c/V_A)^2$, is found

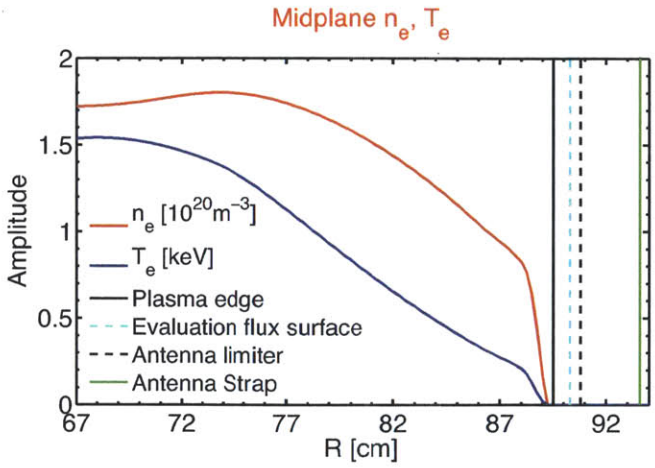

Figure 4-7: Midplane density and temperature profile curve fits from Thompson scattering data. 3D density and temperature profiles were reconstructed by mapping these profiles onto flux surfaces obtained from EFIT.

to provide qualitatively-similar results to the cold plasma model described above.

Surfaces and volumes within the model are meshed using quadratic finite elements; approximately 3 million degrees of freedom are typical. Finite element method codes are fundamentally well suited to model complicated 3-D geometry. However, in practice, incorporating complex 3-D structures into simulation models and properly meshing them is non-trivial. For these simulations, much attention was given to incorporating fine details of the model geometry which might impact the relevant physics of the problem. At the same time, unnecessary details were omitted whenever possible for numerical considerations. Meshing of structures (where finite element nodes are mapped onto the spatial domain of the model), was done programmatically to ensure an optimum mesh distribution. In this way, fine structures purposely included in the model were not assigned too many mesh nodes. Likewise, large areas of the model were assigned a sufficient mesh density to assure proper convergence of the solution.

Similar to the slab model, a radiation boundary condition (RBC) is used to prevent standing waves within the simulation domain. Most of the wave energy is damped within the plasma through the inclusion of artificial collisionality, or loss tangent in the case of dielectric. However, the RBC prevents large reflections at the domain

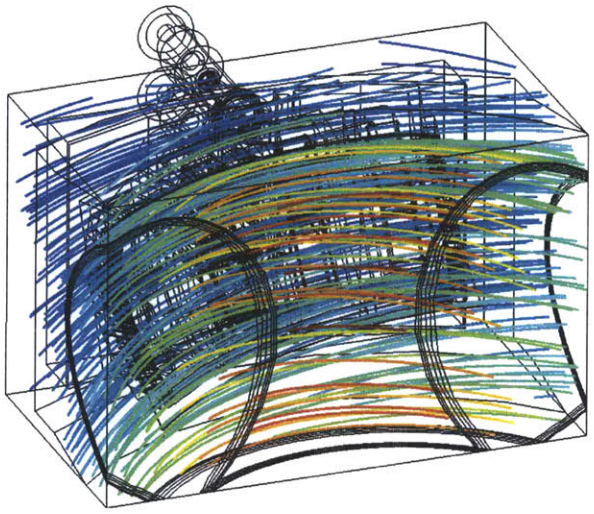

Figure 4-8: Simulation domain showing total magnetic field.

boundaries from waves not completely damped within the plasma. The extent of the simulation domain is shown in Fig. 4-8. Here, the total magnetic field is shown for reference in front of the field-aligned antenna. It should also be noted that a 1 cm vacuum gap is imposed between the plasma and the antenna structure.

4.4 Field-aligned antenna model

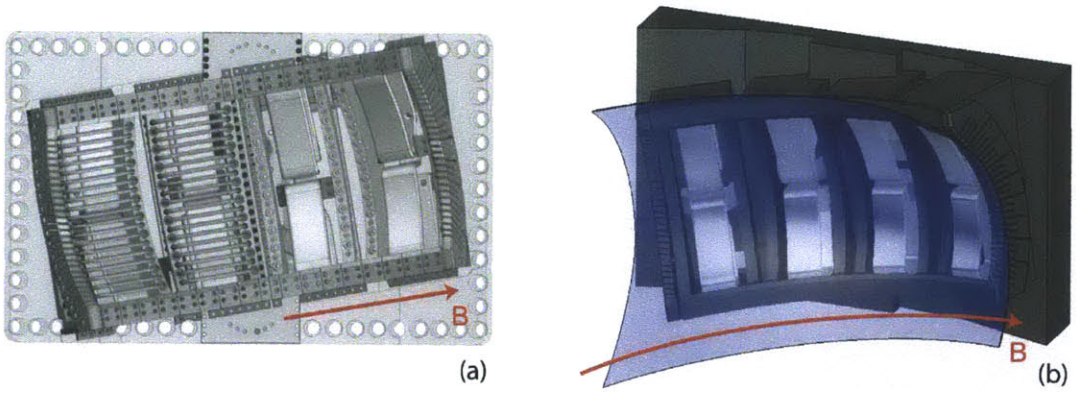

Figure 4-9: The new Alcator C-mod ICRF antenna (a), is rotated 10 degrees to provide symmetry with respect to the total magnetic field. FEM model geometry is shown in (b): field-aligned antenna and evaluation flux surface 0.5 cm in front of antenna private side limiters. Faraday rods are removed from the image for clarity.

Alcator C-Mod uses three ICRF antennas to provide auxiliary heating power. Two of the antennas contain two poloidal straps each, and have been in use on the machine since 1994 [20]. The third antenna is a 4-strap antenna. The 4-strap antenna used from 1998 until 2011 was aligned horizontally in the machine [21]. As mentioned in Ch. 3, misalignment of ICRF antenna components with the magnetic field is thought to contribute poor $E_{||}$ cancellation, RF sheath formation and impurity accumulation. To ameliorate these issues, and minimize the integrated RF $E_{||}$, a new field-aligned ICRF antenna (shown in Fig. 4-9) was designed to have symmetry along the total magnetic field. This required rotation of the antenna due to the finite poloidal/vertical field at the boundary.

The antenna is based upon the previous, horizontal 4-strap ICRF antenna [21]. Both antennas feature a folded strap design utilizing a single coaxial line input for each strap. However, the new antenna is rotated 10 degrees with respect to horizontal, to provide symmetry across the typical magnetic pitch angle at the plasma edge (corresponding to $B_{\mathrm{T}} = 5.4$ T and $I_{\mathrm{p}} = 1$ MA, depending on plasma shaping). Although the shape of each antenna strap is not symmetric about the antenna midplane, the poloidal strap loops are designed to enclose the same magnetic flux. This is important not only because of increased $E_{||}$ cancellation, but also because ICRF antennas function as magnetic flux coupling structures. Most of the energy density of the fast magnetosonic wave (FW) is contained in the RF magnetic field or the oscillating ion velocities [61]. As a result, the energy that can be carried into the plasma by the FW is set by the magnetic coupling effectiveness of the antenna.

Initially, slab and cylindrical simulations of existing C-mod antennas were developed to establish a baseline for optimization of the new field-aligned antenna. Subsequently, toroidal models were implemented to characterize wave propagation, antenna coupling, and $E_{||}$ in Alcator C-Mod geometry. The cold plasma model described in Sec. 4.3 was compared with a lossy dielectric model. Results for conventional ICRF antennas (i.e. poloidal antenna straps not aligned with the total magnetic field) were consistent with experimental observations on numerous tokamaks [3, 31, 26]. However, simulations suggest that cancellation of $E_{||}$ should be significantly higher for an

ICRF antenna structure aligned with the magnetic field. These simulation results will be presented in Ch. 5.

Chapter 5

Simulation results

5.1 Slab and cylindrical geometry

Simulations of the existing C-mod antennas were developed to establish a baseline for optimization of the new field-aligned antenna. For these conventional ICRF antennas (i.e. poloidal antenna straps not aligned with the total magnetic field), cancellation of $E_{\|}$ was found to be larger for dipole toroidal phasing of straps $[0, \pi]$, relative to monopole phasing $[0, 0]$. Similar results were obtained for both slab and cylindrical geometries and are consistent with experimental observations on numerous tokamaks [3, 31, 26]. However, for a symmetrical ICRF antenna aligned with the magnetic field, monopole phasing produced almost complete cancellation of $E_{\|}$. This was surprising because it is opposite to both previous experimental results and simulations for non-aligned ICRF antennas.

Initial simulations were completed using simplified slab geometry for several different antenna designs. The first set of simulations used a flattened version of the end-fed, center-grounded antenna installed on the D and E-ports on Alcator C-Mod. This slab antenna, shown in Fig. 5-1, is constructed using antenna straps which are similar electrical length to the actual D and E-port antennas. In addition, the inductive current loops enclose similar RF magnetic flux to that of the D and E-port antennas.

Figure 5-2, shows a poloidal cross-section of a quadratic element mesh described in

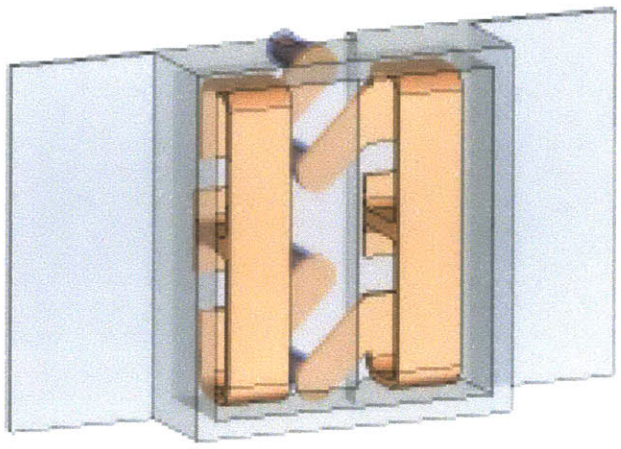

Figure 5-1: Simplified slab model used for FEM simulations. The geometry is based on the end-fed, center-grounded antenna installed on the D and E-ports on Alcator C-Mod described in Ch. 2.

the previous chapter, for both the slab (a) and cylindrical (b) geometries. For these simulations, roughly 2 million degrees of freedom (DoF) are solved. Here element meshing is optimized to provide sufficient spatial resolution in small regions of the model, while keeping the number of unknowns as small as possible.

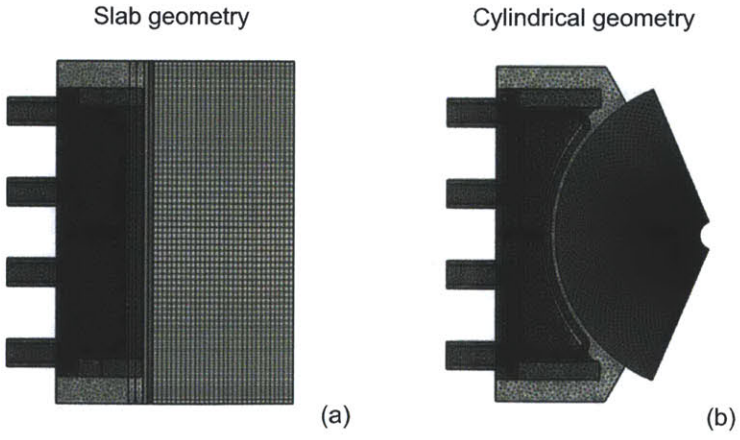

Figure 5-2: Poloidal view of FEM mesh used for slab (a) and cylindrical (b) simulations.

A schematic of the poloidal cross-section of the model domain is shown in Fig. 5-3. Here, the vertical surfaces labeled x = 2.0 cm, x = 2.5 cm and x = 3.0 cm, represent constant magnetic field surfaces where the component of the RF electric

field parallel to the total magnetic field, given by:

$$E_{\parallel} = \frac{\boldsymbol{E}_{RF} \cdot \boldsymbol{B}}{|B|}, \tag{5.1}$$

is evaluated. As seen in the image, the coordinate system defined by Stix [15] is used, where $\boldsymbol{B}/|B| = \hat{z}$, $\hat{x}$ is the radial coordinate, and $\hat{y}$ is the vertical coordinate. One of the motivations for this work is to characterize the effect of magnetic field alignment with the ICRF antenna on $E_{\parallel}$ formation. For this purpose, slab geometry is particularly useful, owing to the simplicity of simulating arbitrary pitch-angles. This is because the necessary rotations involve a single axis and rotation angle. The evaluation *flux surfaces* are planar, by definition. Thus, evaluation of the parallel electric field, given in Eq. 5.1 is straightforward, as is evaluation of the rectification-enhanced sheath potential $\Phi \approx V_{\mathrm{RF}} + 3k_{\mathrm{B}}T$, where the RF potential is given by:

$$V_{RF} = \int \frac{\boldsymbol{E}_{RF} \cdot \boldsymbol{B}}{|B|} dl. \tag{5.2}$$

Here, the line integral is evaluated on magnetic field lines passing close to the front face of the antenna. The limits of integration are finite, but sufficiently far from the antenna structure so that the $E_{\parallel}$ contribution is negligible near the limits of integration.

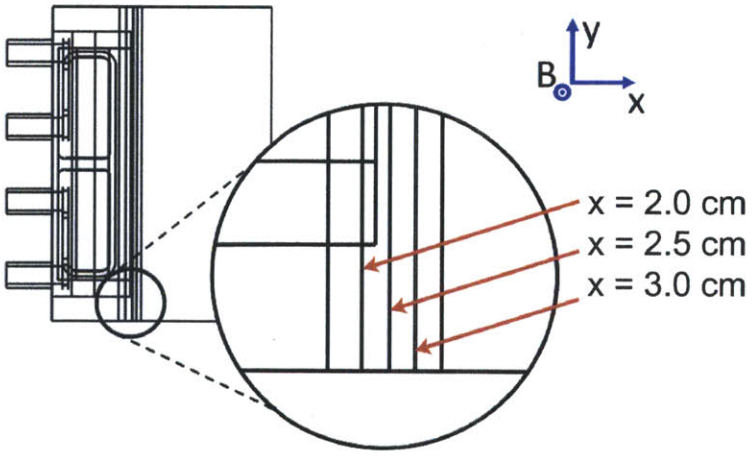

Figure 5-3: Schematic showing slab geometry and surfaces where $E_{\parallel}$ is evaluated.

Contours of the real part of the LHCP component of the electric field $\mathrm{Re}(E^+)$ are plotted in Fig. 5-4, on toroidal and poloidal cross sections. The LHCP component of the electric field is given by:

$$E^+ = E_\mathrm{x} + \mathrm{i}E_\mathrm{y} \tag{5.3}$$

where E_x is the component of the electric field normal to the flux surface, and E_y is the component of the electric field perpendicular to the magnetic field line and tangent to the flux surface at the evaluation point. In Fig. 5-5, contours of the real part of the LHCP component of the electric field $\mathrm{Re}(E^+)$ are shown for two different toroidal phasings. In these plots, the low-field side is on the bottom of the figure, while the high-field side of the tokamak is on top.

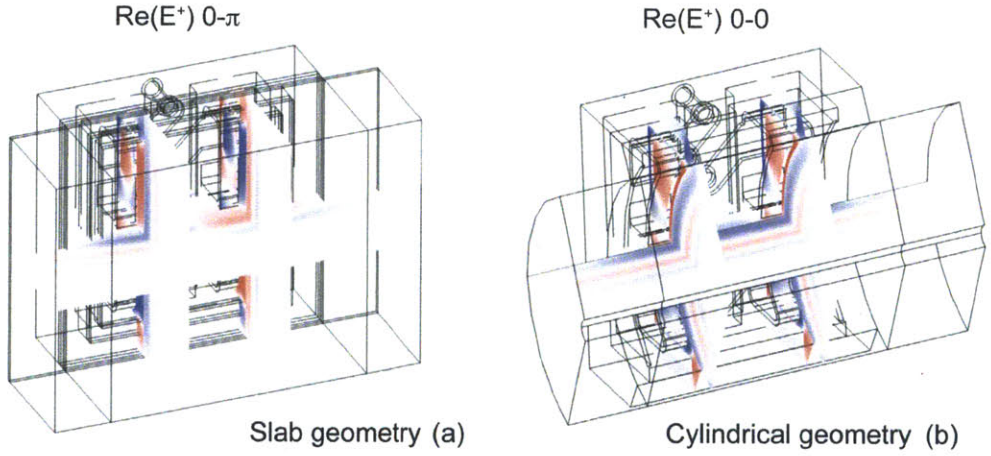

Figure 5-4: LHCP component of the electric field (red is positive, blue is negative): slab geometry using dipole [0, π] phasing (a) and cylindrical geometry showing monopole [0, 0] phasing (b).

In Fig. 5-6, $E_\parallel$ is plotted as a function of position on a plane 2.0 cm in front of the antenna straps, as indicated in Fig. 5-3. In all four plots, the magnetic field direction is in the $\hat{\mathrm{z}}$ direction. In Fig. 5-6(a) and (c), the antenna structure is misaligned with the magnetic field by an angle of 10°. This is contrasted by Fig. 5-6(b) and (d), where the antenna structure is aligned with the magnetic field. These plots provide a very intuitive way to understand how positive and negative contributions to $E_\parallel$ might cancel along a given magnetic field line.

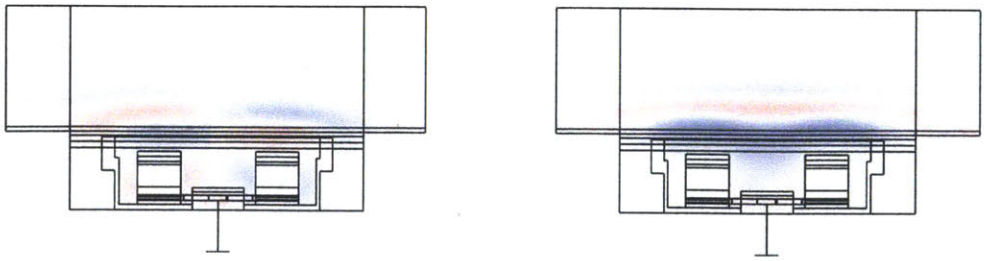

Figure 5-5: LHCP component of the electric field (red is positive, blue is negative), for slab geometry using both dipole [0, π] phasing (a) and monopole [0, 0] phasing (b).

Experimental observations form a data set which is composed entirely of data from antennas not aligned with the total magnetic field. Indeed, almost all currently operating ICRF antennas are positioned horizontally inside the machine, while the magnetic field has a pitch angle at the outer mid-plane of 3° to 20°. For these non-aligned antennas, similar to those represented in Fig. 5-6(a)and (c), observed impurity characteristics are worse for monopole [0, 0] phasing than for dipole $[0, \pi]$ phasing [31, 32, 8]. As described in Ch. 3, these impurity characteristics are related to RF sheath formation and consequently, to $E_{\|}$. Simply looking at Fig. 5-6, it is difficult to tell which toroidal phasing offers better cancellation of $E_{\|}$. However, there are certain regions where the cancellation (or lack of cancellation) is apparent. Compare Fig. 5-6(a) with Fig. 5-6(c). At the midplane, the largest $|E_{\|}|$ is located between the antenna straps and the antenna box. However, the sign of this $E_{\|}$ is opposite on either side of the antenna in (a), but the same on both sides of the antenna in (c). Therefore it is easy to see that $[0, \pi]$ phasing has better cancellation at the mid-plane than does [0, 0] phasing.

Now compare Fig. 5-6(b) with Fig. 5-6(d). At the midplane, $E_{\|} \approx 0$, however $E_{\|}$ at the top and bottom of the antenna structures can be quickly visually inspected. In the $[0, \pi]$ case, shown in Fig. 5-6(b), although $E_{\|}$ is symmetric left to right, the distribution is such that it is more positive at the bottom and more negative at the top. As a result, the $E_{\|}$ cancellation at the top and bottom of the box is worse than in Fig. 5-6(d), where, although the field is asymmetric left to right, the distribution

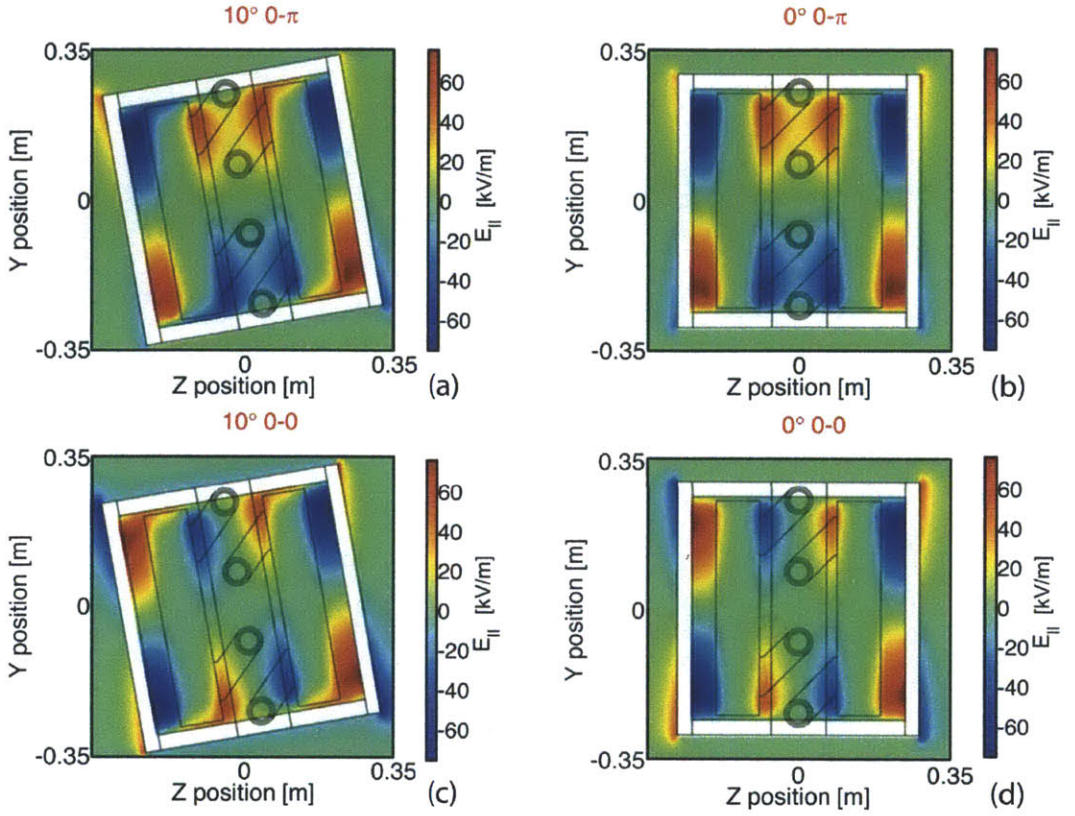

Figure 5-6: Slab geometry plots of $E_{\|}$ in front of the antenna for an antenna misaligned with the magnetic field by 10 deg with [0, π] phasing (a) and monopole [0, 0] phasing (c), and for an antenna aligned with the magnetic field with [0, π] phasing (b) and monopole [0, 0] phasing (d). In these plots, the magnetic field is in the horizontal direction. Surfaces plotted lie 2.0 cm in front of the antenna straps.

of positive and negative values is roughly equal. Therefore, for the field-aligned case, it is easy to see that [0, 0] phasing has better cancellation at the antenna top and bottom than does $[0, \pi]$ phasing. These qualitative observations are confirmed in Fig. 5-7, where the integral of $V_{\mathrm{RF}} = \int \frac{\boldsymbol{E}_{\mathrm{RF}} \cdot \boldsymbol{B}}{|B|} dl$ is plotted for the 10° and 0° cases, as well as a 1° misalignment.

In Fig. 5-7, plots of the absolute value of V_{RF} for two different *radial* locations (x = 2.5 cm and x = 3.0 cm), two toroidal phasings ([0, 0] and [0, π]), and three orientations (10°, 1°, 0°) are shown. In Fig. 5-7(a)–(c) there is a modest reduction in V_{RF} as alignment changes from 10° to 1°, and no apparent change as alignment changes from 1° to 0° for [0, π] phasing. However, in Fig. 5-7(d)–(f) there is a factor

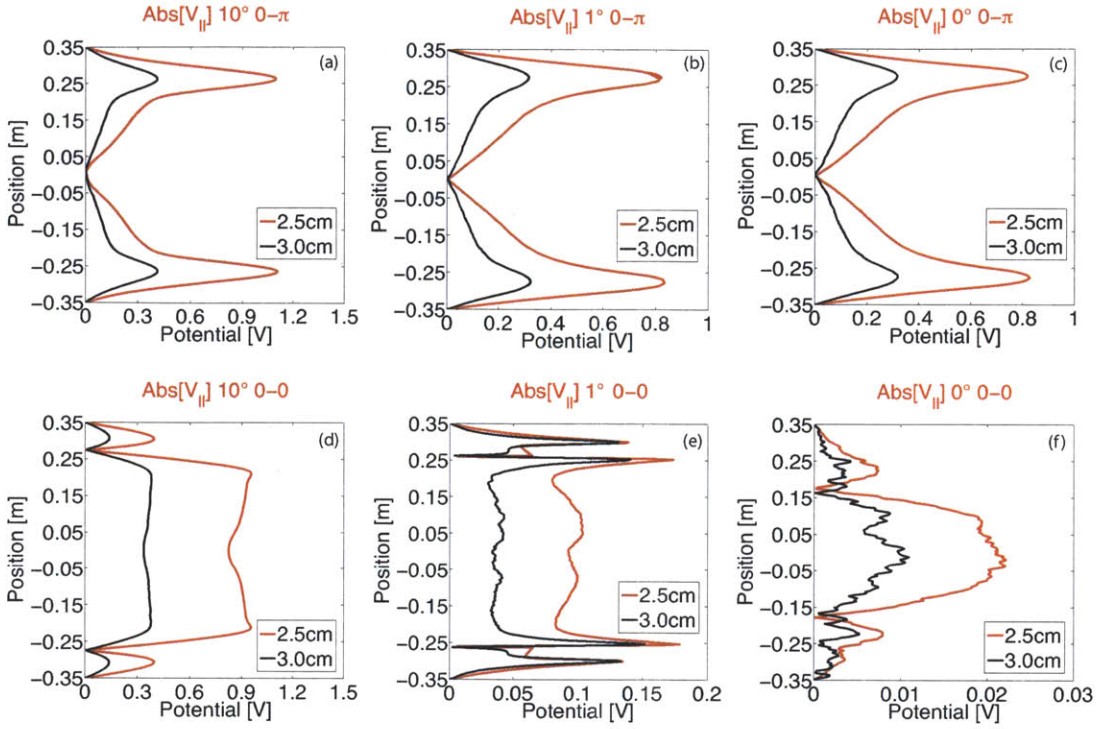

Figure 5-7: Plots of integrated $E_{\|}$ for [0, π] phasing of an antenna misaligned with the magnetic field by 10 deg. (a), 1 deg. (b), 0 deg. (c), and for [0, 0] phasing of an antenna misaligned with the magnetic field by 10 deg. (d), 1 deg. (e), 0 deg. (f). Note the large changes in horizontal scale from one plot to next.

of $\sim$ 50 reduction in V_{RF} as alignment changes from 10° to 0°, and relative to the aligned case 0°, the 1° case shows an increase in V_{RF} of a factor of five for [0, 0] phasing.

The difference in V_{RF} among the three alignments in Fig. 5-7(d)–(f) is significant from the point of view of field-aligned antenna design. This is due to the fact that in a tokamak, the magnetic pitch angle changes with the plasma current. In addition, although the antenna-magnetic field alignment can be made to be quite good, the pitch angle is not constant along the poloidal coordinate. Here we see a small misalignment certainly increases V_{RF}. However, the increase is relatively small compared with a typical ICRF antenna misalignment.

The RF electric fields produced by the antenna are necessarily a function of the current density and its distribution. However, these electric fields are also a function

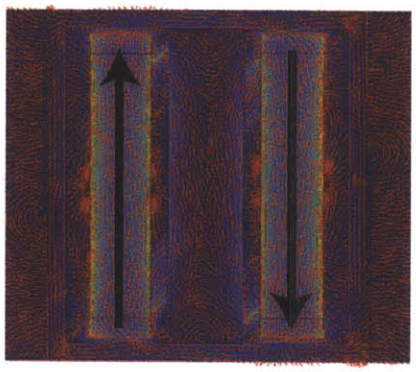

Figure 5-8: Surface current density using copper (skin depth $\delta \sim 7\mu$m) for the entire antenna structure. Small red arrows represent normalized current density, indicating surface current direction only. Background color represents surface current density magnitude; the maximum value, seen at the strap edges, is $\sim$ 2 kA/m for 2 MW input power. The black arrows correspond to the current direction on the front of each strap for [0, π] phasing.

of image currents in the surrounding structure, as seen in 5-8. To investigate the effects of antenna structure geometry on image current characteristics, a series of modifications were made to the slab antenna model described above, using [0, π] phasing.

In Fig. 5-9, the effect of antenna side limiter thickness and position are investigated. Two *radial* slices are used; one lies just outside the limiter edge and one lies just inside the edge, in front of the antenna straps. In Fig. 5-9(a)–(d), only the limiter thickness is varied. Is is apparent that V_{RF} decreases as the limiter thickness increases, supporting the concept of ICRF antennas which are recessed within the first wall. Note for Fig. 5-9(d) the peak observed in all of the other cases (located at $\sim \pm$ 0.3 m) is absent. This is because the primary contribution to this potential is $E_{\|}$ from currents flowing on the outside of the antenna box that aren't present in Fig. 5-9(d). The final case, shown in Fig. 5-9(e), illustrates that moving the limiters farther from the antenna straps decreases V_{RF}. This reduction in V_{RF} is a direct result of smaller image currents in the box due to the larger distance from the antenna straps.

In Fig. 5-10, the effect of antenna box wall modification and the addition of an upper and lower box lip is investigated. Here, the RF potential is evaluated 0.5 cm

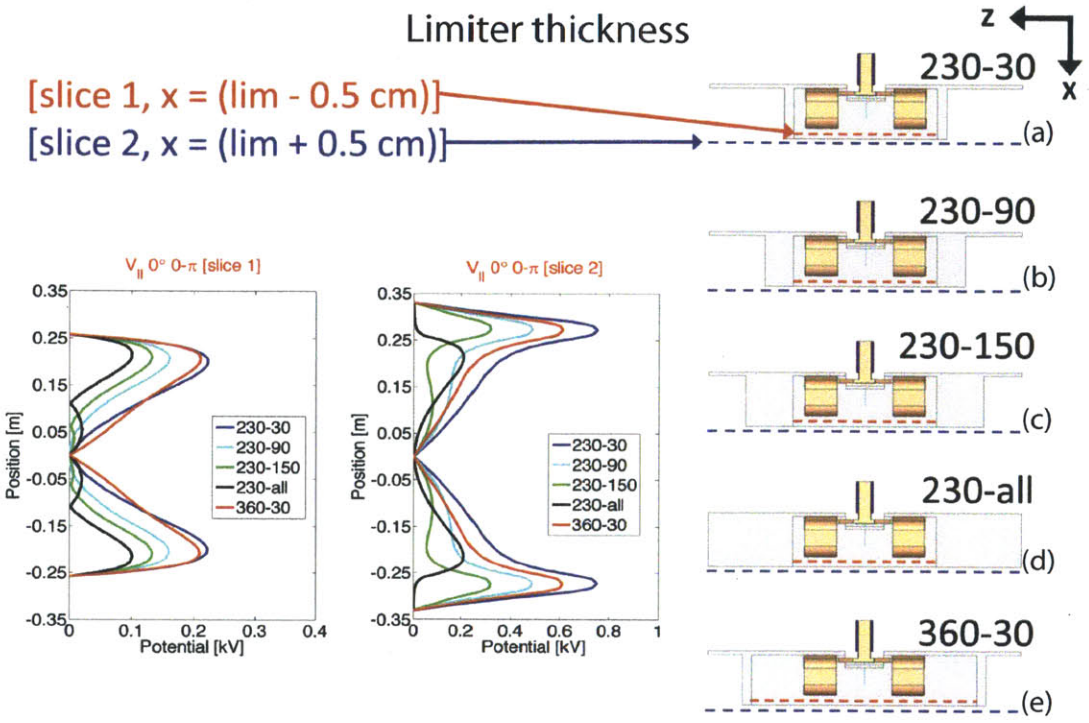

Figure 5-9: Antenna slab limiter topology study quantifying the effect of limiter thickness on V_{RF} at two *radial* positions (slice 1 is located 0.5 cm radially inward of the antenna limiter edge and slice 2 is located 0.5 cm radially outward of the antenna limiter edge). The nomenclature used in (a)–(e) is as follows: the first number represents the $\hat{z}$ distance in mm, from the inner edge of the limiter to the center of the antenna box; the second number represents the toroidal extent of the limiter, in mm.

in front of the antenna limiters. In Fig. 5-10(b)–(d), the effect of adding an upper and lower lip to the antenna box is shown to broaden the peak voltage distribution in the $\hat{y}$ direction. In Fig. 5-10(c)–(e), the effect of removing material from the sides of the antenna box is shown to significantly increase the peak voltage. In contrast, Fig. 5-10(f) shows that removing the top and bottom of the antenna box greatly reduces the RF potential.

In Fig. 5-11, the effect of antenna box slotting is investigated. As in Fig. 5-10, the RF potential is evaluated 0.5 cm in front of the antenna limiters. Here, the baseline case is shown in (b). In Fig. 5-11(a), (c), (d), and (e) different slotting is applied to the walls of the antenna box. Slots 5 cm deep and 1 cm wide are added to the

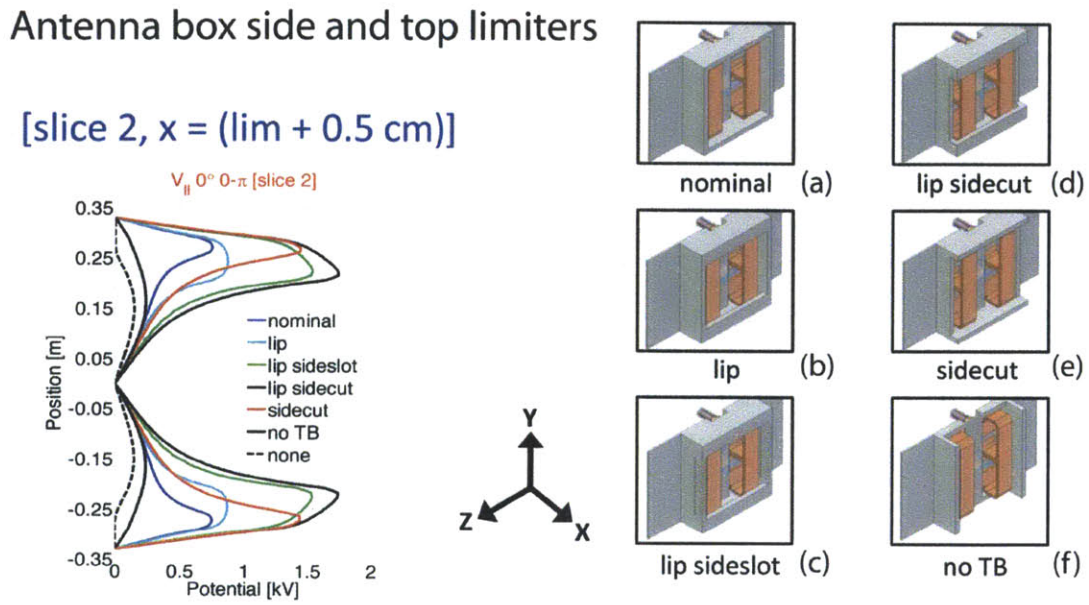

Figure 5-10: Antenna slab limiter topology study quantifying the effect of antenna box modification on V_{RF}, evaluated 0.5 cm radially outward of the antenna limiter edge. Six cases are labeled as follows: the baseline is shown in (a), a lip is added in (b), sidewalls are slotted in (c) and completely removed in (d), a lip is added to the no sidewall case in (e), and the top and bottom are removed in (f).

sidewalls in (a), the top and bottom in (e), and all four walls in (d). In Fig. 5-11(c) the top and bottom are slotted with 1 cm deep, 1 cm wide slots. Finally, in Fig. 5-11(f) the sidewalls are removed completely.

Here, slotting the antenna sidewalls clearly increases V_{RF}, while slotting the top and bottom provides a substantial decrease in V_{RF}. This is an interesting result; although the side limiters of ICRF antennas are typically slotted to allow better RF flux coupling to the plasma, this slotting actually makes V_{RF} larger. Conversely, to maximize $E_{\|}$ cancellation, the top and bottom of the antenna structure should be slotted. Unfortunately, this would introduce the unwanted effect of having small, high-voltage gaps where $\mathbf{E} \parallel \mathbf{B}$, within the conducting antenna structure. In areas on the C-Mod ICRF antennas where $\mathbf{E} \parallel \mathbf{B}$ arcing is observed at fields of $\sim 1.5\mathrm{MVm}^{-1}$, compared to $\sim 3.5\mathrm{MVm}^{-1}$ in areas where $\mathbf{E} \perp \mathbf{B}$. [40]

Following 3-D slab geometry simulations, 3-D cylindrical geometry was investi-

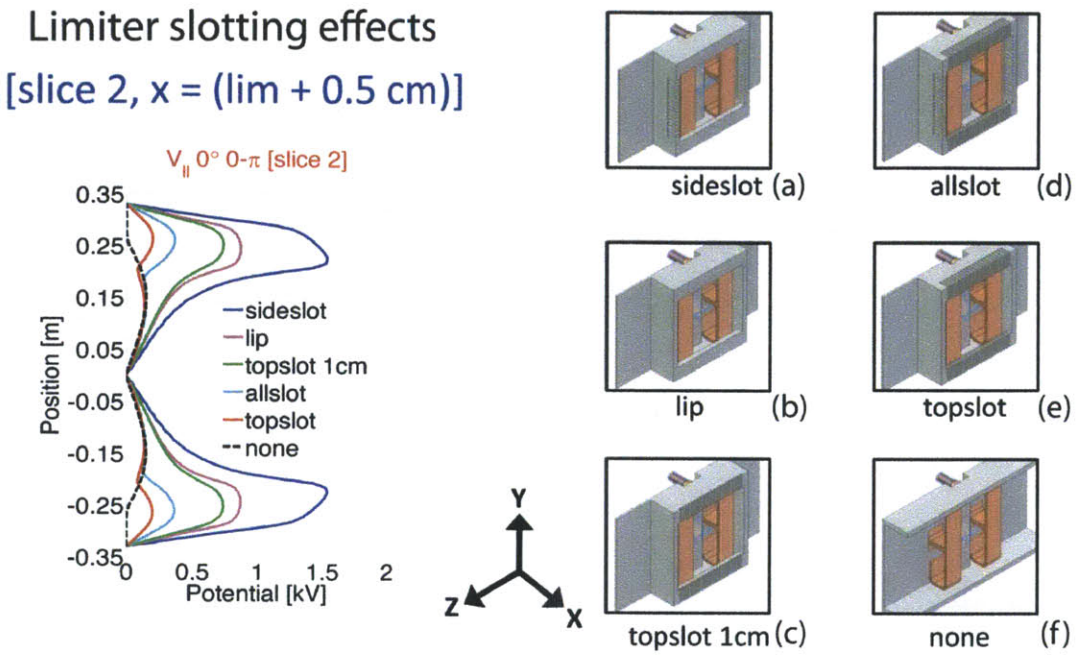

Figure 5-11: Antenna slab limiter topology study quantifying the effect of antenna box slotting on V_{RF}, evaluated 0.5 cm radially outward of the antenna limiter edge. Six cases are labeled as follows: the baseline is shown in (b), the sidewalls are slotted in (a), the top and bottom are slotted in (c)–(e), and all of the box walls are slotted in (d).

gated. In Fig. 5-12, the [0, π] and [0, 0], 0° and 10° cases from Fig. 5-7(a), (c), (d), and (e) are compared directly with 0°, [0, 0] and [0, π] cases for a cylindrical antenna-plasma model. Here, we see the reduction in integrated $E_{\|}$ is similar for both the slab and cylindrical cases. This similarity extends to both the shape of V_{RF}, and the magnitude. Subsequently, toroidal models were implemented to characterize wave propagation, antenna coupling, and $E_{\|}$ in Alcator C-Mod geometry. In slab geometry, $E_{\|}$ is exactly perpendicular to the current strap direction. However, for toroidal geometry, $E_{\|}$ is a complex function of all spatial components of the electric field produced from currents in all of the individual straps. Here, the question of $E_{\|}$ cancellation through symmetry becomes much more complicated.

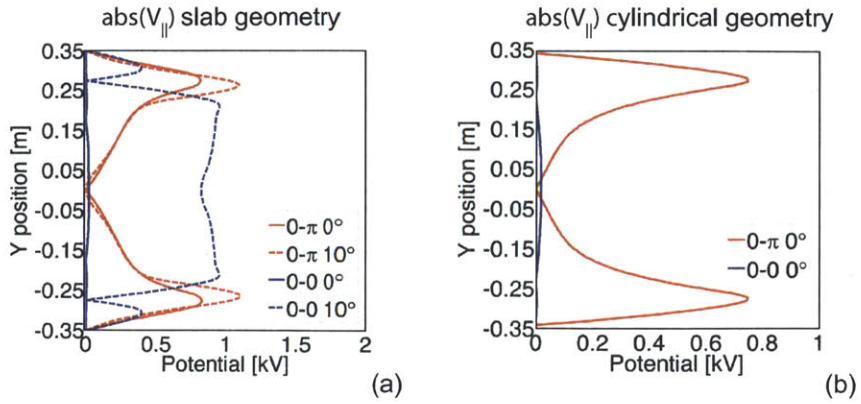

Figure 5-12: Comparison of integrated $E_{||}$ for slab and cylindrical models for both [0, 0] and [0, π] phasing.

5.2 Toroidal geometry

For the first time, an ICRF-cold-plasma model has been implemented in entirely spatial domain 3-D toroidal geometry, using FEM. Toroidal models were implemented using both the cold plasma dielectric tensor and isotropic dielectric tensor described in the previous chapter. For these simulations data from an Alcator C-Mod discharge with plasma current $I_{\mathrm{p}} = 1$ MA, $B_{\mathrm{T}} = 5.4$ T, and appropriate shaping to yield a magnetic pitch angle of 10° at the outer midplane. As shown in Fig. 5-13, the alignment of the antenna structure and the magnetic field at the edge (blue streamlines) is quite good.

Finite element method codes are fundamentally well suited to model complicated 3D geometry, as described in Ch. 4. However, in practice, incorporating complex 3D structures into simulation models and properly meshing them is non-trivial. For these simulations, much attention was given to incorporating fine details of the model geometry which might impact the relevant physics of the problem. At the same time, unnecessary details were omitted whenever possible for numerical considerations. Meshing of structures (where finite element nodes are mapped onto the spatial domain of the model), was done programmatically to ensure an optimum mesh distribution. In this way, fine structures purposely included in the model were not assigned too many mesh nodes. Likewise, large areas of the model were assigned a sufficient

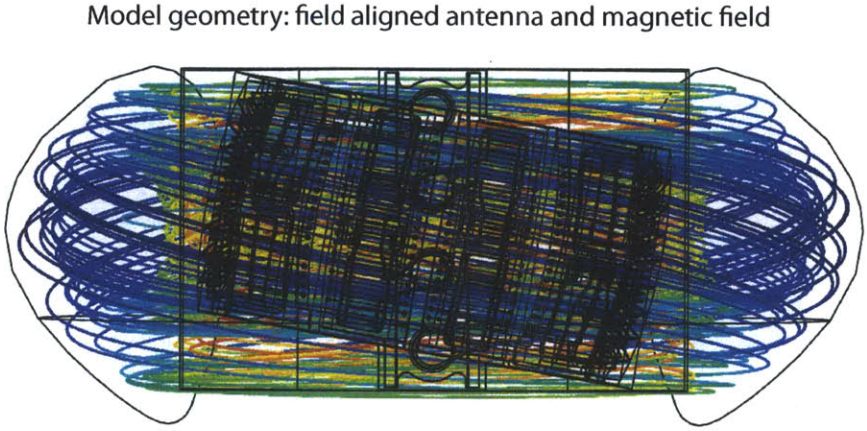

Figure 5-13: View of field-aligned antenna superimposed on magnetic field.

mesh density to assure proper convergence of the solution. Optimization studies were implemented early in the development process to ensure sufficient nodal resolution and efficient solution convergence.

A rectangular prism section of Alcator C-Mod surrounding the antenna, shown in Fig. 5-14, was chosen for the simulation domain. Both top and side views are shown along with relevant boundary conditions. An EM wave scattering boundary condition was implemented at the front and sides of the model domain to prevent waves not absorbed within the plasma from reflecting. The plasma region is shown in violet, with surrounding scrape-off layer. All calculation domains outside the plasma are composed of either vacuum or filled with conductor. The mid-plane SOL density profile used for these simulations is a modified hyperbolic tangent fit to measured plasma density. In Fig. 5-15, four simulation subdomains are shown: Bulk plasma, SOL, vacuum region, and antenna. The density used for the SOL has been artificially truncated at $R_0 = 90$ cm to establish a vacuum region directly in front of the antenna. A CAD drawing of the Alcator C-Mod field-aligned ICRF antenna is shown in Fig. 5-16(a). The antenna is rotated 10 degrees from horizontal to align with the total magnetic field. In Fig. 5-16(b), the FEM model geometry is shown for the field-aligned antenna and evaluation flux surface 0.5 cm in front of antenna private side limiters.

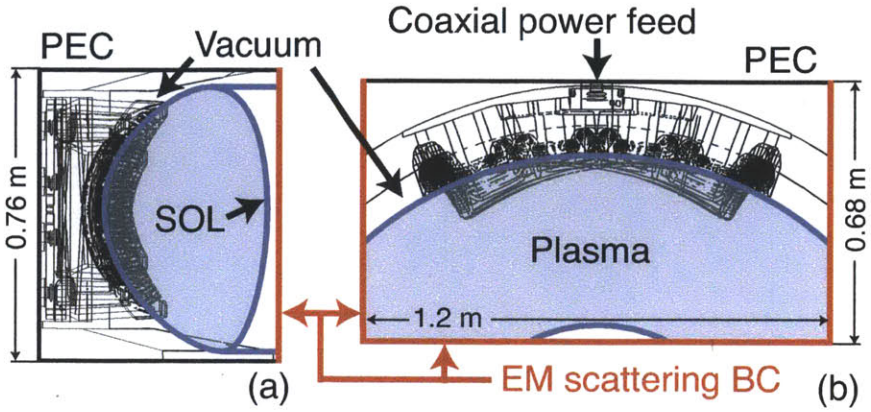

Figure 5-14: The simulation domain is shown for the field-aligned antenna in side (a), and top (b) views. An EM wave scattering boundary condition is implemented at the front and sides of the simulation domain to prevent reflection of any waves not damped within the plasma. A perfect electric conductor (PEC) condition was used at the remaining simulation boundaries. Note that the plasma does not intersect the antenna; this effect is merely due to the mid-plane projection of the plasma on the model shown.

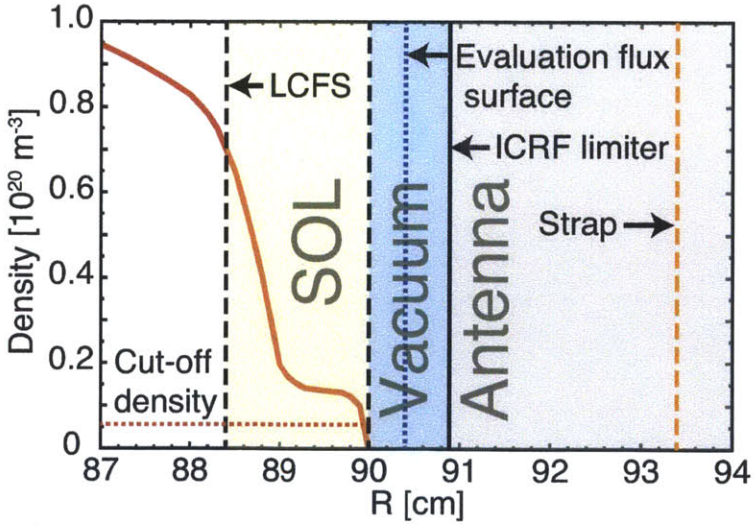

Figure 5-15: Mid-plane density profile and radial geometry map of simulation. The simulation domain contains four primary regions: Bulk plasma, SOL, vacuum, and antenna. The evaluation flux surface is indicated in blue at $R = 90.5$ cm.

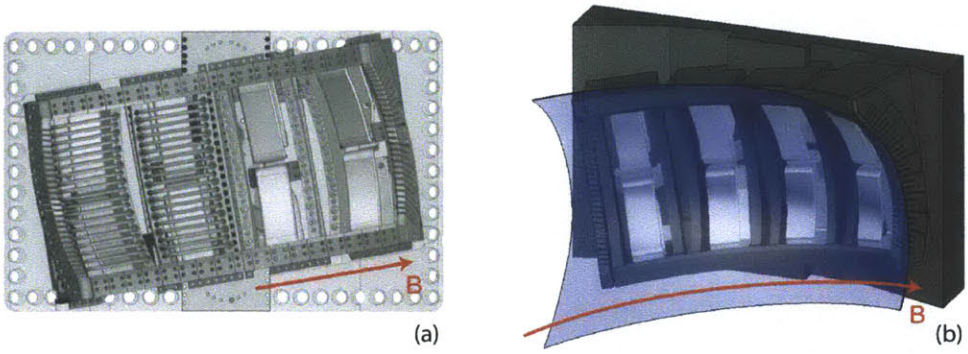

Figure 5-16: The new Alcator C-Mod field-aligned ICRF antenna is rotated 10 degrees from horizontal to align with the total magnetic field (a). FEM model geometry is shown for the field-aligned antenna and evaluation flux surface 0.5 cm in front of antenna private side limiters (b). Faraday rods are removed from the image for clarity.

Figure 5-17 shows the CAD model used for simulations and two planar surfaces where E^+ is evaluated. Figure 5-17(a) shows a tilted cross section bisecting one of the antenna straps where E^+ is evaluated in 5-18. Figure 5-17(b) shows a cross section through the antenna midplane where E^+ is evaluated in Fig. 5-20.

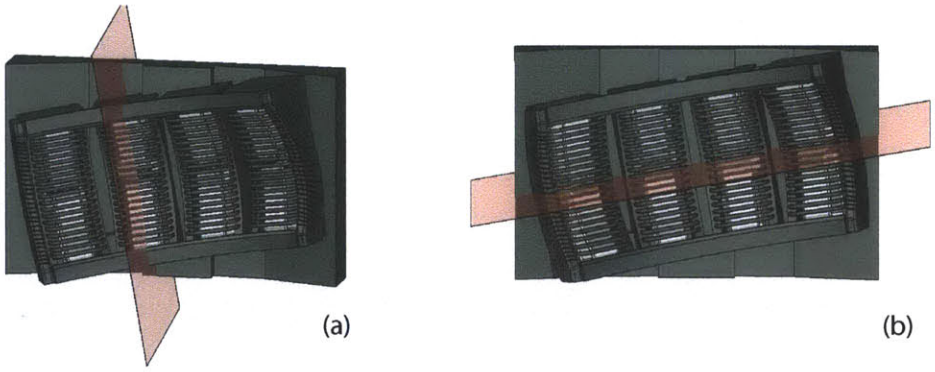

Figure 5-17: Model antenna geometry showing E^+ evaluation surfaces for poloidal and toroidal cross section results.

In Ch. 2, the ion cyclotron resonance layer was defined as the surface where the launched frequency equals the ion cyclotron frequency ($\omega = \omega_{ci}$), and was shown to depend primarily on the magnetic field, particle species and launched frequency. For a set launched frequency, as the magnetic field is increased, the 1/R dependence causes

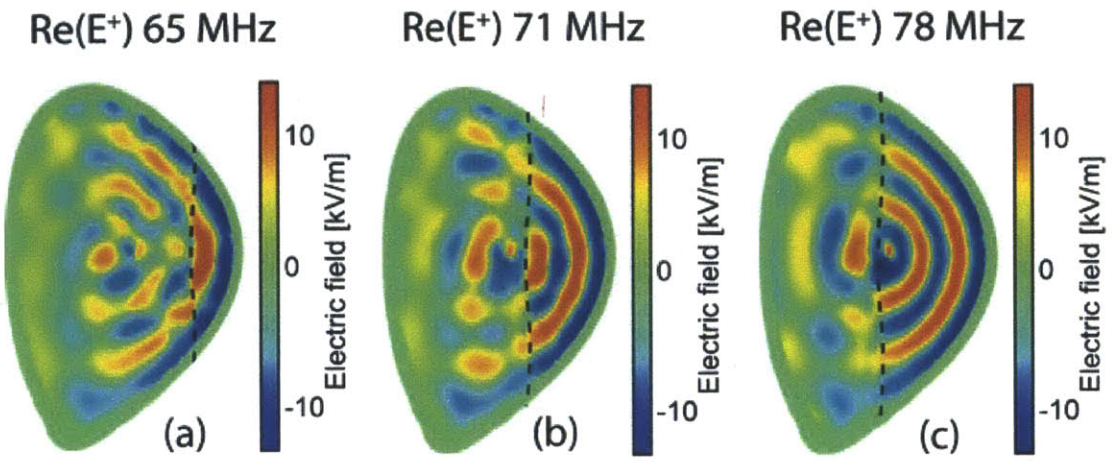

Figure 5-18: Plots of the real part of the LHCP component of the electric field $\mathrm{Re}(E^+)$ for launched ICRF frequencies of 65 MHz (a), 71 MHz (b) and 78 MHz (c) in C-Mod simulation with $B_\mathrm{T} = 5.4$ T. Minority resonance layer is shown for 5% hydrogen minority in deuterium.

the resonance layer to move outward in major radius. Likewise, for a fixed magnetic field, as the launch frequency is decreased the resonance layer moves outward in major radius. This effect is simulated in Fig. 5-18, where a hydrogen minority resonance is created in a deuterium plasma. In Fig. 5-18(a)–(c), the launched frequency is shifted from 65 MHz in (a), to 71 MHz in (b) and finally 78 MHz in (c). Here, the coherent waves artificially damp near the minority ion cyclotron resonance layer, which moves radially inward as the launched frequency is increased.

Figure 5-19 shows poloidal cross sections of a part of the model domain. In Fig. 5-19 (a), absorbed power, plotted as a function of major radius, is given by:

$$P_\mathrm{abs} = \frac{1}{2}\mathrm{Re}\left[\boldsymbol{E}^* \cdot \left(-i\varepsilon_0\omega\left(\overleftrightarrow{\epsilon} - \overleftrightarrow{\boldsymbol{I}}\right)\right) \cdot \boldsymbol{E}\right] \tag{5.4}$$

where $\boldsymbol{E}^*$ is the complex conjugate of the electric field, and $\overleftrightarrow{\epsilon}$ is defined in Eq. (4.9). Figure 5-19(b) shows a contour plot of the artificial minority ion absorbed power. The absorption is strongest in the vicinity of the minority cyclotron resonance layer, where substantial damping occurs as a result of the artificial collisionality included through ν [62]. Contours of the real part of the left-hand circularly polarized (LHCP) component of the electric field $\mathrm{Re}(E^+)$ are plotted in Fig. 5-19(c). Note that coherent

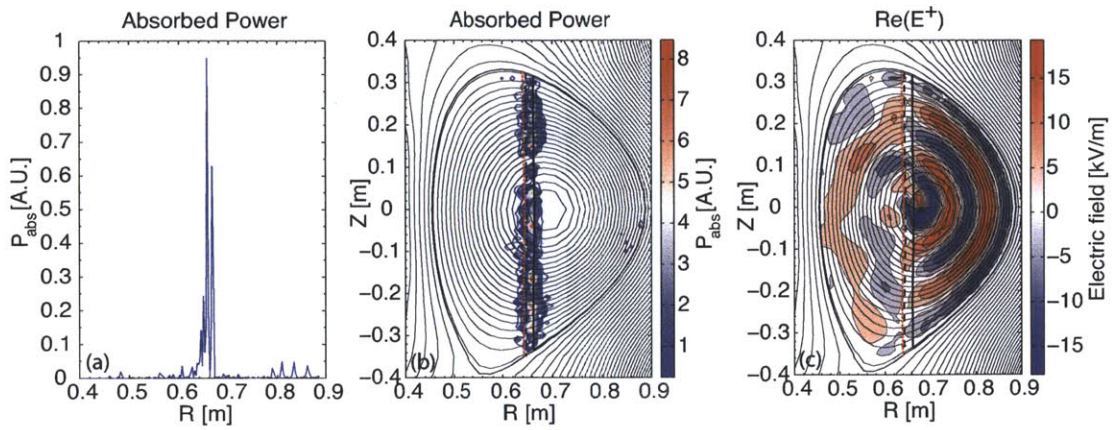

Figure 5-19: Simulated wave propagation and absorption for two ion minority D(H) cold plasma: Power absorbed as a function of major radius (a), contour plots of absorbed power on a poloidal plasma cross section (b), and the real part of the LHCP component of the electric field Re(E^+) (c).

waves propagate from the antenna at $R_0 = 0.91$ m toward the minority cyclotron resonance layer, where they are artificially damped.

Contours of the real part of the LHCP component of the electric field Re(E^+) are again plotted in Fig. 5-20, here on a midplane toroidal cross section shown in 5-17. For toroidal geometry, the LHCP component of the electric field is given by:

$$E^+ = E_\mathrm{N} + \mathrm{i}E_\perp \tag{5.5}$$

where E_N is the component of the electric field normal to the flux surface, and $E_\perp$ is the component of the electric field perpendicular to the magnetic field line and tangent to the flux surface at the evaluation point. In these plots, the low-field side (where the antenna is located) is on the bottom of the figure, while the high-field side of the tokamak is on top. In Fig. 5-20(a)–(c), typical toroidal heating phasings are shown: $[0, \pi, 0, \pi]$, $[0, \pi, \pi, 0]$ and $[0, 0, \pi, \pi]$. On Alcator C-Mod, only the first two are generally used for heating. Figure 5-20(d) shows monopole phasing [0, 0, 0, 0], where the current in all of the antenna straps is in-phase. Figure 5-20(e) shows a variation from monopole phasing, where a phase shift of $\pi/6$ is added to every other strap. Finally, Fig. 5-20(f), shows typical co-current drive (CD) phasing $[0, \pi/2, \pi, 3\pi/2]$

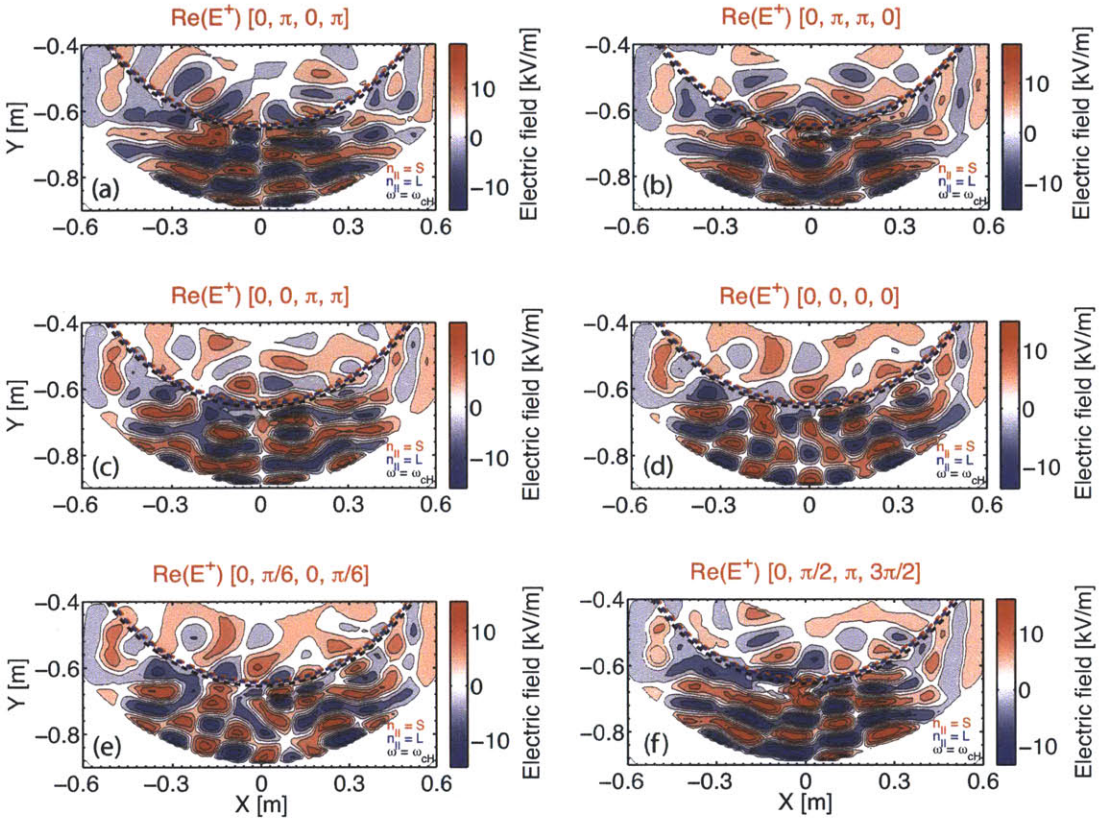

Figure 5-20: Contours of the real part of the LHCP component of the electric field $\mathrm{Re}(E^+)$ evaluated on a toroidal cross section of the plasma at the midplane. Toroidal strap phasings shown are: $[0, \pi, 0, \pi]$ (a), $[0, \pi, \pi, 0]$ (b), $[0, 0, \pi, \pi]$ (c), $[0, 0, 0, 0]$ (d), $[0, \pi/6, 0, \pi/6]$ (e), and $[0, \pi/2, \pi, 3\pi/2]$ (f). The fast-wave resonance $n_\parallel = S$, is shown by the dotted line (red). The fast-wave cutoff $n_\parallel = L$, is shown by the dashed line (blue), and the the minority cyclotron resonance $\omega = \omega_{cH}$, is shown by the solid line (black)

used on C-Mod. Similar to 5-19(c), the coherent waves artificially damp near the minority cyclotron resonance. The fast-wave resonance $n_\parallel^2 = S$, is shown by the dotted line (red). The fast-wave cutoff $n_\parallel^2 = L$, is shown by the dashed line (blue), and the the minority cyclotron resonance $\omega = \omega_{cH}$, is shown by the solid line (black).

The launched power spectrum of an ICRF antenna is important for several reasons. First, heating or current drive can be produced depending on whether a symmetric or asymmetric spectrum of waves is launched. Second, as mentioned previously, antenna-plasma coupling increases with decreasing $k_\parallel$, but core absorption decreases

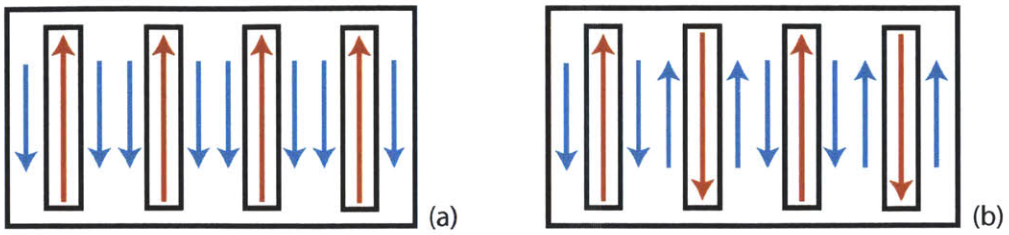

Figure 5-21: Schematic of primary poloidal currents for a 4-strap ICRF antenna. The red arrows indicate current direction on the straps, while the blue arrows indicate return image currents on the septa. Monopole phasing $[0, 0, 0, 0]$ is shown in (a), and dipole phasing $[0, \pi, 0, \pi]$ is shown in (b). Note that in the dipole case, the image currents between the straps are opposite and thus cancel each other fairly well. However, in the monopole case the image currents add together, forming a structure that behaves like a 7-strap antenna with $0 - \pi$ phasing between straps.

with increasing $k_{\|}$. As a result, there is a trade-off between low and high parallel wavenumber spectra. In addition, for conventional ICRF antennas, low $k_{\|}$ phasings tend to produce more impurities, hot-spots and arcing than higher $k_{\|}$ phasings.

It has been indicated previously that image currents on the septa between current straps can have a profound effect on the launched power spectrum of the antenna [63]. This is especially true for monopole phasings, where the image currents on septa are opposite to the strap currents. In Fig. 5-21, this effect is shown for a pair of 4-strap antennas. The red arrows in the figure indicate current direction on the straps, while the blue arrows indicate return image currents on the septa. Monopole phasing $[0, 0, 0, 0]$ is shown in 5-21(a), and dipole phasing $[0, \pi, 0, \pi]$ is shown in 5-21(b). Note that in the dipole case, the image currents between the straps are opposite and thus cancel each other fairly well. However, in the monopole case the image currents add together, forming a structure that behaves like a 7-strap antenna with π phasing between straps. This is seen quite clearly in the toroidal cross section plots of E^+ in Fig. 5-20(d) and (e). Comparing 5-20(a) and (d) with Fig. 5-21(a) and (b) we see that the wave periodicity at the plasma edge in Fig. 5-20 matches the current distribution shown in Fig. 5-21.

The discrepancy between analytical power spectra calculations and actual launched spectra is particularly significant for low parallel wavenumber phasings. This has im-

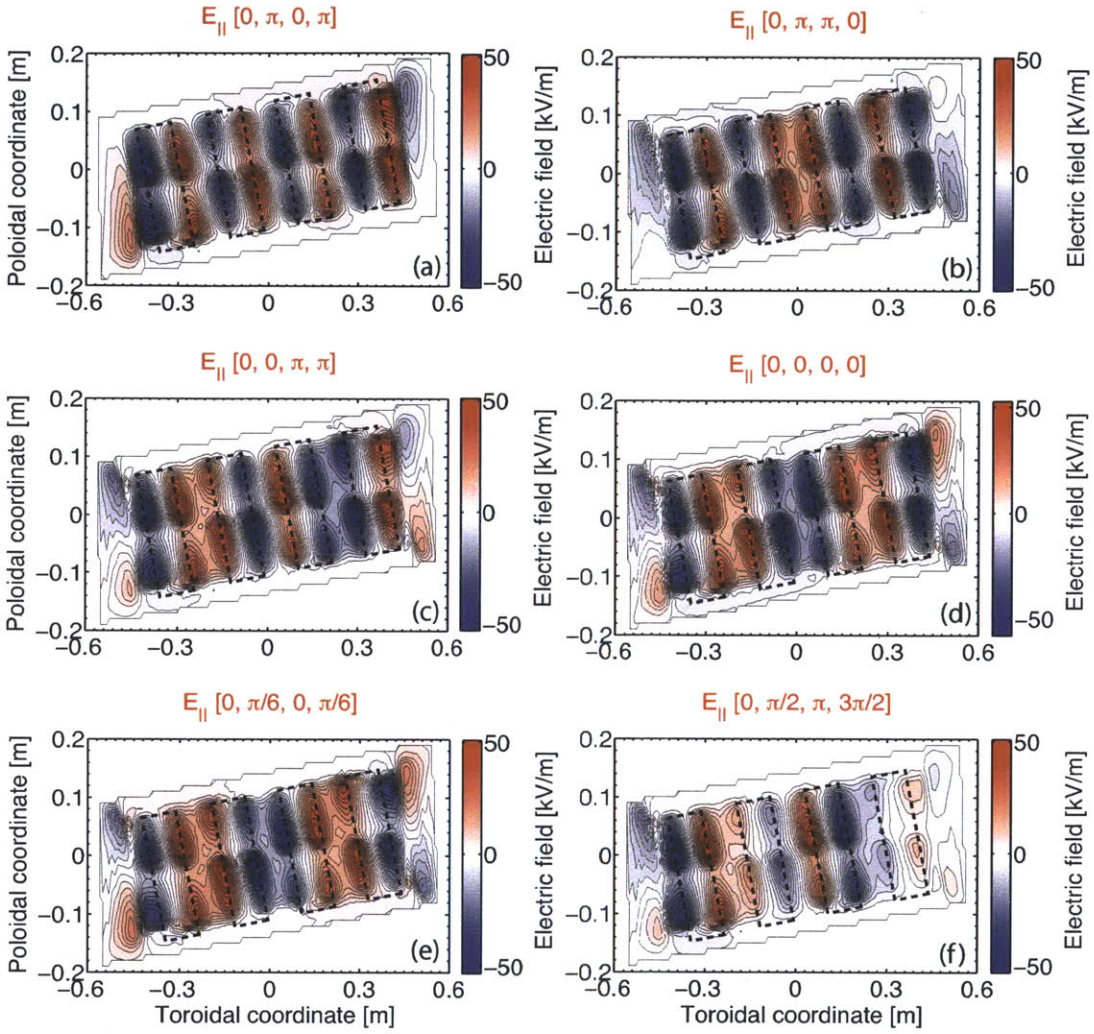

Figure 5-22: Parallel electric field $E_\parallel$, plotted on projections of a flux surface 0.5 cm radially inward of the poloidal antenna limiters. Toroidal strap phasings shown are: $[0, \pi, 0, \pi]$ (a), $[0, \pi, \pi, 0]$ (b), $[0, 0, \pi, \pi]$ (c), $[0, 0, 0, 0]$ (d), $[0, \pi/6, 0, \pi/6]$ (e), and $[0, \pi/2, \pi, 3\pi/2]$ (f).

portant implications for codes which do not treat the plasma response to all of the 3D antenna structure currents self-consistently. Three dimensional models such as the one used here can provide a self-consistent plasma-SOL-antenna solution. As a result, the actual launched spectrum should have better agreement with the calculated spectrum.

In Fig. 5-22, $E_\parallel$ is plotted on a projection of a flux surface positioned 0.5 cm radially inward of the poloidal antenna limiters, for the same toroidal strap phasings

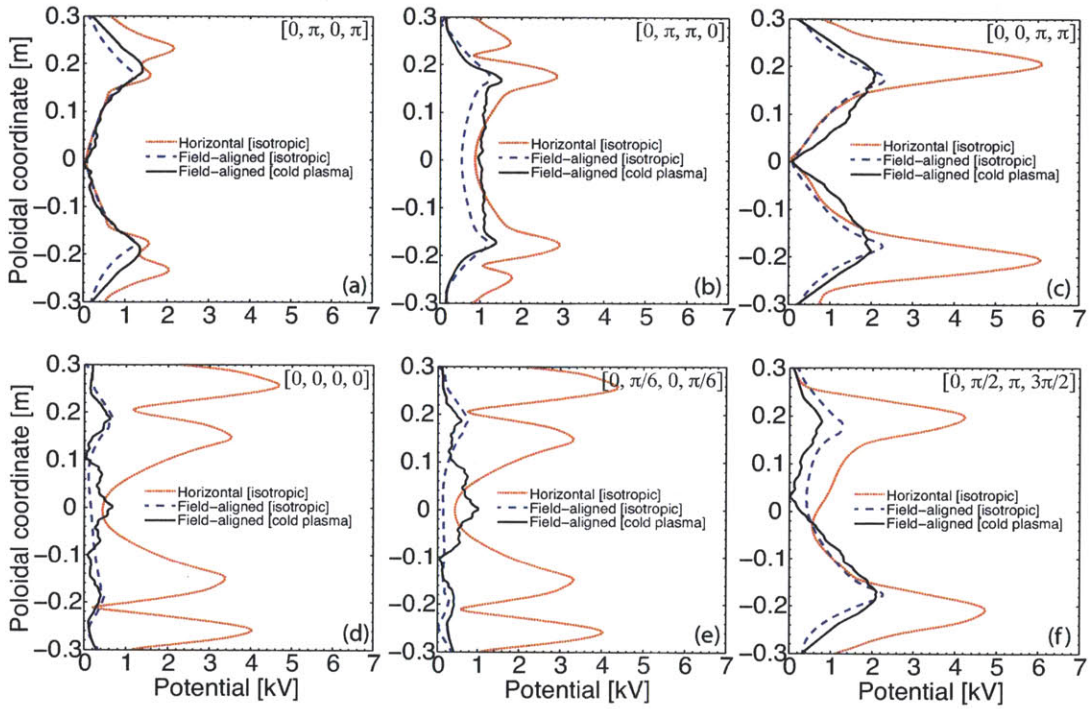

Figure 5-23: RF potential, evaluated 0.5 cm radially inward of antenna limiters. Toroidal strap phasings shown are: $[0, \pi, 0, \pi]$ (a), $[0, \pi, \pi, 0]$ (b), $[0, 0, \pi, \pi]$ (c), $[0, 0, 0, 0]$ (d), $[0, \pi/6, 0, \pi/6]$ (e), and $[0, \pi/2, \pi, 3\pi/2]$ (f). The dotted line (red) represents the previous horizontal antenna, and the dashed line (blue) represents the field-aligned antenna, each loaded with an isotropic dielectric. The solid line (black) represents the field-aligned antenna loaded with the cold plasma model described in section 4.3.

shown in Fig. 5-20. Figure 5-22(a)–(c) are typical ICRF 4-strap heating phasings, Fig. 5-22(d)–(e) are the low $k_{\|}$ heating phasings, and Fig. 5-22(f) is for current drive. The outlines of the antenna straps have been superimposed on the figure for clarity. The positive and negative peaks of $E_{\|}$ occur at the edges of the antenna strap where the current density is highest. These positive and negative peaks correspond to electric fields in opposite directions on a given magnetic field line. For a magnetic field line passing through this region, $E_{\|}$ cancellation will be largest if the positive and negative values integrate to zero. Note, in Fig. 5-22 that the positive and negative contributions of $E_{\|}$ are particularly imbalanced at the antenna side limiters, shown at the left and right edge of each figure.

To quantify the rectification enhanced sheath potential, we use Eq. 5.2, repeated

here for convenience: $V_{\mathrm{RF}} = \int \frac{\boldsymbol{E}_{RF} \cdot \boldsymbol{B}}{|B|} dl$. Here, the line integral is evaluated on magnetic field lines passing close to the front face of the antenna. The limits of integration are finite, but sufficiently far from the antenna structure so that the $E_{\|}$ contribution is negligible near the limits of integration. Figure 5-23 shows the absolute value of Eq. (5.2), evaluated on magnetic field lines passing 0.5 cm radially inward of the antenna limiters, as a function of the poloidal coordinate at the antenna. Six different toroidal phasings are considered. Figures 5-23(a)–(c) display typical heating phasings: $[0, \pi, 0, \pi]$, $[0, \pi, \pi, 0]$, and $[0, 0, \pi, \pi]$. Figure 5-23(d) shows shows monopole heating phasing $[0, 0, 0, 0]$. One caveat for the monopole case is that small specific core absorption rates occur at the monopole $k_{\|}$ spectral peak of 0 m^{-1} [24]. This may be avoided by using pseudo-monopole phasing, or a variant with a finite $k_{\|}$ spectral peak. Figure 5-23(e) shows a variant of monopole phasing, pseudo-monopole phasing $[0, \pi/6, 0, \pi/6]$, in which a toroidal phase shift of $\pi/6$ is added to every other strap relative to the monopole case to establish a finite $k_{\|}$ at the spectral peak. Finally, Fig. 5-23(f) shows the typical co-current current drive phasing used on Alcator C-Mod $[0, \pi/2, \pi, 3\pi/2]$. For comparison, in each figure the dotted line (red) represents the previous horizontal antenna, and the dashed line (blue) represents the field-aligned antenna, each loaded with an isotropic dielectric. The solid line (black) represents the field-aligned antenna loaded with the cold plasma model described in Ch. 4.

In each case shown in Fig. 5-23, the integrated $E_{\|}$ is reduced relative to the previous non-aligned antenna. A modest reduction is apparent in both the $[0, \pi, 0, \pi]$ and $[0, \pi, \pi, 0]$ cases. However, the reduction in the RF potential for the other cases ($[0, 0, \pi, \pi]$, $[0, 0, 0, 0]$, $[0, \pi/6, 0, \pi/6]$, and $[0, \pi/2, \pi, 3\pi/2]$), is more substantial; the reduction in V_{RF} for these phasings is a factor of 2–3. This is especially significant for the low-$k_{\|}$ monopole and pseudo-monopole cases, which have the highest total V_{RF} for the non-aligned antenna. For the field-aligned antenna, monopole and pseudo-monopole phasings have the lowest total V_{RF}.

Extensive simulation of field-aligned and conventional antennas has been accomplished using, for the first time, an entirely spatial domain, 3-D, toroidal ICRF-cold-plasma model. For each toroidal phasing investigated, including conventional

symmetric spectra heating phasings, current drive phasings and monopole phasings, integrated $E_{||}$ was reduced for the field-aligned antenna structure. Therefore based on this modeling of the RF launching structure and cold plasma response, we expect significant reductions in impurity contamination caused by the sheath rectification of $E_{||}$ during operation of the field-aligned antenna.

Chapter 6

Manufacturing and Installation

6.1 Antenna parts

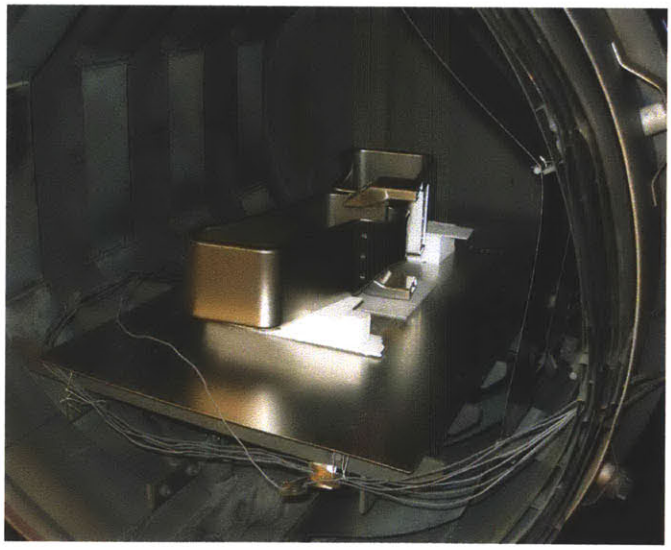

Figure 6-1: Inconel current strap ready to be baked in oven.

The field-aligned antenna parts were manufactured both within the Plasma Science and Fusion Center (PSFC) machine shop at MIT and at commercial vendors. Much of the work which could be done at MIT was machined in-house. The most complicated pieces were the four folded antenna straps. These pieces are complicated geometric shapes whose front surface conforms to a virtual plasma flux surface, while being rotated 10° from horizontal. In addition, the straps were made of 625 Inconel

nickel superalloy to withstand the large disruption forces present inside the tokamak. Conventional milling techniques could not be used to machine these parts from a single piece of metal as desired. Therefore, 6-axis wire electrical discharge machining (EDM) was used to machine all four current straps at the PSFC. One of the four Inconel straps is shown in Fig. 6-1 inside an oven used to bake large parts. The straps are thoroughly cleaned, baked and sent to a commercial vendor to be electroplated with copper.

Some of the field-aligned antenna parts, such as the large stainless steel back plates were sent outside to be machined. In addition, the Faraday screen (FS) rods were machined, bent, cut to length and coated by commercial vendors. The rods, shown in Fig. 6-7 (e), were machined from solid molybdenum and coated with titanium boron nitride (TiBN). All of the antenna protection tiles were machined at PSFC from TZM molybdenum. Both sets of tiles, shown in Fig. 6-2, were attached to the antenna box structure using silver plated vented machine screws. Visible in Fig. 6-2 are the side limiter slots which enhance RF magnetic flux transmission through the sides of the antenna box structure.

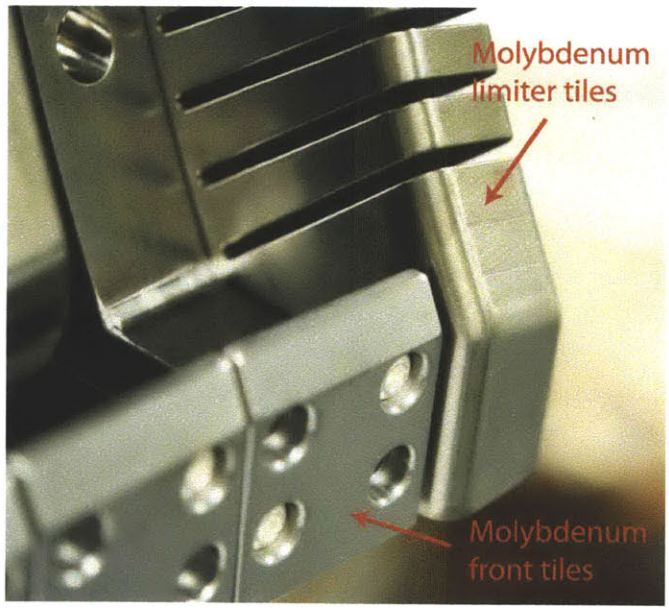

Figure 6-2: The protection tiles for the field-aligned antenna, like previous C-Mod ICRF antennas, are made from TZM molybdenum and machined at the PSFC.

6.2 Assembly

Once the parts were machined, the entire antenna was assembled on a custom made test stand. Before cleaning, baking and final assembly, the parts were checked thoroughly to ensure proper alignment. The first assembly is shown near completion in Fig. 6-3. To quantify part specifications and overall alignment and correct assembly, a Faro 3D coordinate measuring machine (CMM), shown in Fig. 6-4, was used. This tool allows 3D coordinate mapping of manufactured parts to 20 micron accuracy.

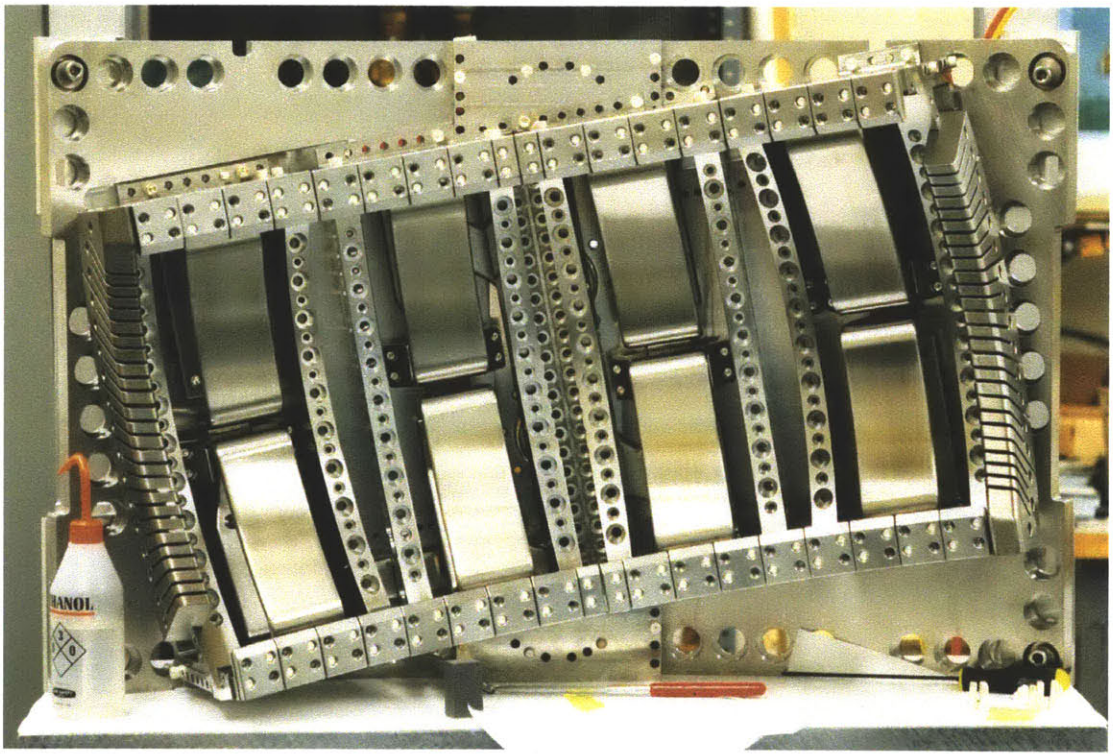

Figure 6-3: The entire antenna structure was assembled on a custom test stand to check alignment and overall part specifications. This image was taken immediately after the parts were machined, before plating and baking.

Once part specifications and assembly tolerances were met, parts were electroplated with copper. Plating thickness was chosen to be approximately 75 microns, which is an order of magnitude greater than the electrical skin depth at 80 MHz. This combination of Inconel substrate and copper plating serves two simultaneous purposes. First, because the resistivity of Inconel is approximately two orders of

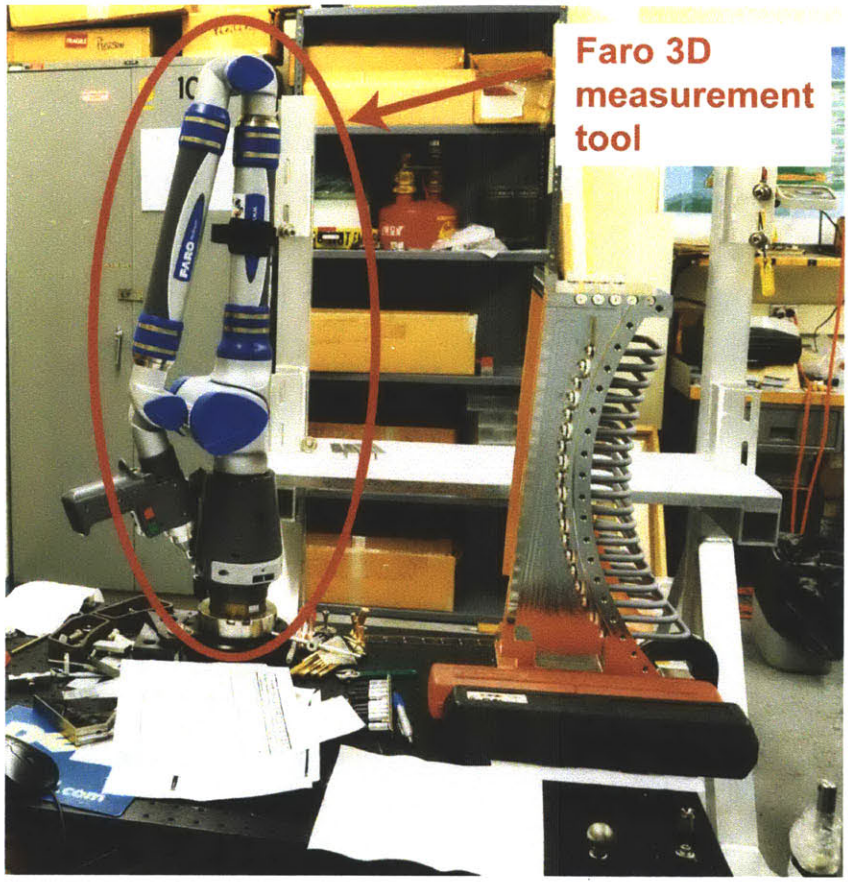

Figure 6-4: This is an image of one of two Faro coordinate measuring machines (CMMs) used to check alignment and manufacturing specifications.

magnitude higher than that of copper, current induced in the straps during a disruption is significantly lower than it would be for an all copper strap. Additionally, the tensile strength of Inconel is approximately five times that of copper, so it can better withstand the resulting $J \times B$ forces during a disruption. Second, the copper plating provides a low resistance path for the RF current. This way RF power losses and disruption effects are minimized at the same time.

Several components are shown in Fig. 6-5. One of four folded current straps is shown in Fig. 6-5 (a) along with the top and bottom of the box which will enclose it. One outer septum and one inner septum are shown in Fig. 6-5 (b). Fig. 6-5 (c) shows the feedthrough plate where the coaxial transmission line terminates before transitioning to stripline conductor. Figure 6-6 shows the bellows (a), which provide

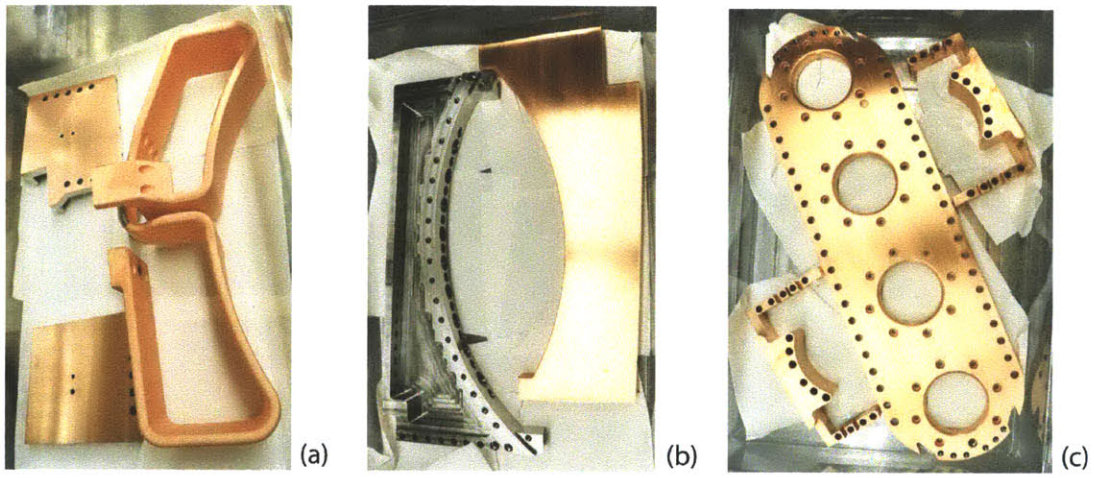

Figure 6-5: Several parts after copper plating: one current strap and top and bottom box panels (a); septa (un-plated outside on the left and plated inside on the right) (b); and coaxial feedthrough plate and covers (c).

some lateral movement between the striplines and the center conductors (b), during disruptions.

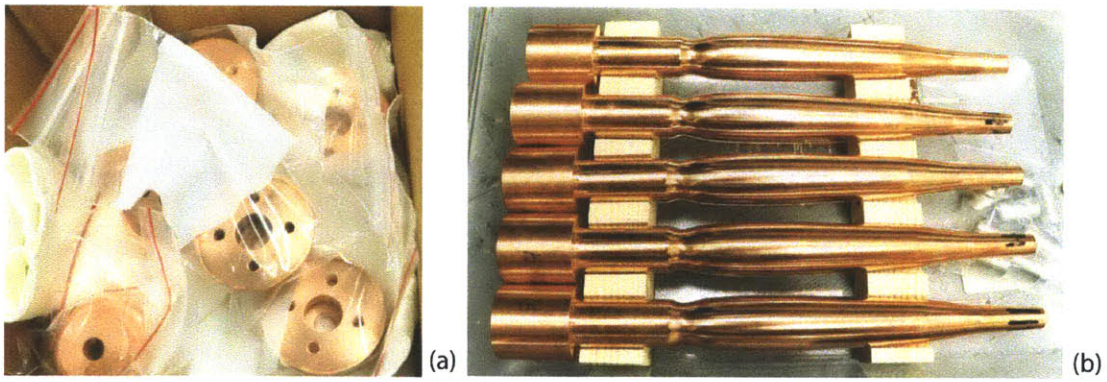

Figure 6-6: Two of the center conductor components are shown here. The bellows (a), allows some lateral movement between the center conductor (b), and stripline during disruptions.

Half of the stainless steel back plate is shown in Fig. 6-7 (a) after it has been plated. One of the current straps is shown in Fig. 6-7 (b) after electroplating and subsequent polishing. Before assembly onto the back plates around the current straps, each individual box structure is built as a sub-assembly as shown in Fig. 6-7 (c). Two striplines that will carry current from the center conductors to the current straps are

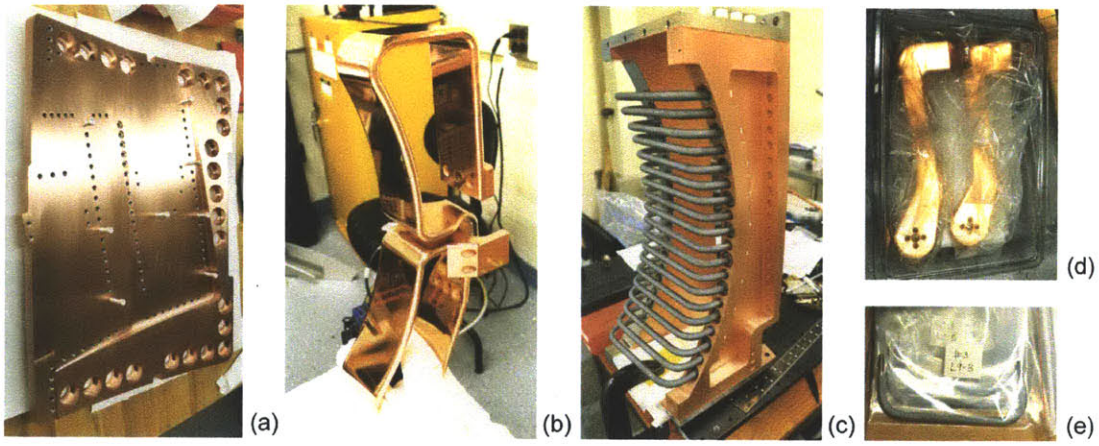

Figure 6-7: Antenna components: one of two back plates after plating (a); a current strap after copper plating and polishing (b); one of four assembled strap boxes (c); striplines for straps 1 and 4 (d); and coated and cleaned Faraday rods (e).

shown in Fig. 6-7 (d). These striplines will attach to the center conductor with four machine screws and the current strap with three machine screws. Cleaned and baked FS rods are shown in Fig. 6-7 (e) after they have been coated with TiBN.

Proper grounding is extremely important in RF systems, especially when high amounts of power are used. To ensure adequate grounding between the current straps and the antenna box, RF gaskets were machined into the contact locations as shown in Fig. 6-8. Similar gaskets were machined into the box walls to ensure proper grounding, prevent voltage arcs and isolate image currents within each box. In addition, copper plated stainless shim connectors were added to the structure to connect current straps two and three with the central Z-shaped plate used to shield the coaxial line feeds.

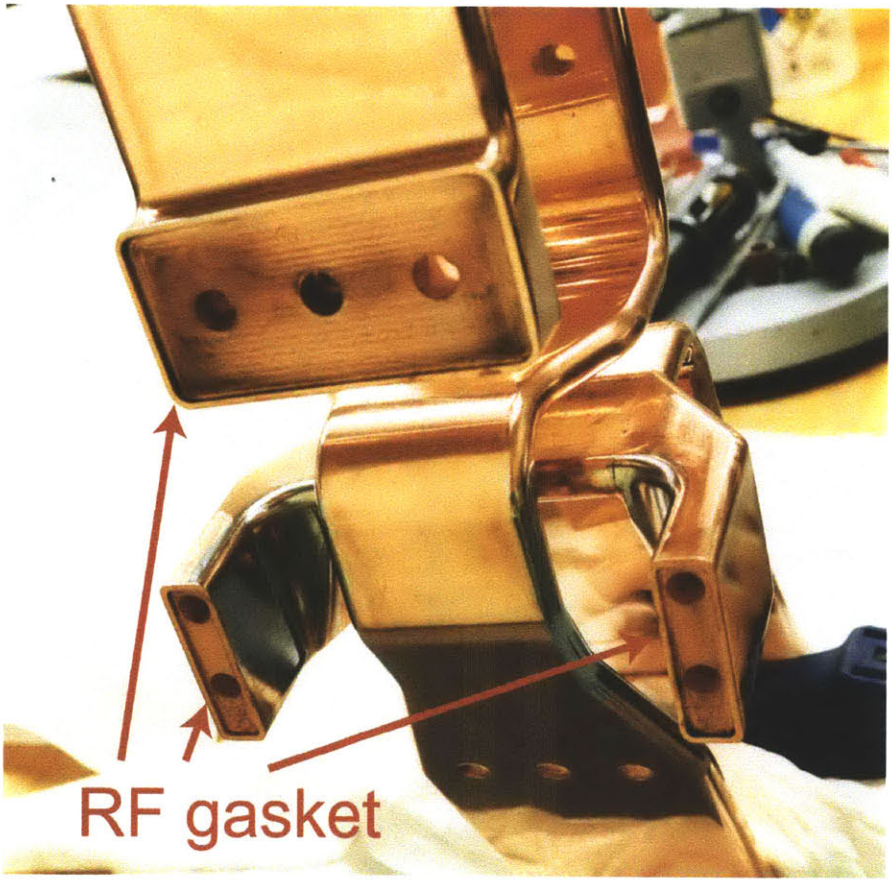

Figure 6-8: The three RF gaskets where the current straps connect to ground are shown. These gaskets ensure proper RF contact between the straps and antenna back plate.

6.3 Installation

Installation began with the complete removal of the previous four strap ICRF antenna located at J-port. Once the previous antenna was removed, the attachment studs in the vacuum vessel wall were ground down and new studs were welded into the vacuum vessel in preparation for the new antenna. First, the new coaxial feedlines were assembled and installed into the J horizontal port. Next, the port feedthrough plate was installed to the coaxial lines and outer wall. Then, the antenna back plates were installed on the outer wall of the vessel. The next step, shown in Fig. 6-9, was to install the current straps and striplines. Straps two and three are welded to their respective striplines prior to plating to form one continuous piece. However, straps one and four must be bolted to their respective striplines. These straps are installed first, then the striplines are attached to both the center conductors and current straps. Figure 6-10 shows all four straps fully installed, awaiting the attachment of the FS boxes.

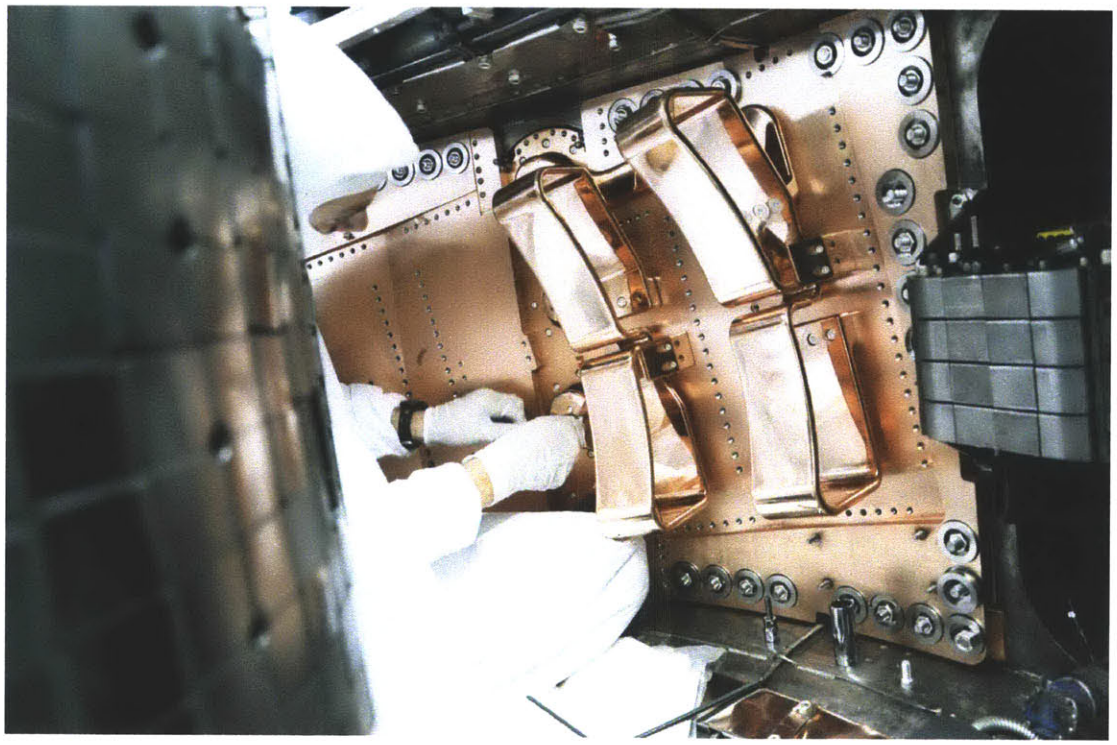

Figure 6-9: The field-aligned antenna straps being installed inside C-Mod.

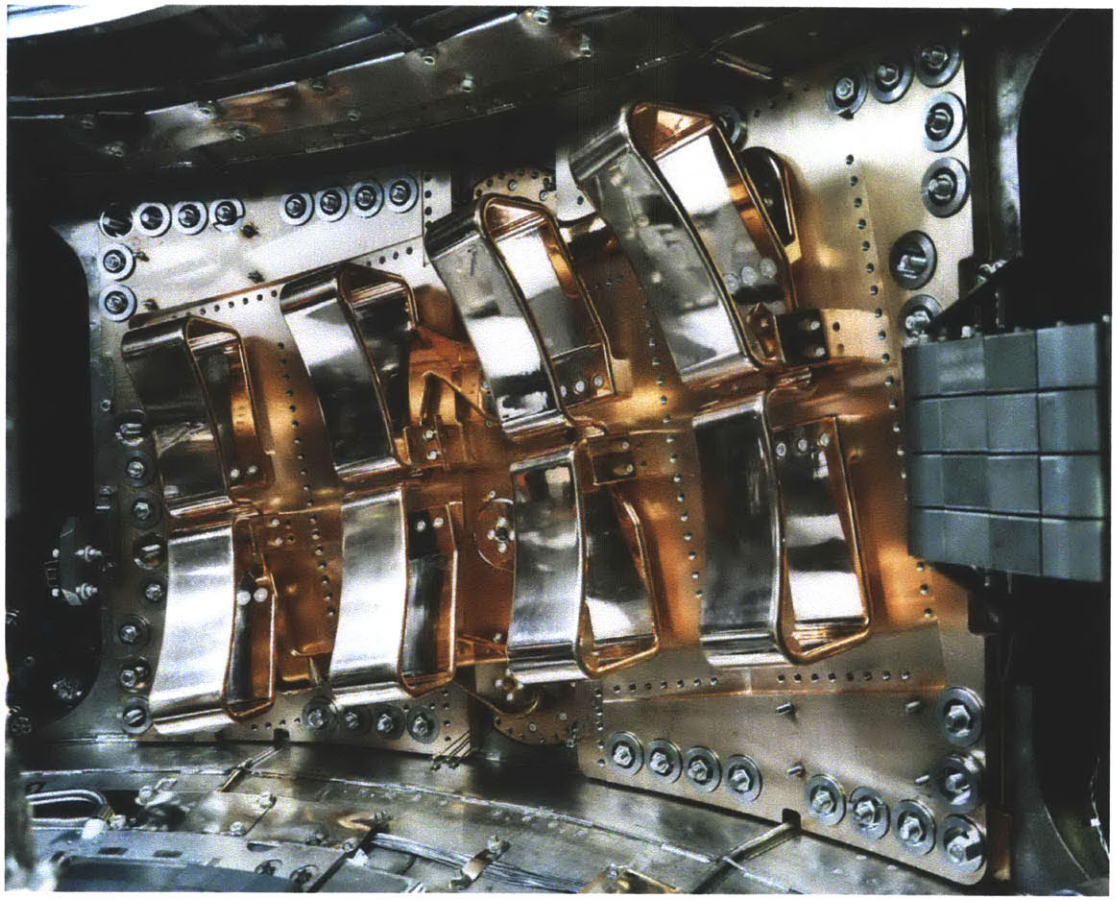

Figure 6-10: Prior to installing the individual boxes and Faraday rods, the four current straps are installed, torqued and checked.

Once the current straps and striplines are installed and torqued to specification, the FS boxes and tiles can be installed. The outer FS boxes are installed first, shown in Fig. 6-11, followed by the inner boxes. Each FS box has approximately 60 machine screws that are torqued to ensure proper RF grounding at the connection to the back plate. Following the box assembly, the diagnostic probes and leads are connected. There are two current probes and two voltage probes for each strap. These are positioned at the top and bottom of each FS box as shown in Fig. 6-12. There are also sets of thermocouples connected to the side limiter tiles to help quantify heat flux to the antenna structure. Once the thermocouples are in place, the remaining molybdenum protection tiles are torqued down and installation is complete. Figures 6-13 and 6-14 show the finished field-aligned antenna installed inside Alcator C-Mod.

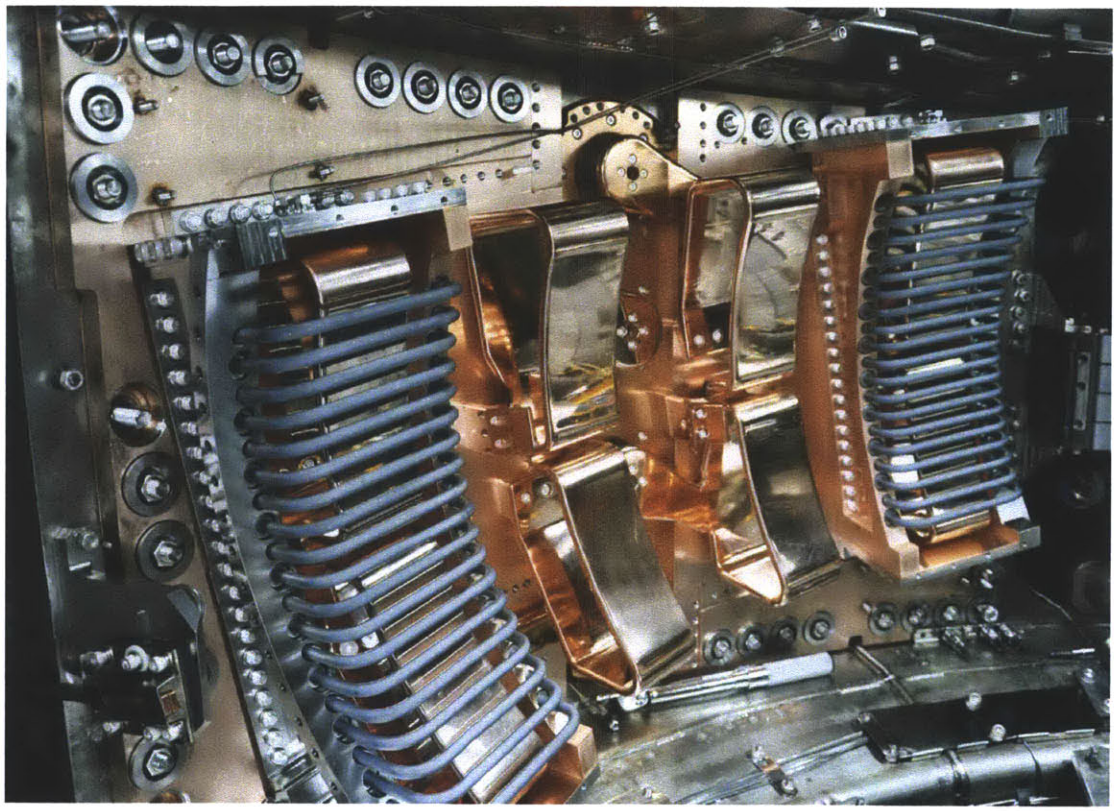

Figure 6-11: The outer two boxes are installed on the back plate.

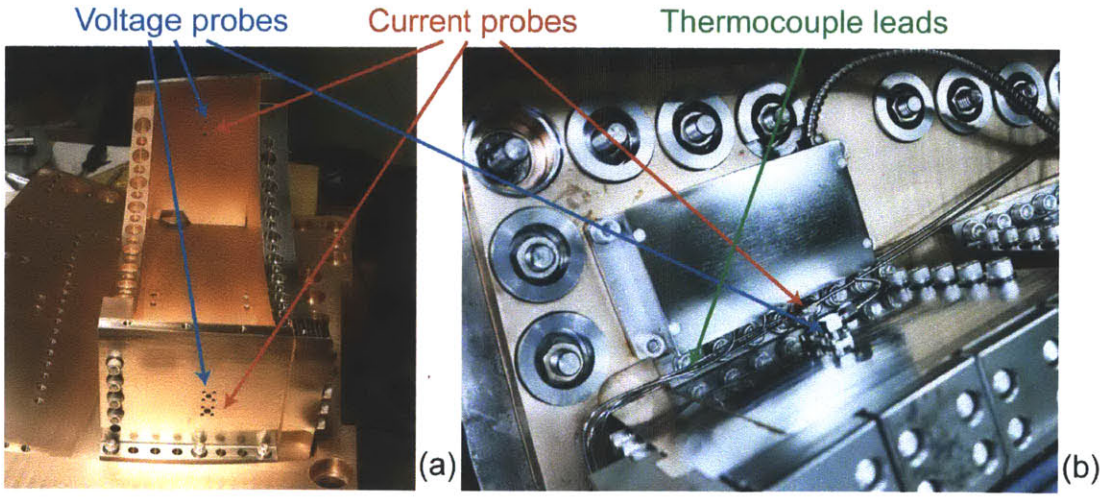

Figure 6-12: Each antenna strap box (a), has two voltage probes and two current probes. In addition, sets of thermocouple leads (b), are attached to individual side limiter tiles.

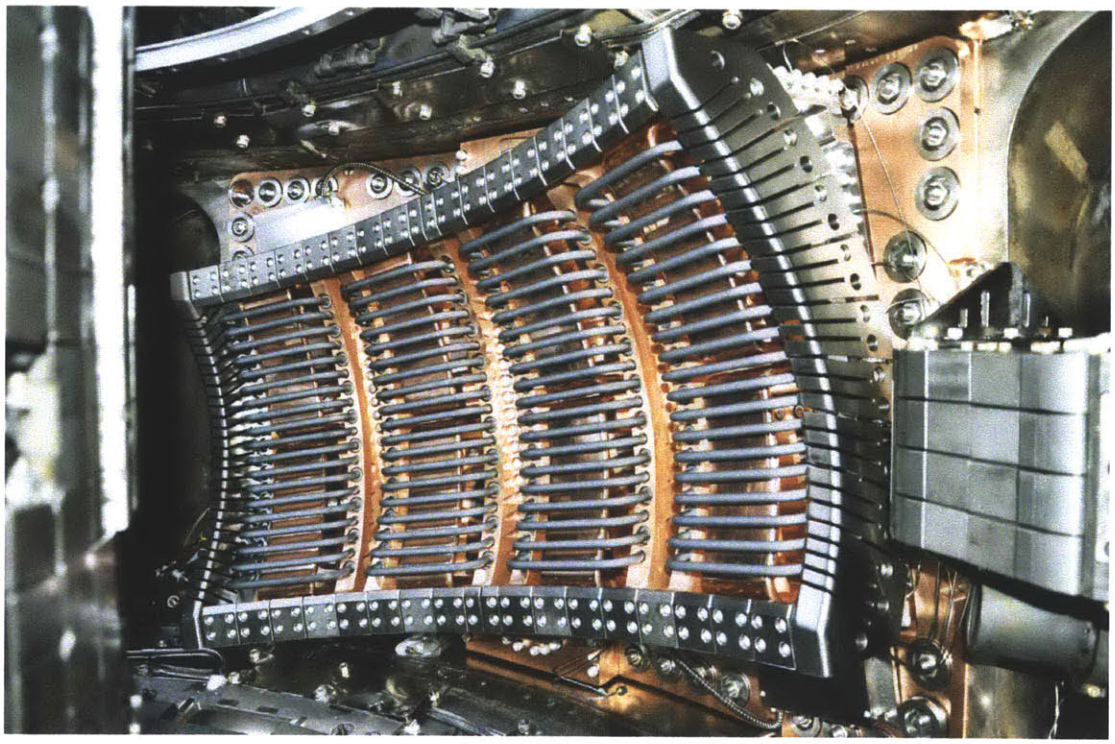

Figure 6-13: The field-aligned antenna installed inside C-Mod at J-port.

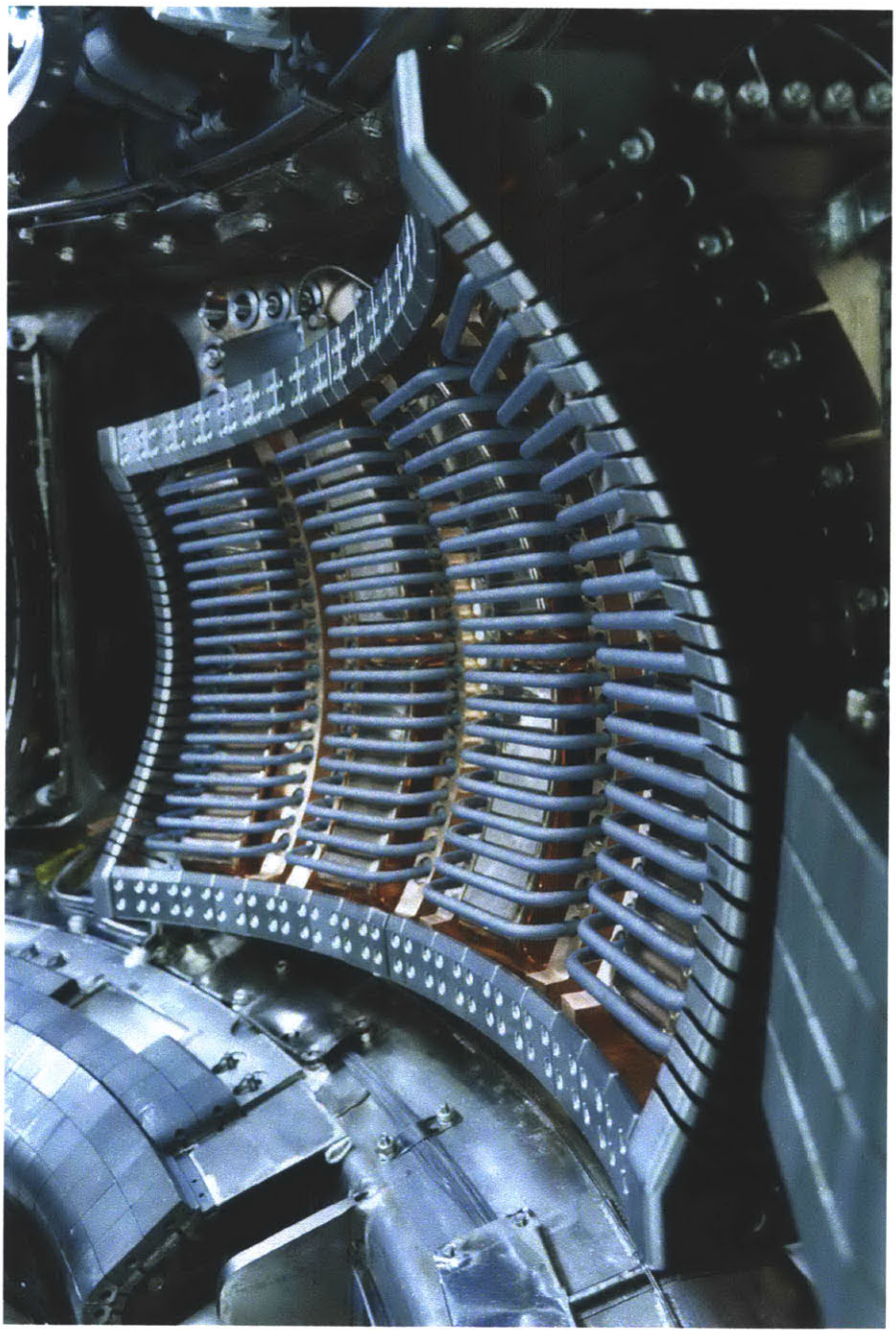

Figure 6-14: Edge view of the field-aligned antenna installed inside C-Mod at J-port.

Chapter 7

Experimental results

7.1 Experimental plan

Experiments were performed in December 2011 and January 2012 under Alcator C-Mod Mini-proposal 669 (MP669): Rotated Antenna Commissioning and Initial Characterization. The purpose of this experimental proposal was to commission and characterize the voltage, power, and neutral pressure limits of the newly installed magnetic field-aligned ICRF antenna. A second C-Mod Mini-proposal (MP681) was developed to investigate the performance, impurity characteristics, power and voltage limits at other antenna phases. However, an open-circuit condition developed at the transition from the coaxial center conductor feed to antenna stripline of strap number three. As a result, the new antenna was operated as a dipole antenna with only two of the four straps energized for the duration of proposal MP669.

7.1.1 Approach

For the initial antenna operation, a typical L-mode plasma with plasma current $I_p \approx$ 0.9MA, toroidal magnetic field $B_T \approx 5.4$T, and line-averaged density $n_{l04} \approx 0.8 \times 10^{20}\mathrm{m}^{-2}$ was chosen. The first operational goal was to obtain an impedance match to the plasma utilizing short RF pulses at low power $P_{RF} \leq 200$kW. Following initial vacuum testing, the RF power was increased to the maximum tolerable power level

in short pulses. After establishing a maximum short pulse power limit, the power was decreased and the pulse length was increased to investigate thermal limits. After quantifying the voltage and power handling characteristics, the neutral power limits were investigated.

Although originally envisioned for MP681, some initial impurity characteristics were investigated within MP669. To characterize the field-aligned antenna performance and impurity characteristics, the plasma response to the field-aligned antenna was compared to the plasma response to the non-aligned D and E antennas within the same discharge. Within each discharge, the field-aligned J antenna and non-aligned D and E antennas were energized for approximately 300 ms each, with 200 ms between RF pulses. To avoid issues with respect to plasma so-called *memory* (e.g. where the second H-mode is poorer than the first), the order of the antennas was also varied. Both L and H-mode plasmas were utilized since they have significantly different edge SOL, pedestal, and impurity characteristics. Plasma characteristics [stored energy, temperature, radiated power] were monitored using available diagnostics. The McPherson, Chromex, LoWEUS, and ZEUS spectrometers were used for global, antenna quadrant and mid-plane impurity views. The investigation of the plasma response dependence on antenna phasing and plasma current was not performed under MP669. However, once all four antenna straps are functioning normally these dependencies will be characterized under MP681 during July and August 2012.

7.1.2 Operational plan

The field-aligned antenna evaluation began with run day 1111209 on December 09, 2011. As planned, operation commenced with typical lower single null (LSN) plasmas with plasma current $I_p \approx 0.8$MA, toroidal magnetic field $B_T \approx 5.4$T, and line-averaged density $n_{l04} \approx 0.8 \times 10^{20}\text{m}^{-3}$. The field-aligned antenna conditioned quickly and reached $P_{RF} = 2$MW with sporadic faulting. To avoid dithering H-modes, the configuration was switched to upper single null (USN) after the fifth discharge. In USN, the plasma ended in alternating disruptions and fizzles and following shot num-

ber twelve the configuration was changed back to LSN. For the last two shots of the day, density was decreased to $n_{l04} \approx 0.6 \times 10^{20}\mathrm{m}^{-3}$ in LSN. During these shots it became clear that the field-aligned antenna was not functioning properly. The power distribution between the antenna straps was no longer symmetric. Upon inspection, the decoupling between straps had become particularly poor. Measurements were made of the individual straps revealing a problem with strap number three. Coaxial line was removed from the antenna power feed system until it was apparent that the problem was inside the C-Mod vacuum barrier. A boroscope was inserted into the vessel to attempt to diagnose the problem with strap number three. A physical gap was observed between the transition of the coaxial center conductor and the bellows at the stripline to coaxial connection as seen in Fig. 7-1.

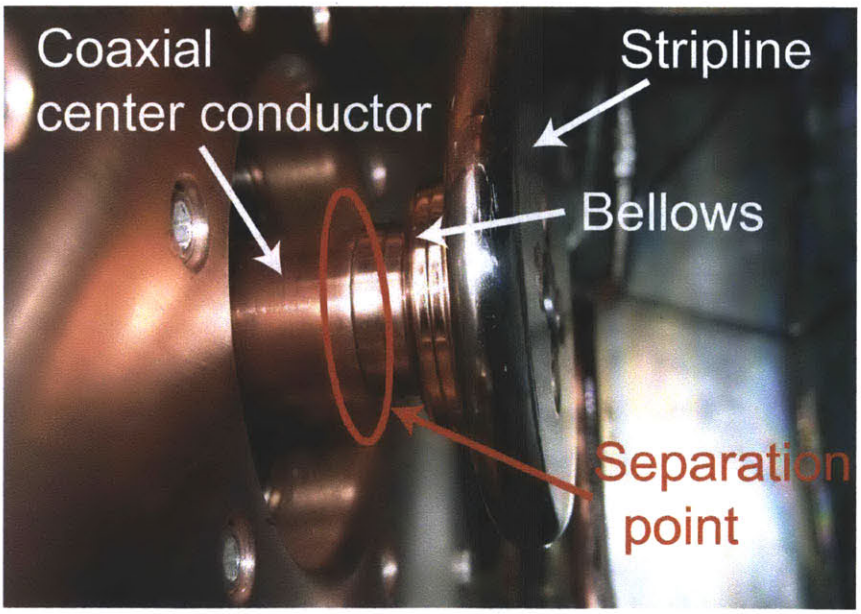

Figure 7-1: One of four coaxial to stripline transitions in the field-aligned antenna. The center conductor, bellows and stripline are shown. In addition, the transition from center conductor to bellows where separation occurred on strap three, is circled in red.

It was determined that the transition could not be repaired without breaking vacuum. As a result, the decision was made to attempt to continue operation with the field-aligned antenna reconfigured as a two-strap dipole. Straps three and four were shorted and only straps one and two were energized for the remaining campaign.

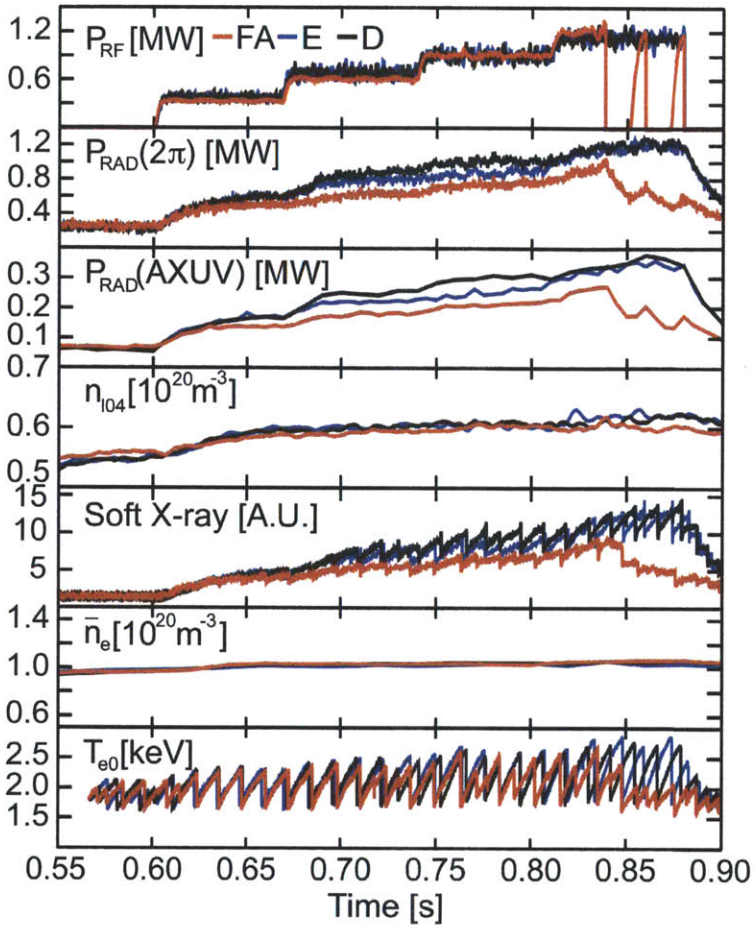

Figure 7-2: Overlay of three pre-boronization plasma discharges: 1120104033, 1120104034, 1120104036. The field-aligned antenna is shown in red, the D-port antenna is shown in black, and the E-port antenna is shown in blue.

7.1.3 Dipole operation and experimental results

Characterization of the field-aligned antenna as a two-strap antenna began with run 1120104 on January 04, 2012. This run day was the first operation after the boroscope inspection. As such, the primary objective was to assess machine condition. However, ICRF conditioning of the two-strap field-aligned antenna was done in parallel. Three discharges (1120104033, 1120104034, 1120104036), shown in Fig. 7-2, illustrate a reduction in radiated power, and thus impurity content, for the field-aligned antenna relative to the D-port and E-port antennas. For each shot, RF power is on from $t = 0.60$ s to $t = 0.88$ s, and is stepped in four increments: 0.4 MW, 0.8 MW, 1.0

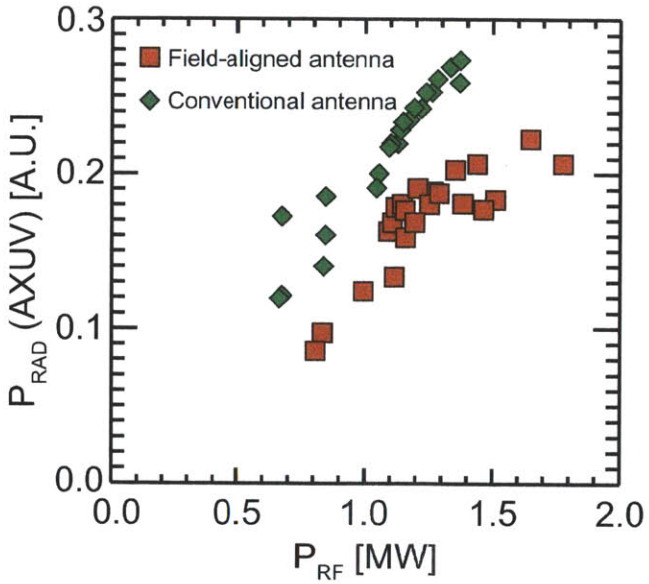

Figure 7-3: Comparison of radiated power versus RF input power for the field-aligned antenna with a conventional antenna. [Figure courtesy of S.J. Wukitch]

MW and 1.2 MW. Both density (n_{l04} , $\bar{n}_e$) and electron temperature (T_{e0}) are virtually identical for the three pulses shown in Fig. 7-2. However, radiated power measured on the Absolute eXtreme Ultra Violet (AXUV) photodiodes, the 2π-diodes, and the soft X-ray (SXR) detectors is significantly lower for the field-aligned antenna.

The first dedicated two-strap field-aligned antenna run was 1120124 on January 24, 2012. The field-aligned antenna conditioned significantly faster than either of the conventional two-strap antennas located at D-port and E-port. The field-aligned antenna reached voltages of 45 kV at input power of 1.5 MW in a series of enhanced D_α (EDA) H-modes. Additionally, changes in antenna loading during L-H transitions were smaller for the field-aligned antenna than for the D or E-port antennas. Unfortunately, a leak in the alternator air-switch resulted in a shortened run day.

Evaluation of the antenna was continued the following day with run 1120125 on January 25, 2012. A set of discharges were run where each antenna was operated in series, one after the other. The order of antenna operation was changed from shot to shot to ensure accurate comparison. Antenna No. 1 operated from 0.60 s to 0.90 s, antenna No. 2 operated from 0.95 s to 1.25 s, and antenna No. 3 operated from

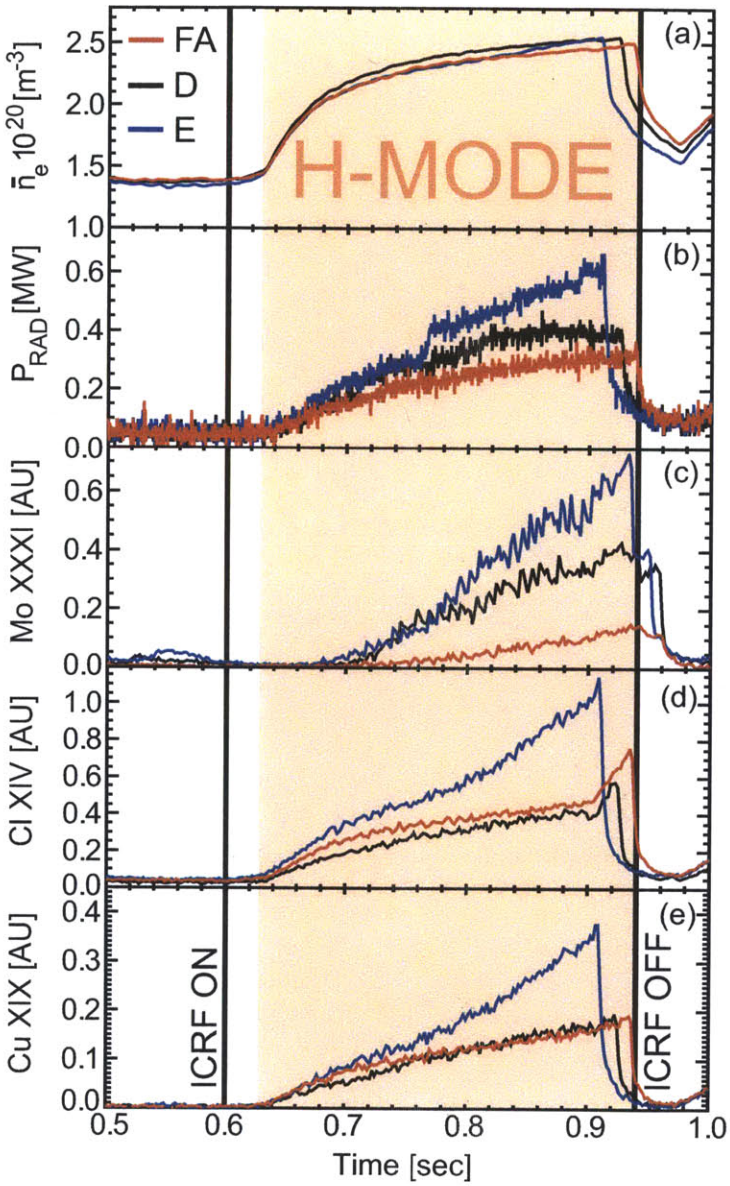

Figure 7-4: Comparison of impurity characteristics of the field-aligned antenna (red) with the D-port (black) and E-port (blue) antennas. H-mode duration and the points where ICRF power (1.0 MW) is turned on and off are indicated. Line averaged electron density (a), total radiated power (b), molybdenum (Mo XXXI) brightness (c), chlorine (Cl XIV) brightness (d), and copper (Cu XIX) brightness (e) are shown. [Figure courtesy of M.L. Reinke]

1.30 s to 1.60 s. Radiated power was consistently lower for the field-aligned antenna. Figure 7-3 shows radiated power (AXUV) as a function of RF power. While P_{RAD} increases as P_{RF} increases for both the field-aligned and conventional antennas, both the slope and magnitude of the increase is smaller for the field-aligned antenna.

Figure 7-4 shows a series of three discharges (1120125007, 1120125009, 1120125010), where ICRF was on from $t = 0.60$ s to $t = 0.95$ s. These discharges are all post-boronization and help to assess the boronization recovery of the antennas. The field-aligned antenna recovered immediately, reaching 1 MW RF power after a single shot. The E-port antenna reached 1 MW after two shots and the D-port antenna reached 1 MW power after five shots. This improvement for the field-aligned antenna is likely the result of enhanced voltage handling and a higher neutral pressure limit. The transition into H-mode confinement can be seen with the corresponding density increase in Fig. 7-4 (a). Volumetric radiated power, shown in (b) is significantly higher for both D and E-port antennas than for the field-aligned antenna. In Fig. 7-4, spectral brightness for molybdenum (Mo XXXI) (c), chlorine (Cl XIV) (d), and copper (Cu XIX) is plotted for all three antennas. Note that the radiation from highly stripped core molybdenum (Mo XXXI) is significantly lower for the field-aligned antenna than for the conventional antennas. For the intrinsic impurities chlorine and copper, shown in Fig. 7-4 (d) and (e), respectively, the radiation for both the field-aligned antenna and D-port antenna are lower than that of the E-port antenna.

Another interesting observation from Fig. 7-4 is that the radiation from these intrinsic impurities increases almost immediately after the plasma transitions into H-mode confinement at $t = 0.63$ s. However, the molybdenum brightness begins to increase approximately 50 ms after H-mode begins. This might suggest that the molybdenum brightness increase is transport related. If the Mo XXXI brightness was simply related to enhanced sputtering at the Mo tile surfaces, the increase would be expected immediately, instead of the observed delay. However, edge density evolution and a delay in the onset of the enhanced sheath may also play a role.

Figure 7-5 shows neutral Molybdenum (Mo I) brightness from the Chromex spectrometer for two different discharges where the order of antenna excitation was

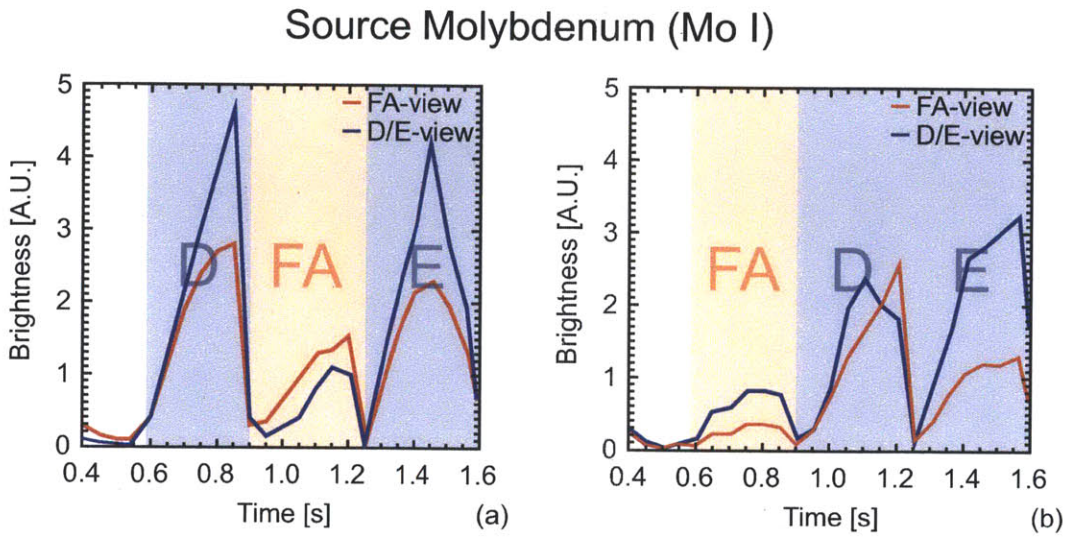

Figure 7-5: Source molybdenum (Mo I) brightness from views of either the field-aligned antenna or the D-port/E-port antenna when either the field-aligned antenna, the D-port antenna, or the E-port antenna is energized.

changed. In both plots (a) and (b), the red trace represents a view of the field-aligned antenna (FA-view), while the blue trace represents a view of the D-port and E-port antennas (D/E-view). In 7-5 (a) the order of antenna excitation is D-FA-E. For 7-5 (b) the order of antenna excitation is FA-D-E. In each case the brightness observed from views of all antennas is lower when the field-aligned antenna is powered relative to the conventional ICRF antennas.

Chapter 8

Discussion and conclusions

8.1 Comparison of simulation with experiment

Experimental data presented in this thesis are necessarily limited by the narrow operational regime of the field-aligned antenna as a 2-strap, fixed toroidal phase device. As described in Ch. 7, the electro-mechanical separation of current strap number three has prevented normal operation of the field-aligned antenna. As a result, only a small number of discharges over a few run days provide quantitative results on the operating characteristics of the new antenna. However, for the case of dipole phasing, there were enough data to at least begin a cursory analysis of the antenna performance. These data, presented in Ch. 7, suggest that alignment of the antenna structure with the equilibrium magnetic field improves impurity characteristics. Simulation results shown in Ch. 5 suggested a reduction in $V_{\mathrm{RF}} = \int \frac{\boldsymbol{E}_{RF} \cdot \boldsymbol{B}}{|B|} dl$ of approximately 40 % for the dipole-phased field-aligned antenna compared with the conventional antenna. For the reconfigured 2-strap version of the field-aligned antenna, experimental data shown in Ch. 7 reveal a reduction in radiated power of 20 % to 100 %, relative to the conventional ICRF antennas.

8.2 Conclusions

A new magnetic field-aligned ICRF antenna was designed, optimized, installed and operated inside Alcator C-Mod. Finite element simulations were developed for two and four strap ICRF antennas in slab, cylindrical and toroidal geometry for cold plasma and isotropic dielectric loads. Linear 3-D coupling studies of ICRF waves in C-Mod were performed for a rotated four strap antenna using a FEM code which includes the actual SOL density profiles, the 3-D solid geometry of the launcher, with a cold plasma load. The results indicate that an ICRF antenna aligned with the total Alcator C-Mod magnetic field could reduce the average RF potential along magnetic field lines intersecting the antenna by a factor of 2–3. In addition, the largest reduction in V_{RF} occurs for monopole phasing and pseudo-monopole phasing, which provide the optimum magnetic flux coupling to the plasma. Through this reduction in RF potential, both source and transport impurity characteristics in Alcator C-Mod are expected to improve during ICRF operation of the field-aligned antenna. Initial results suggest that impurity characteristics are improved during operation of the field-aligned antenna relative to the conventional antennas.

8.3 Future work

Beginning in June 2012, these experiments will be revisited using the repaired field-aligned antenna with all four current straps operational. To characterize the field-aligned antenna performance, the plasma response to the field-aligned antenna will be compared to the plasma response to the D and E antennas within the same discharge. In particular, we are interested in impurity characteristics, SOL density profile modification, plasma potential variation, and SOL transport. We will investigate the plasma response dependence on antenna phasing and plasma current. Within each discharge, we will pulse field-aligned and D -port and E-port antennas for $\sim$ 300 ms each, with 200 ms between RF pulses. Both L and H-mode plasmas will be utilized since they have significantly different edge SOL, pedestal, and impurity characteristics. For the

initial operation, we will utilize [0, π , 0, π] and switch to [0, 0, 0, 0] electronically. Since we need to switch the transmission line network to access heating [0, π, π, 0] and current drive [0, $\pi/2$, π, $3\pi/2$] phasing, we will need a separate run day.

Plasma current will also be swept to quantify the effect of magnetic pitch angle on impurity production and transport. We will monitor plasma characteristics [stored energy, temperature, radiated power] using available diagnostics. We will use McPherson, Chromex, LoWEUS, and ZEUS spectrometers for global, antenna quadrant and mid-plane impurity views. The SOL reflectometer and GPI will be used to monitor SOL density and transport modifications. We will also use emissive probes at the AB limiter to monitor plasma potential.

In parallel, numerical techniques will be enhanced to better understand experimental results. First, a non-linear RF sheath boundary condition will be implemented in the FEM code. Second, edge density fluctuations and convective cell formation will be investigated within the framework of existing FEM codes and particle in cell (PIC) codes to better quantify ICRF-related SOL transport and turbulence.

Bibliography

[1] ITER Physics Basis Editors, ITER Physics Expert Group Chairs, Co-Chairs, ITER Joint Central Team, and Physics Integration Unit. ITER physics basis, chapter 1: Overview and summary. *Nuclear Fusion*, 39(12):2137, 1999.

[2] J.R. Myra, D.A. D'Ippolito, and M.J. Gerver. Faraday screen sheaths and impurity production during ion cyclotron heating. *Nuclear Fusion*, 30(5):845, 1990.

[3] M. Bures, H. Brinkschulte, J. Jacquinot, K. D. Lawson, A. Kaye, and J. A. Tagle. The modification of the plasma edge and impurity production by antenna phasing during ICRF heating on JET. *Plasma Physics and Controlled Fusion*, 30(2):149, 1988.

[4] F.W. Perkins. Radiofrequency sheaths and impurity generation by ICRF antennas. *Nuclear Fusion*, 29(4):583, 1989.

[5] B.C. Stratton, H.W. Moos, W.L. Hodge, S. Suckewer, J.C. Hosea, R.A. Hulse, D.Q. Hwang, and J.R. Wilson. Changes in impurity radiation during ICRF heating of PLT tokamak plasmas. *Nuclear Fusion*, 24(6):767, 1984.

[6] H.L. Manning, J.L. Terry, B. Lipschultz, B. LaBombard, B.D. Blackwell, C.L. Fiore, M.E. Foord, E.S. Marmar, J.D. Moody, R.R. Parker, M. Porkolab, and J.E. Rice. Impurity generation during ICRF heating experiments on Alcator C. *Nuclear Fusion*, 26(12):1665, 1986.

[7] F. Waelbroeck, J. Winter, G. Esser, B. Giesen, L. Konen, V. Philipps, U. Samm, J. Schluter, P. Weinhold, The TEXTOR Team, and T. Banno. Influence of boronization on the plasma performance in TEXTOR. *Plasma Physics and Controlled Fusion*, 31(2):185, 1989.

[8] M. Bures, J.J. Jacquinot, M.F. Stamp, D.D.R. Summers, D.F.H. Start, T. Wade, D.A. D'Ippolito, and J.R. Myra. Assessment of beryllium Faraday screens on the JET ICRF antennas. *Nuclear Fusion*, 32(7):1139, 1992.

[9] B. Lipschultz, Y. Lin, M. L. Reinke, A. Hubbard, I. H. Hutchinson, J. Irby, B. LaBombard, E. S. Marmar, K. Marr, J. L. Terry, S. M. Wolfe, the Alcator C-Mod group, and D. Whyte. Operation of Alcator C-Mod with high-Z plasma facing components and implications. *Physics of Plasmas*, 13(5):056117, 2006.

[10] L.L. Lao, H. St. John, R.D. Stambaugh, A.G. Kellman, and W. Pfeiffer. Reconstruction of current profile parameters and plasma shapes in tokamaks. *Nuclear Fusion*, 25(11):1611, 1985.

[11] Department of Economic United Nations and Social Affairs Population Division. World population to 2300, 2004.

[12] J.P. Freidberg. *Plasma Physics and Fusion Energy.* Cambridge University Press, 2007.

[13] V.P. Smirnov. Tokamak foundation in USSR/russia 1950 to 1990. *Nuclear Fusion*, 50(1):014003, 2010.

[14] J. Wesson. *Tokamaks.* Oxford University Press, 1996.

[15] T.H. Stix. *Waves in plasmas.* Amer. Inst. of Physics, 1992.

[16] F.W. Perkins. Heating tokamaks via the ion-cyclotron and ion-ion hybrid resonances. *Nuclear Fusion*, 17(6):1197, 1977.

[17] I. H. Hutchinson, R. Boivin, F. Bombarda, P. Bonoli, S. Fairfax, C. Fiore, J. Goetz, S. Golovato, R. Granetz, M. Greenwald, S. Horne, A. Hubbard, J. Irby, B. LaBombard, B. Lipschultz, E. Marmar, G. McCracken, M. Porkolab, J. Rice, J. Snipes, Y. Takase, J. Terry, S. Wolfe, C. Christensen, D. Garnier, M. Graf, T. Hsu, T. Luke, M. May, A. Niemczewski, G. Tinios, J. Schachter, and J. Urbahn. First results from Alcator C-Mod. *Physics of Plasmas*, 1(5):1511–1518, 1994.

[18] S.N. Golovato, W. Beck, P. Bonoli, M. Fridberg, M. Porkolab, and Y. Takase. Antennas for ICRF heating in the Alcator C-Mod tokamak. In *Fusion Engineering, 1993., 15th IEEE/NPSS Symposium on*, volume 2, pages 1069 –1072 vol.2, oct 1993.

[19] S.J. Wukitch, B. LaBombard, Y. Lin, B. Lipschultz, E. Marmar, M.L. Reinke, and D.G. Whyte. ICRF specific impurity sources and plasma sheaths in Alcator C-Mod. *Journal of Nuclear Materials*, 390-391:951 – 954, 2009.

[20] Y. Takase, S. Golovato, M. Porkolab, K. Bajwa, H. Becker, and D. Caldwell. Engineering design and analysis of the Alcator C-Mod two-strap ICRF antenna. In *Fusion Engineering, 1991. Proceedings., 14th IEEE/NPSS Symposium on*, pages 118 –121 vol.1, sep-3 oct 1991.

[21] G. Schilling, JC Hosea, JR Wilson, PT Bonoli, WD Lee, E. Nelson-Melby, M. Porkolab, and SJ Wukitch. Extension of Alcator C-Mod's ICRF experimental capability. In *AIP Conference Proceedings*, pages 429–432. IOP INSTITUTE OF PHYSICS PUBLISHING LTD, 1999.

[22] A. Parisot, S. J. Wukitch, P. T. Bonoli, J. W. Hughes, B. LaBombard, Y Lin, R Parker, M Porkolab, and A K Ram. ICRF loading studies on Alcator C-Mod. *Plasma Physics and Controlled Fusion*, 46(11):1781, 2004.

[23] S. J. Wukitch, Y. Lin, B. Lipschultz, A. Parisot, M. Reinke, P. T. Bonoli, M. Porkolab, I. H. Hutchinson, and E. Marmar Alcator C-Mod Team. ICRF performance with metallic plasma facing components in Alcator C-Mod. *AIP Conference Proceedings*, 933(1):75–82, 2007.

[24] J. M. Noterdaeme and G. Van Oost. The interaction between waves in the ion cyclotron range of frequencies and the plasma boundary. *Plasma Physics and Controlled Fusion*, 35(11):1481, 1993.

[25] M. Bures, J. Jacquinot, K. Lawson, M. Stamp, H. P. Summers, D. A. D'Ippolito, and J. R. Myra. Impurity release from the ICRF antenna screens in JET. *Plasma Physics and Controlled Fusion*, 33(8):937, 1991.

[26] D.A. D'Ippolito, J.R. Myra, P.M. Ryan, E. Righi, J. Heikkinen, P.U. Lamalle, J.-M. Noterdaeme, and Contributors to the EFDAJET Workprogramme. Modelling of mixed-phasing antenna-plasma interactions on JET A2 antennas. *Nuclear Fusion*, 42(12):1357, 2002.

[27] E. Lerche, V. Bobkov, P. Jacquet, M.-L. Mayoral, A. Messiaen, I. Monakhov, J. Ongena, G. Telesca, D. Van Eester, and R. R. Weynants JET-EFDA contributors. Recent experiments on alternative dipole phasing with the JET A2 ICRF antennas. *AIP Conference Proceedings*, 1187(1):93–96, 2009.

[28] R. Van Nieuwenhove and G. Van Oost. Experimental evidence for sheath effects at the ICRF antenna and ensuing changes in the plasma boundary during ICRF on TEXTOR. *Journal of Nuclear Materials*, 162-164:288 – 291, 1989.

[29] R. Van Nieuwenhove and G. Van Oost. Experimental study of sheath currents in the scrape-off layer during ICRH on TEXTOR. *Plasma Physics and Controlled Fusion*, 34(4):525, 1992.

[30] R. Van Nieuwenhove, R. Koch, G. Van Oost, J.A. Boedo, P. Dumortier, F. Durodie, P. Lamalle, D. Lebeau, A.M. Messiaen, J. Ongena, B. Schweer, C. Stickelmann, G. Telesca, P.E. Vandenplas, G. Van Wassenhove, and M. Vervier. Comparison of the performance of ICRF antennas with and without Faraday shield on TEXTOR. *Nuclear Fusion*, 32(11):1913, 1992.

[31] J. E. Stevens, C. Bush, P. L. Colestock, G. J. Greene, K. W. Hill, J. C. Hosea, C. K. Phillips, B. Stratton, S. von Goeler, J. R. Wilson, W. Gardner, D. Hoffman, and A. Lysojvan. The effect of ICRF antenna phasing on metal impurities in TFTR. *Plasma Physics and Controlled Fusion*, 32(3):189, 1990.

[32] D.A. D'Ippolito, J.R. Myra, J.H. Rogers, K.W. Hill, J.C. Hosea, R. Majeski, G. Schilling, J.R. Wilson, G.R. Hanson, A.C. England, and J.B. Wilgen. Analysis of RF sheath interactions in TFTR. *Nuclear Fusion*, 38(10):1543, 1998.

[33] T. Fujii, M. Saigusa, H. Kimura, S. Moriyama, H. Kubo, T. Sugie, and N. Hosogane. Performance of toroidally wide-separation loop antennae for JT-60U ICRF experiments. *Fusion Engineering and Design*, 26(1-4):377 – 385, 1995.

[34] C.E. Thomas Jr., J.H. Harris, G.R. Haste, C.C. Klepper, J. Hogan, S.J. Tobin, F.W. Baity, M.D. Carter, D.J. Hoffman, P.M. Ryan, B. Saoutic, B. Beaumont, A. Becoulet, H. Kuus, D. Fraboulet, A. Grosman, D. Guilhem, J.Y. Pascal, J. Valter, T. Loarer, and M. Chatelier. First measurements of ICRF and edge/SOL plasma interactions on Tore Supra. *Journal of Nuclear Materials*, 220-222(0):531 – 535, 1995.

[35] M. Becoulet, L. Colas, S. Pecoul, J. Gunn, Ph. Ghendrih, A. Becoulet, and S. Heuraux. Edge plasma density convection during ion cyclotron resonance heating on Tore Supra. *Physics of Plasmas*, 9(6):2619–2632, 2002.

[36] L. Colas, L. Costanzo, C. Desgranges, S. Brmond, J. Bucalossi, G. Agarici, V. Basiuk, B. Beaumont, A. Bcoulet, and F. Nguyen. Hot spot phenomena on Tore Supra ICRF antennas investigated by optical diagnostics. *Nuclear Fusion*, 43(1):1, 2003.

[37] L. Colas, V. Basiuk, B. Beaumont, A. Bécoulet, G. Bosia, S. Brémond, M. Chantant, F. Clairet, A. Ekedahl, E. Faudot, A. Géraud, M. Goniche, S. Heuraux, G.T. Hoang, G. Lombard, L. Millon, R. Mitteau, P. Mollard, K. Vulliez, and the Tore Supra team. Key results of long pulse ICRH operation in Tore Supra. *Nuclear Fusion*, 46(7):S500, 2006.

[38] B. Lipschultz, D.A. Pappas, B. LaBombard, J.E. Rice, D. Smith, and S.J. Wukitch. A study of molybdenum influxes and transport in Alcator C-Mod. *Nuclear Fusion*, 41(5):585, 2001.

[39] S.J. Wukitch, B. Lipschultz, E. Marmar, Y. Lin, A. Parisot, M. Reinke, J. Rice, and J. Terry. RF plasma edge interactions and their impact on ICRF antenna performance in alcator c-mod. *Journal of Nuclear Materials*, 363-365(0):491 – 497, 2007.

[40] S. J. Wukitch, R. L. Boivin, P. T. Bonoli, J. A. Goetz, J. Irby, I. Hutchinson, Y. Lin, A. Parisot, M. Porkolab, E. Marmar, G. Schilling, and J. R. Wilson. Investigation of performance limiting phenomena in a variable phase ICRF antenna in Alcator C-Mod. *Plasma Physics and Controlled Fusion*, 46(9):1479, 2004.

[41] V. Bobkov, R. Bilato, F. Braun, L. Colas, R. Dux, D. Van Eester, L. Giannone, M. Goniche, A. Herrmann, P. Jacquet, A. Kallenbach, A. Krivska, E. Lerche, M.-L. Mayoral, D. Milanesio, I. Monakhov, H. W. Muller, R. Neu, J.-M. Noterdaeme, Th. Putterich, and V. Rohde ASDEX Upgrade Team JET-EFDA Contributors. Interaction of ICRF fields with the plasma boundary in AUG and JET and guidelines for antenna optimization. *AIP Conference Proceedings*, 1187(1):125–132, 2009.

[42] V. Bobkov, F. Braun, R. Dux, L. Giannone, A. Herrmann, A. Kallenbach, H.W. Muller, R. Neu, J.M. Noterdaeme, T. Putterich, and V. Rohde. Operation of ICRF antennas in a full tungsten environment in ASDEX Upgrade. *Journal of Nuclear Materials*, 390-391(0):900 – 903, 2009.

[43] V. Bobkov, F. Braun, R. Dux, A. Herrmann, L. Giannone, A. Kallenbach, A. Krivska, H.W. Muller, R. Neu, J.-M. Noterdaeme, T. Putterich, V. Rohde, J. Schweinzer, A. Sips, I. Zammuto, and ASDEX Upgrade Team. Assessment of compatibility of ICRF antenna operation with full W wall in ASDEX Upgrade. *Nuclear Fusion*, 50(3):035004, 2010.

[44] R. Neu, V. Bobkov, R. Dux, A. Kallenbach, Th. Ptterich, H. Greuner, O. Gruber, A. Herrmann, Ch. Hopf, K. Krieger, C.F. Maggi, H. Maier, M. Mayer, V. Rohde, K. Schmid, and W. Suttrop. Final steps to an all tungsten divertor tokamak. *Journal of Nuclear Materials*, 363-365(0):52 – 59, 2007.

[45] V. Bobkov, F. Braun, L. Colas, R. Dux, H. Faugel, L. Giannone, A. Herrmann, A. Kallenbach, H.W. Muller, R. Neu, J.-M. Noterdaeme, T. Putterich, G. Siegl, and E. Wolfrum. ICRF antenna-plasma interactions and its influence on W sputtering in ASDEX Upgrade. *Journal of Nuclear Materials*, 415(1, Supplement):S1005 – S1008, 2011.

[46] D.A. D'Ippolito and J.R. Myra. ICRF-edge and surface interactions. *Journal of Nuclear Materials*, 415(1, Supplement):S1001 – S1004, 2011.

[47] D. A. D'Ippolito, J. R. Myra, M. Bures, and J. Jacquinot. A model of sheath-driven impurity production by ICRF antennas. *Plasma Physics and Controlled Fusion*, 33(6):607, 1991.

[48] D. A. D'Ippolito, J. R. Myra, J. Jacquinot, and M. Bures. Radio-frequency-sheath-driven edge plasma convection and interaction with the H mode. *Physics of Fluids B: Plasma Physics*, 5(10):3603–3617, 1993.

[49] J.R. Myra, D.A. D'Ippolito, D.A. Russell, L.A. Berry, E.F. Jaeger, and M.D. Carter. Nonlinear ICRF-plasma interactions. *Nuclear Fusion*, 46(7):S455, 2006.

[50] J. R. Myra and D. A. D'Ippolito. Far field ICRF sheath formation on walls and limiters. *AIP Conference Proceedings*, 289(1):421–424, 1994.

[51] L. Colas, A. Ekedahl, M. Goniche, J. P. Gunn, B. Nold, Y. Corre, V. Bobkov, R. Dux, F. Braun, J. M. Noterdaeme, M. L. Mayoral, K. Kirov, J. Mailloux, S. Heuraux, E. Faudot, J. Ongena, ASDEX Upgrade Team, and JET-EFDA contributors. Understanding the spatial structure of RF-induced SOL modifications. *Plasma Physics and Controlled Fusion*, 49(12B):B35, 2007.

[52] E. Faudot, L. Colas, S. Heuraux, and J. P. Gunn. Broadening of rectified potential structures induced by RF currents in a magnetized plasma: Application to ITER scrape-off-layer. *Physics of Plasmas*, 17(4):042503, 2010.

[53] M. Brambilla. Numerical simulation of ion cyclotron waves in tokamak plasmas. *Plasma Physics and Controlled Fusion*, 41(1):1, 1999.

[54] E. F. Jaeger, L. A. Berry, D. B. Batchelor, J. R. Myra, and D. A. D'Ippolito. Full-wave calculation of sheared poloidal flow driven by high harmonic IBW. In *APS Meeting Abstracts*, volume 1, 1999.

[55] V. Lancellotti, D. Milanesio, R. Maggiora, G. Vecchi, and V. Kyrytsya. TOPICA: an accurate and efficient numerical tool for analysis and design of ICRF antennas. *Nuclear Fusion*, 46(7):S476, 2006.

[56] O. Meneghini, S. Shiraiwa, and R. Parker. Full wave simulation of lower hybrid waves in maxwellian plasma based on the finite element method. *Physics of Plasmas*, 16(9):090701, 2009.

[57] S. Shiraiwa, O. Meneghini, R. R. Parker, P. Bonoli, M. L. Garrett, M. C. Kaufman, J. C. Wright, and S. J. Wukitch. Plasma wave simulation based on a versatile finite element method solver. *Physics of Plasmas*, 17(5):056119, 2010.

[58] O. Meneghini and S. Shiraiwa. Full wave simulation of lower hybrid waves in ITER plasmas based on the finite element method. *Plasma and Fusion Research*, 5:S2081–S2081, 2010.

[59] J. W. Hughes, D. A. Mossessian, A. E. Hubbard, E. S. Marmar, D. Johnson, and D. Simon. High-resolution edge thomson scattering measurements on the Alcator C-Mod tokamak. *Review of Scientific Instruments*, 72(1):1107–1110, 2001.

[60] P. U. Lamalle, A. M. Messiaen, P. Dumortier, and F. Louche. Recent developments in ICRF antenna modelling. *Nuclear Fusion*, 46(4):432, 2006.

[61] F. W. Perkins. ICRF heating theory. *Plasma Science, IEEE Transactions on*, 12(2):53 –63, june 1984.

[62] T. Yamamoto, S. Murakami, and A. Fukuyama. Simulation study of ICRF wave propagation and absorption in 3-D magnetic configurations. *Plasma and Fusion Research*, 3:S1075–S1075, 2008.

[63] M.D. Carter, D.A. Rasmussen, P.M. Ryan, G.R. Hanson, D.C. Stallings, D.B. Batchelor, T.S. Bigelow, A.C. England, D.J. Hoffman, M. Murakami, C.Y. Wang, J.B. Wilgen, J.H. Rogers, J.R. Wilson, R. Majeski, and G. Schilling. Three dimensional modelling of ICRF launchers for fusion devices. *Nuclear Fusion*, 36(2):209, 1996.